

1

2

Balloon-borne aerosol-cloud interaction studies (BACIS): New

observational techniques **Field campaigns** to understand and quantify
aerosol effects

on clouds

Ravi Kiran. V¹, Venkat Ratnam. M¹, Masatomo Fujiwara², Herman Russchenberg³, Frank G Wienhold⁴,

Madhavan. B.L¹, Roja Raman. M⁵, Renju Nandan¹, Akhil Raj. S. T¹, Hemanth Kumar. A¹, Ravindra

Babu. S¹

¹National Atmospheric Research Laboratory (NARL), Gadanki, 517 112, India

²Faculty of Environmental Earth Science, Hokkaido University, Sapporo, 060-0810, Japan

³Department of Geoscience and Remote Sensing, Delft University of Technology, Delft, 2628CD, The Netherlands

⁴Institute of Atmospheric and Climate Science (IAC), Universitaetstrasse 16, Zurich, 8092, Switzerland

⁵Department of Physics, Sri Venkateswara University, Tirupati, 517 502, India

14

15

Correspondence to: Ravi Kiran. V (ravikiranv@narl.gov.in)

16

17

18

19

20

21

22

~~23~~
~~24~~
~~25~~
~~26~~
~~27~~
~~28~~
~~29~~

30
31
32

Abstract.

34 ~~Better~~ A better understanding of aerosol-cloud interaction processes is ~~an~~ important ~~aspect~~ to quantify the role of clouds and
aerosols
35 ~~in on~~ the climate system. There have been significant efforts to explain the ways aerosols modulate cloud properties. However,
36 ~~from~~ the observational point of view, it is indeed challenging to observe and/or verify some of these processes because no
37 ~~single~~ instrument or platform is proven sufficient. Discrimination between aerosol and cloud is vital for the quantification of
aerosol-cloud interaction. With this motivation, a ~~unique~~ set of observational field campaigns named
38 ~~Balloon~~ Balloon-borne Aerosol Cloud Interaction Studies (BACIS) is proposed and conducted using balloon~~—~~borne in-situ
39 ~~measurements~~ in addition to the ground-based (Lidars, MST radar, LAWP, MWR, Ceilometer) and space~~—~~borne (CALIPSO)
40 ~~remote sensing instruments from Gadanki (13.45° N, 79.2° E), India.~~ So far, 15 campaigns have been conducted as a part of
BACIS
41 ~~campaigns~~ from 2017 to 2020. This paper presents the concept of the observational approach, lists the major objectives of the
42 ~~campaigns~~, describes the instruments deployed, and discusses results from selected campaigns. ~~Consistency in balloon~~ Balloon-
borne
43 ~~measurements~~ is assessed using the data from simultaneous observations of ground-based, space~~—~~borne remote sensing
44 ~~instruments.~~ A good agreement is found among Aerosol/cloud profiles obtained from the multi-instrumental observations. ~~Balloon~~

are found similar. Apart from this, balloon-borne ~~in-situ~~ profiling ~~is found to~~

~~45—complement the~~provides information ~~provided~~missed by ground-based and/or space-borne measurements. A combination of the Compact

~~46—~~Optical Backscatter Aerosol Detector (COBALD) and Cloud Particle Sensor (CPS) sonde is employed for the first time to

~~47—~~discriminate cloud and aerosol in an in-situ profile. A threshold value of COBALD ~~color~~colour index (CI) for ice clouds is found to

~~48—~~be between 18 and 20 and CI values for coarse mode aerosol ~~particle~~particles range between 11 and 15. Using the data from balloon

~~49—~~measurements, the relationship between cloud and aerosol is quantified for the liquid clouds. A statistically significant slope (aerosol-cloud interaction index) of 0.77 found between aerosol back scatter and cloud particle count reveals the role of aerosol in the cloud activation process. In a nutshell, the results presented here demonstrate the observational approach to quantifying aerosol-cloud interactions.

~~50—(aerosol-cloud interaction index) of 0.77 (0.86) found between aerosol back scatter from 300m (400m) below the cloud base~~

~~51—and cloud particle count within the cloud indicates the role of aerosol in the cloud activation process. In a nutshell, the results~~

~~52—presented here demonstrate the observational approach to quantify aerosol-cloud interactions and paves the way for further~~

~~53—investigations using the approach.~~

56 1 Introduction

~~57—Understanding the fundamental process of aerosol-cloud interactions remains to be a challenging issue in the~~

~~58—scientific community, already for more than three decades (Seinfeld et al., 2016). First ever observational evidence from~~

~~59—analysis of ship tracks using satellite imagery had open up a wide scope for further research in this area (Coakley et al.,~~

~~60—1987; Radke et al., 1989). Since then, efforts are underway using different observational and modeling techniques and lead~~

~~61—to a significant development in the process based understanding, quantification and modeling (Abbott and Cronin, 2021; Fan~~

62 et al., 2018; Haywood and Boucher, 2000; Koren et al., 2010; Lohmann, 2006; Lohmann and Feichter, 2004; Rosenfeld et
63 al., 2008, 2014b). Despite of all these efforts, radiative forcing estimates due to aerosol cloud interactions still show large
64 uncertainties (IPCC, 2013). Apart from this, climate model simulations have uncertainties due to the fact that
65 parameterization schemes are inefficient in representing the ways aerosols interact with clouds (Fan et al., 2016; Rosenfeld
66 et al., 2014b; Seinfeld et al., 2016). At process level, various hypothesis have been proposed subsequent to the first indirect
67 effect which was proposed almost four decades ago (Twomey, 1977). All these effects are found to act specific to cloud
68 based on background meteorological, dynamical conditions. For example, the invigoration effect is proposed for convective
68 clouds (Rosenfeld et al., 2014a) under the influence of updrafts. First indirect effect (Twomey effect) and second indirect
69 effect (Albrecht effect) for liquid clouds have been shown to be influenced by mixing (Costantino and Bréon, 2010),
69 turbulence and entrainment (Jose et al., 2020; Schmidt et al., 2015; Small et al., 2009). Although the first indirect effect is
70 reasonably well understood, observational limitation poses serious challenges in understanding and/or evaluating other
71 hypotheses.

71 Among the various observational techniques that are currently available (ground based, space borne remote sensing
72 and aircraft or unmanned ariel vehicle; UAV), none of the single observational technique has been proven self sufficient in
73 aerosol cloud interaction studies. For example, ground based (and/or space borne) lidars suffer serious attenuation and even
73 losses of observations due to the presence of optically thick cloud layers in the atmosphere. Thus, they may not be able to
74 represent the complete vertical structure of cloud and aerosols. Note that information on aerosol/cloud profile is essential for
74 the estimation of their climate effects. Similarly, satellite data analysed with different analytical methods such as by
74 changing grid resolutions have shown different results and conclusions (Grosvenor et al., 2018; Koren et al., 2010;
75 McComiskey and Feingold, 2012). Besides this, in situ measurements using aircraft and UAV have been remarkable in
75 obtaining detailed information on the microphysics of cloud and aerosol (Corrigan et al., 2008; Kulkarni et al., 2012;
76 Redemann et al., 2020; Weinzierl et al., 2017). However, there are serious limitations with respect to altitude coverage,
77 feasibility of conducting aircraft or UAV campaigns and overall cost involved. Also, there is a chance that the aircraft
77 perturb the atmosphere before it actually makes the measurement of cloud/aerosol.

78 Therefore, it is essential to examine the combined information obtained simultaneously using multi instrumental
— techniques so as to obtain a comprehensive picture. A classic paper by Feingold et al. (2003) first time quantified the
79 ‘Twomey effect’ using ground based remote sensing instruments such as a micro wave radiometer (MWR), cloud radar and
80 a Raman Lidar. In an intensive operations program, Feingold et al. (2006) conducted airborne in situ measurements for
80 obtaining the cloud effective radius using an aircraft in addition to the ground based and space borne remote sensing
80 instruments. Pandithurai et al. (2009) also quantified the ‘Twomey effect’ using a suite of ground based remote sensing
80 instruments (cloud radar, MWR, polarization Lidar) along with the surface aerosol measurements (aerosol size distribution,
80 scattering coefficient and cloud condensation nuclei concentration). Similarly, Sena et al. (2016) utilized 14 years of
81 coincident observations from cloud radar and a laser Ceilometer along with surface reaching shortwave radiation
82 measurements from the Atmospheric Radiation Measurement (ARM) program over the Southern Great Plains, USA to
82 investigate aerosol modifications on cloud macroscopic parameters and radiative properties rather than cloud microphysical
83 parameters. In addition to simultaneous measurements of cloud/aerosol, concurrent measurements of thermodynamic and
83 dynamic parameters of the atmosphere are also needed to thoroughly understand the process of aerosol cloud interactions. A
83 step forward in this direction, McComiskey et al. (2009) used long term, statistically robust ground based remote sensing
83 data from Pt. Reyes, California, USA to not only quantify the ‘Twomey effect’ but also examine the factors influencing the
84 variability in aerosol indirect effects such as updraft velocity, liquid water path, scale and resolution of observations. Using a
84 novel dual field of view Raman Lidar and a Doppler Lidar technique, Schmidt et al. (2014) analysed the data from Leipzig,
85 Germany to explore linkages between aerosol and cloud properties, the influence of updrafts. Sarna and Russchenberg,
85 (2016) used synergy of measurements from a Lidar (Ceilometer), Radar (cloud radar) and a Radiometer (MWR) collected at
86 ARM Mobile facility at Graciosa Island, the Azores, Portugal and at the Cabaw Experimental Site for Atmospheric Research
86 (CESAR) observatory, The Netherlands, to not only quantify the aerosol indirect effect but also attempted to disentangle the
86 effect of vertical wind (Sarna and Russchenberg, 2017). All these studies contributed significantly to the knowledge on
86 aerosol cloud interactions but are based on remote sensing techniques, limited to the low level, warm and non precipitating
86 clouds only.

~~In view of~~Understanding the fundamental process of aerosol-cloud interactions remains to be a challenging issue in the scientific community, already for more than three decades (Seinfeld et al., 2016). First-ever observational evidence from analysis of ship tracks using satellite imagery had opened up a wide scope for further research in this area (Coakley et al., 1987; Radke et al., 1989). Since then, efforts are underway using different observational and modelling techniques and lead to a significant development in the process-based understanding, quantification, and modelling (Abbott and Cronin, 2021; Fan et al., 2018; Haywood and Boucher, 2000; Koren et al., 2010; Lohmann, 2006; Lohmann and Feichter, 2004; Rosenfeld et al., 2008, 2014b). Despite all these efforts, radiative forcing estimates due to aerosol-cloud interactions still show large uncertainties (IPCC, 2021). Apart from this, climate model simulations have uncertainties because parameterization schemes are inefficient in representing the ways aerosols interact with clouds (Fan et al., 2016; Rosenfeld et al., 2014b; Seinfeld et al., 2016). At the process level, various hypotheses have been proposed after the first indirect effect which was proposed almost four decades ago (Twomey, 1977). All aerosol-cloud effects are found to act specifically to cloud type, background meteorological, and dynamical conditions. For example, the invigoration effect is proposed for convective clouds (Rosenfeld et al., 2014a) under the influence of updrafts. The first indirect effect (Twomey effect) and the second indirect effect (Albrecht effect) for liquid clouds be influenced by mixing (Costantino and Bréon, 2010), turbulence, and entrainment (Jose et al., 2020; Schmidt et al., 2015; Small et al., 2009). Although the first indirect effect is reasonably well understood, observational limitation poses serious challenges in understanding and/or evaluating other hypotheses.

Among the various observational techniques that are currently available (ground-based, space-borne remote sensing, and aircraft or unmanned aerial vehicle; UAV), none of the techniques alone has been proven self-sufficient in aerosol-cloud interaction studies. For example, ground-based (and/or space-borne) lidars suffer serious attenuation and even losses of observations due to the presence of optically thick cloud layers in the atmosphere. Thus, they may not be able to represent the complete vertical structure of clouds and aerosols. Note that information on aerosol/cloud profiles is essential for the estimation of their climate effects. Similarly, satellite data sets have shown distinct results and conclusions (Grosvenor et al., 2018; Koren et al., 2010; McComiskey and Feingold, 2012) using different analytical methods for example changing grid resolutions, etc. Besides this, in-situ measurements using aircraft and UAVs have been remarkable in obtaining detailed information on the microphysics of cloud and aerosol (Corrigan et al., 2008; Girdwood et al., 2020, 2021; Kulkarni et al., 2012; Mamali et al., 2018; Redemann et al., 2020; Weinzierl et al., 2017). However, there are serious limitations concerning altitude coverage, the feasibility of conducting aircraft or UAV campaigns, and the overall cost involved. Also, there is a chance that the aircraft perturb the atmosphere before it measures cloud/aerosol.

Therefore, it is essential to examine the combined information obtained simultaneously using multi-instrumental techniques to obtain aerosol, cloud and associated environmental parameters to understand aerosol-cloud interaction. A classic paper by Feingold et al. (2003) first time quantified the ‘Twomey effect’ using ground-based remote sensing instruments such as a microwave radiometer (MWR), cloud radar, and a Raman Lidar. In an intensive operations program, Feingold et al. (2006) conducted airborne in-situ measurements for obtaining the cloud effective radius using an aircraft in addition to the ground-based and space-borne remote sensing instruments. Pandithurai et al. (2009) also quantified the ‘Twomey effect’ using a suite of ground-based remote sensing instruments (cloud radar, MWR, polarization Lidar) along with the surface aerosol measurements (aerosol size distribution, scattering coefficient, and cloud condensation nuclei concentration). Similarly, Sena et al. (2016) utilized 14 years of coincident observations from cloud radar and a laser Ceilometer along with surface-reaching shortwave radiation measurements from the Atmospheric Radiation Measurement (ARM) program over the Southern Great Plains, USA to investigate aerosol modifications on cloud macroscopic parameters and radiative properties rather than cloud microphysical parameters. In addition to simultaneous measurements of cloud/aerosol, concurrent measurements of thermodynamic and dynamic parameters of the atmosphere are also needed to thoroughly understand the process of aerosol-cloud interactions. A step forward in this direction, McComiskey et al. (2009) used long-term, statistically robust ground-based remote sensing data from Pt. Reyes, California, the USA to not only quantify the ‘Twomey effect’ but also examine the factors influencing the variability in aerosol indirect effects such as updraft velocity, liquid water path, scale, and resolution of observations. Using a novel dual field of view Raman Lidar and a Doppler Lidar technique, Schmidt et al. (2014) analyzed the data from Leipzig, Germany to explore linkages between aerosol, cloud properties, and the influence of updrafts. Sarna and Russchenberg, (2016) used synergy of measurements from a Lidar (Ceilometer), Radar (cloud radar) and a Radiometer (MWR) collected at ARM Mobile facility at Graciosa Island, the Azores, Portugal, and the Cabaw Experimental Site for Atmospheric Research (CESAR) observatory, The Netherlands, to not only quantify the aerosol indirect effect but also attempted to disentangle the effect of vertical wind (Sarna and Russchenberg, 2017). All these studies contributed significantly to the knowledge on aerosol-cloud interactions but are based on remote sensing techniques, limited to the low-level, warm, and non-precipitating clouds only.

87———Given the measurement limitations discussed above, a balloon-borne in-situ measurement is suggested to be the
89——best complementary complementary technique as balloons can pass through the cloud (during their ascent/descent) representing the
vertical
91——structure of the cloud as well as aerosol below and above the cloud near simultaneously (see Sect. 2 for details) without
93——perturbing the atmosphere. InformationAlthough there is less information and data on balloon-based aerosol sampling artefacts
than on conventional aircraft, information from balloon-borne in-situ measurements in combination with the ground-based

95 and/or space-borne platforms will be of great help in constructing the complete vertical profiles of aerosol, cloud ~~and~~

further, and further understanding the process of aerosol-cloud interactions. With this in mind, a balloon-borne field campaign named BACIS (Balloon-borne Aerosol Cloud Interaction Studies) was initiated in the year 2017 at National Atmospheric Research Laboratory (NARL), Gadanki (13.45° N, 79.2° E), India, with the multi-instrumental approach.

understanding the process of aerosol-cloud interactions. With this in mind, a balloon-borne field campaign named BACIS (Balloon-borne Aerosol Cloud Interaction Studies) was initiated in the year 2017 from National Atmospheric Research Laboratory (NARL), Gadanki (13.45° N, 79.2° E), India, with multi-instrumental approach. Gadanki located in Southern Peninsular India is influenced by both the South West and North East Monsoon. Most importantly the location hosts a suit of unique ground-based instruments that cover optical, radio and in-situ techniques. A combination of specialized sondes like the Compact Optical Backscatter Aerosol Detector (COBALD; see <https://iac.ethz.ch/group/atmospheric-chemistry/research/ballon-soundings.html>, last access: 19 June 2021) and the Cloud Particle Sensor (CPS; Fujiwara et al., 2016) are used together for the first time in the present study.

The concept of observational strategy, objectives of the campaign and details about the balloon sensors, ground/space-based instruments, data processing, interpretation of data are provided in the second section. The third section discusses the results on consistency in multi-instrumental observations, interpretation of aerosol and cloud features in a profile, multiple soundings to estimates statistics on threshold values of aerosol/cloud and finally illustrates the relationship between aerosol-cloud relationships. The fourth section summarizes the results.

Balloon-borne measurement of aerosol/cloud was first reported in Rosen and Kjöme, 1991 using a backscatter sonde developed by them. COBALD is similar to this but lightweight sonde (Brabec et al., 2012). Measurements of aerosol size distribution in the stratosphere were carried out using an optical particle counter developed at Wyoming university (Deshler et al., 2003). But Smith et al., 2019 developed a novel, low-cost, and lightweight open path configuration optical particle counter, UCASS (Universal Cloud Aerosol Sampling System) for a wide range of particle size measurements covering both aerosol and cloud. Kezoudi et al., 2021 and Mamali et al., 2018 used UCASS and reported balloon-borne in-situ measurement of dust aerosol and compared UCASS with ground-based, airborne instruments. However, BACIS campaigns are designed to understand and quantify aerosol-cloud interactions. For this, a combination of balloon-borne sondes, COBALD and CPS is used for the first time to separate/discriminate aerosol and cloud in a profile. Note that individually COBALD and CPS have been used in other studies (Brunamonti et al., 2018, 2020; Fujiwara et al., 2016a; Hanumanthu et al., 2020; Inoue et al., 2021; Vernier et al., 2015, 2018).

The purpose of this manuscript is to introduce the motivation and objectives of the BACIS Campaigns for quantifying aerosol-cloud interactions. In order to do this, we have discussed most related topics, such as the campaign approach, sensors/instruments employed, analytical methods and comparison of balloon features. Results from selected campaigns focus on discrimination of aerosol/cloud in a profile. Overall, the methods presented in this paper for the data analysis/processing are novel. Using these methods aerosol-cloud interaction is estimated in liquid clouds.

99 **2. Instruments and ~~methodology~~ methods**

101 **2.1. Balloon-~~b~~orne sensors**

103 **2.1.1. COBALD**

105 The Compact Optical Backscatter Aerosol Detector (COBALD) deployed in BACIS campaigns is a lightweight
107 (540 g) balloon-~~b~~orne sonde developed in the group of Professor Thomas Peter at ETH Zurich, Switzerland. It is essentially a
109 miniaturized version of the backscatter sonde developed by Rosen and Kjome (1991). A backscatter sonde is a balloon-borne sensor which measures the backscattered light from molecules, aerosol and clouds at multiple wavelengths in the vicinity of the sonde as it passes through the atmospheric column. The COBALD consists of two LED light
111 sources of approximately 500 mW power emitting 455 nm (blue) and 940 nm (termed ‘infrared’) wavelengths, respectively

~~112 (Brabec et al., 2012). (Brabec et al., 2012).~~ The light emitted by the sonde illuminates the air in the vicinity, and backscattered light ~~from an ensemble of particles~~ is detected
~~114 using a silicon photo-detector-photodetector.~~ The emitted ~~beams~~beam's divergence (with a full-width half-maximum of 4 degrees ~~FWHM~~), detector field of view (of 6 degrees~~→~~), and
~~116 geometrical alignment of optics yields~~ the reception of backscatter light from a distance of 0.5 m (overlapping distance) from the
~~118 sonde.~~ The region of up to 10 m from the instrument contributes to 90 % of the measured backscattering signal. The real-
~~120 time backscatter data, in units of counts per secondssecond~~ (cps, originating from the internal data treatment) is included in the
~~122 radiosonde telemetry at a frequency of 1 Hz and sent to the ground station along with the pressure and temperature~~
~~124 measurements.~~ In the present case, we have used an iMet radiosonde (InterMet, USA). The sondes were usually operated for
~~126 about 15 minutes at the surface (before launch) for thermal stabilization, verified by cross-checking the LED brightness~~
~~128 monitor signals, and also delivered in epscounts per second,~~ with sonde specific reference values provided by the ~~manufacture~~manufacturer. The sonde is ~~passed~~
~~130 launched~~ when the return signal data at the surface is within $\pm 15\%$ of the reference value.

~~143~~ **2.1.2. CPS**

~~145 Cloud Particle Sensor (CPS) sonde is a light-weightlightweight~~ balloon~~-~~borne sensor (~200 g) developed for the detection of
~~147 cloud particle number and phase (Fujiwara et al., 2016).~~ cloud particle number and phase (Fujiwara et al., 2016b). The latest version of the sonde (launched in the campaigns) is
~~149 supplied by Meisei Electric Corporation, Japan, along with a Meisei RS-11G radiosonde (Kobayashi et al., 2019; RS-~~
~~151 (Kobayashi et al., 2019; RS-11G(R3) is the model with an interface for CPS).~~ CPS primarily consists of a column (~1 cm x 1 cm in cross-section and
~~153 ~12 cm in vertical length) for air passage, a diode laser (~790 nm, polarized→), and two silicon photo-detectors-photodetectors.~~ Cloud particles
~~155 entering the column due to the balloon ascent are illuminated by the laser. The scattered light from cloud particles is detected~~
~~157 by the photo-detectorsphotodetectors~~ placed at an angle of 55° and 125° to the incident laser light. The detector at 125° comes with an
~~159 additional polarization plate positioned in front of it for the detection of cross-polarization whereas the detector at 55°~~
~~161 measures the intensity of plane-polarized scattered light. The intensities I55 and I125, for the detectors located at 55° and~~
~~163 125°, respectively, are provided in voltage, and I55 is related to particle size. The minimum size of a water droplet that can~~

~~165~~ _be detected by CPS is found to be 2 μm (1 μm particles are undetected in laboratory experiments using various standard
~~167~~ _spherical particles) and I55 was found to sometimes saturate ($\sim 7.5\text{V}$) for particles $\sim 80\text{-}140\text{ }\mu\text{m}$ (Appendix A of Fujiwara et
~~169~~ _al., 2016). Real-time data from CPS ~~is~~has been transferred to the ground station through RS-11G_(R3) radiosonde at a frequency
of
~~171~~ _1Hz. CPS data include the number of particles counted in a sec, scatted light intensity (in Voltage) for the two detectors (I55 and

172—I125), as well as particle signal width for the first six particles for each second, and DC output voltage. The particle
174—information is transmitted to the ground station only for the first six particles for each second due to the limited downlink
176—rate of RS-11G which is 25 byte s⁻¹. Before launch, the sonde is tested by spraying water near to air passage column for
particle detection.

178—particle detection.

180 2.2. Remote sensing instruments

163 2.2.1. MPL/Ceilometer

165—A Micro Pulse Lidar (MPL) was operated on 07-08 July 2017 during the first two campaigns. However, a laser
167—Ceilometer (make of Vaisala, Finland) was made available for the rest of the campaigns due to non availability of MPL.
169—Complete technical details of MPL used in the campaign can be found in Cherian et al. (2014). Cherian et al. (2014). A low energy
($< 10 \mu\text{j}$) green
171—(532 nm) pulsed laser of pulse width less than 10 ns ~~were~~was shot from MPL at a pulse repetition frequency of 2500 s⁻¹. A
173—Cassegrain type telescope of 150 mm diameter and a PMT have been deployed to collect the backscattered photons (co-
175—polarized) from particles and clouds in the atmosphere. The entire system is operated at a dwell time of 200 ns which would
177—correspond to a range resolution of 30 m. The return signals were collected for 1500 bins which correspond to the total range
179—of 45 km. A profile of backscattered photons was obtained for every 300 μs and all profiles collected were averaged for
181—every one minute. The telescope field of view and laser beam divergence ~~coincide~~coincide or overlap at above ~150 m. Using the
183—data from MPL (from Gadanki and the nearby location at Sri Venkateswara University, Tirupati, India (13.62°N, 79.41°E;
185—~~35 km from Gadanki~~), ~~Ratnam et al. (2018)~~ ~35 km from Gadanki), ~~Ratnam et al. (2018)~~ reported the presence of an elevated
aerosol layer in the lower troposphere (~3
187—km) during South-West Monsoon Season and discussed the possible causes for the formation and maintenance of this
189—elevated layer. The low-level jet (LLJ) between 2 and 3 km in the lower troposphere present during ~~South West~~the southwest
Monsoon
191—causes the formation of an elevated layer. In addition, the presence of shear between LLJ and tropical easterly jet (TEJ) maintains
193—the elevated layer restricting the upliftment of aerosol. ~~Prasad et al. (2019)~~Prasad et al. (2019) also used the same dataset
to discuss nocturnal, seasonal, and intra-annual variations in the tropospheric aerosol.

194 seasonal and intra-annual variation in the tropospheric aerosol. A laser Ceilometer (operated in rest of the campaigns) is
195 similar to a MPL but operates at 910 nm wavelength and provides round-the-clock measurements of cloud base heights,
196 boundary layer height apart from aerosol extinction under all weather conditions (Wiegner et al., 2014).

A Ceilometer (make from Vaisala, Finland) was used in the rest of the campaigns during non-available dates of MPL. It is similar to
an MPL but operates at a 910 nm wavelength and provides round-the-clock measurements of cloud base heights, and boundary layer height
apart from aerosol extinction under all weather conditions (Wiegner et al., 2014).

197 2.2.2. Mie Lidar

198 Mie lidar at Gadanki is a unique lidar system with capabilities to probe the atmosphere to higher altitudes (~30 km).
199 This lidar was operated in almost all the campaigns. A very high energy (600 mJ) pulsed laser of pulse width of less than 7
ns and a pulse repetition frequency of 50 s^{-1} is operated at a wavelength of 532 nm. A 320 mm diameter Cassegrain type
200 telescope along with a couple of PMT has been used as a detection assembly to collect the co and cross polarized return
200 signal. However, the co-polarization channel (only) is analysed in the present study. The data is stored at a dwell time of 2 μs
200 which corresponds to the range resolution of 300 m and the profiles collected were averaged for every 250 sec (~4 min).
200 The data is considered to be reliable from an altitude of 3-4 km as the field of view of Mie telescope and laser beam
200 divergence overlap at this height (Pandit et al., 2014). For the first time, sixteen years of Mie lidar data has been analysed to
200 determine the long-term climatology of tropical cirrus clouds (Pandit et al., 2015). Gupta et al. (2021) reported the long-term
200 observations of aerosol extinction profiles using combination of MPL, Mie lidar and space borne CALIPSO lidar.

Mie lidar at Gadanki is a unique lidar system with capabilities to probe the atmosphere to higher altitudes (~30 km). This lidar was
operated in almost all the campaigns. A very high energy (600 mJ) pulsed laser with a pulse width of a few 7 ns and a pulse repetition frequency
of 50 s^{-1} is operated at a wavelength of 532 nm. A 320 mm diameter Cassegrain type telescope along with a couple of PMT has been used as
a detection assembly to collect the co and cross-polarized return signal. However, the co-polarization channel (only) is analysed in the present
study. The data is stored at a dwell time of 2 μs which corresponds to the range resolution of 300 m and the profiles collected were averaged
every 250 sec (~4 min). The data is considered to be reliable from an altitude of 3-4 km as the field of view of the Mie telescope and laser
beam divergence overlap at this height (Pandit et al., 2014). For the first time, sixteen years of Mie lidar data have been analysed to determine
the long-term climatology of tropical cirrus clouds (Pandit et al., 2015). Gupta et al. (2021) reported the long-term observations of aerosol
extinction profiles using a combination of MPL, Mie lidar, and a space-borne CALIPSO lidar.

2.2.3. CALIPSO

203 Cloud-Aerosol Lidar with Orthogonal Polarization (CALIOP) is the space-born lidar ~~on-board~~onboard the CALIPSO
satellite

205 (L'Ecuyer, 2011). (L'Ecuyer, 2011). CALIOP consists of two pulsed diode lasers operating at 532 and 1064 nm wavelengths with
pulse energy

207 of 110 mJ and a repetition rate of ~20 Hz. A Backscattered signal is collected by an avalanche ~~photo-diode~~photodiode (APD) at
1064 nm

209 and ~~photo-multiplier~~photomultiplier tubes (PMT) at 532 nm. The signals at 532 nm are collected at both parallel and perpendicular
to the

plane of polarization of the outgoing beam, while for 1064 nm channel polarization is parallel only. The range resolution of the backscattered profile at 532 nm is 30 m for the altitude range from -0.5 to 8.2 km, 60 m for 8.2 to 20.2 km and 180 m for >20-30 km. Horizontal resolution is 0.33 km for -0.5 to 8.2 km and 1 km for 8.5-20.2 km. More details about CALIOP can be found in Winker et al. (2007).

~~be found in Winker et al. (2007).~~

2.2.4. MST Radar

~~The Indian MST radar located at Gadanki is high power coherent backscatter VHF (Very High Frequency) radar operating at 53MHz. The detailed description of MST radar can be found in Rao et al. (1995). Before the BACIS campaign, it has been upgraded to a fully active phased array with dedicated 1 kW solid state transmitter receiver units (total power of~~

The Indian MST radar located at Gadanki is a high-power coherent backscatter VHF (Very High Frequency) radar operating at 53MHz. A detailed description of MST radar can be found in Rao et al. (1995). Before the BACIS campaign, it has been upgraded to a fully active phased array with dedicated 1 kW solid-state transmitter-receiver units (total power of 1024 kW). This radar operates in Doppler Beam Swinging (DBS) mode to provide wind information covering the

troposphere, lower stratosphere and mesosphere. Atmospheric scatterers are advected with the background air motions and

the three-dimensional wind velocity vectors (zonal, meridional and vertical) can be directly deduced from the Doppler shifts of the radar echoes received in three independent beam directions. Note that these radars are the only means of getting direct vertical velocities presently and ~~playsplay~~ a crucial role in the understanding of aerosol-cloud interaction processes. For the present study, data is obtained from five beam directions with 256 FFT (Fast Fourier Transform) points and coherent integrations, 4 incoherent integrations, Inter Pulse Period (IPP) of 160 ms, the pulse width of 8 μ s coded covering the altitude region of 3 to 21 km with 150 m vertical resolution.

~~integrations, 4 incoherent integrations, Inter Pulse Period (IPP) of 160 ms, pulse width of 8 μ s coded covering the altitude region of 3 to 21 km with 150 m vertical resolution.~~

2.3. The observational concept of the BACIS Campaign

~~A unique observational approach is proposed here wherein a balloon borne in situ measurement is made simultaneously while the multiple remote sensing instruments are operational from the ground and space borne platforms. The schematic diagram shown in Figure 1 illustrates the entire concept. A meteorological balloon with specialized sondes such as COBALD (Brabee et al., 2012) and CPS (Fujiwara et al., 2016) along with a radiosonde is launched 10-30 minutes prior to CALIOP on board Cloud Aerosol Lidar and Infrared Pathfinder Satellite Observation (CALIPSO; Winker et al., 2007) (night time) overpass close by Gadanki. Ground based remote sensing instruments at NARL, Gadanki such as a Micro Pulse Lidar (MPL; Cherian et al., 2014) and/or a laser Ceilometer (Wiegner et al., 2014), a Mie Lidar (subsequently referenced to as ‘Mie’; Pandit et al., 2014), an Indian MST Radar (Rao et al., 1995) and/or a Lower Atmospheric Wind Profiler (LAWP; Srinivasulu et al., 2012) are also operated before, during and after the launch. Other observational facilities such as ambient aerosol instruments at the Indian Climate Observatory Network (ICON), NARL, Gadanki and a MWR are operated during the launch period. Table 1 lists the ensemble of instruments used in the campaign, their purpose and the physical quantity that can be obtained from each instrument. Temporal variation of remote sensing data on cloud and aerosol profiles is obtained from ground based (MPL/Mie) lidars. Space borne lidar (CALIPSO) also provides the same but for an along track (roughly meridional) distribution near the time of overpass over Gadanki. On the other hand, in situ measurements of aerosol and cloud profiles along with background meteorological parameters (temperature, relative humidity, wind speed and direction) are collected using the specialized balloon sounding (COBALD and CPS). Combined~~

data from balloon, ground/space borne lidars are the basis for the identification of aerosol and cloud particles. Apart from
247 this, temporal variation in wind components obtained from the ground based radars (MST Radar and/or LAWP) aids in

—entangling the effect of vertical winds and turbulence on aerosol-cloud interactions. A MWR provides the cloud liquid water
248—and relative humidity profiles, etc., useful to constrain the cloud water content in a cloud layer to understand the aerosol
248—influence on cloud properties. In addition to these measurements, surface aerosol information obtained by the
249—instrumentation available at the ICON observatory, NARL helps in understanding the role of sources of aerosol from the
249—surface. Altogether, near simultaneous information on the aerosol, cloud and background meteorological conditions obtained
249—from the multi-instruments is aimed to understand the aerosol-cloud interactions.

An observational approach is conceptualized here wherein a balloon-borne in-situ measurement is made simultaneously while the
multiple remote sensing instruments are operated from the ground and spaceborne platforms. The schematic diagram shown in Figure 1
illustrates the observational approach. A meteorological balloon with specialized sondes such as COBALD (Brabec et al., 2012) and CPS
(Fujiwara et al., 2016b) along with a radiosonde is launched ~10-30 minutes before CALIOP onboard Cloud-Aerosol Lidar and Infrared
Pathfinder Satellite Observation (CALIPSO; Winker et al., 2007) (night time) overpass close by Gadanki. Ground-based remote sensing
instruments at NARL, Gadanki such as a Micro Pulse Lidar (MPL; Cherian et al., 2014) and/or a laser Ceilometer (Wiegner et al., 2014), a
Mie Lidar (subsequently referenced to as ‘Mie’; Pandit et al., 2014), an Indian MST Radar (Rao et al., 1995) and/or a Lower Atmospheric
Wind Profiler (LAWP; Srinivasulu et al., 2012) are also operated before, during and after the launch. Other observational facilities such as
ambient aerosol instruments at the Indian Climate Observatory Network (ICON), NARL, Gadanki and an MWR are operated during the launch
period. Table 1 lists the ensemble of instruments used in the campaign, their purpose and the physical quantity that can be obtained from each
instrument. Temporal variation of remote sensing data on the cloud and aerosol profiles is obtained from ground-based (MPL/Mie) lidars.
Spaceborne lidar (CALIPSO) also provides the same but for an along-track (roughly meridional) distribution near the time of overpass over
Gadanki. On the other hand, in-situ measurements of aerosol and cloud profiles along with background meteorological parameters
(temperature, relative humidity, wind speed and direction) are collected using the specialized balloon sounding (COBALD and CPS).
Combined data from balloon and ground/spaceborne lidar is the basis for the identification of aerosol and cloud particles. Apart from this,
temporal variation in wind components obtained from the ground-based radars (MST Radar and/or LAWP) aids in entangling the effect of
vertical winds and turbulence on aerosol-cloud interactions. An MWR provides the cloud liquid water and relative humidity profiles, etc.,
useful to constrain the cloud water content in a cloud layer to understand the aerosol influence on cloud properties. In addition to these
measurements, surface aerosol information obtained by the instrumentation available at the ICON observatory, NARL helps in understanding

the role of sources of aerosol from the surface. Altogether, near-simultaneous information on the aerosol, cloud and background meteorological conditions obtained from the multi-instruments is aimed to understand the aerosol-cloud interactions.

250—Initially, when the experiment was being conceptualized, it was thought to conduct a launch once in one or two
252—_months. However, due to the limited number ~~of~~ stock of specialized sondes (available with us), it was decided to conduct
254—_instead two pilot campaigns to demonstrate the concept proposed. Apart from this, it was also required to have
256—_balloon/payload tracking equipment to ensure the safe recovery of the payloads. A low-cost GPS/GSM—_based tracker ~~was~~
258—~~made available~~is used for this purpose. Subsequently, two pilot campaigns were conducted in the early hours of 6 June and 8 July
260—_2017. Table 2 lists the date and time of all balloon campaigns that have been conducted from Gadanki as a part of BACIS
262—_campaigns and the instruments operated during the corresponding campaign. As shown in Table 2, so far 15 launches have
been conducted from the year 2017 to 2020.

264—~~been conducted from the year 2017 to 2020.~~

266—Figure 2 shows the photographs taken at the balloon facility, NARL just before the launch during one of the
268—_campaigns. The balloon payload with specialized sondes (COBALD, CPS) and radiosonde (iMet and RS-11G) is shown in
270—_Fig. 2(a) and the prelaunch activities at the field are shown in Fig. 2(b). Skilled personnel were deployed for the launch and
272—_recovery of the payload. As of now, we have recovered all the launch payloads successfully (~~expect~~except one) with the help of
274—_GPS/GSM tracker assembly. Except for the two pilot campaigns, the rest of them were conducted during the ~~nights~~night
irrespective
276—_of the CALIPSO satellite overpass as there was a maneuverer in CALIPSO orbit during September 2018 (CALIPSO track
278—_got departed from A-Train to join C-Train. More details can be found at link <https://atrain.nasa.gov/>), followed by which we
280—_could not find CALIPSO nighttime passage close by Gadanki. Apart from this, MPL measurements were not available after
282—_a few initial campaigns due to ~~the~~ technical issues. However, a laser Ceilometer was operated in place of MPL. The other
284—_major issue for conducting a campaign was the limited availability of specialized sondes and compatible radiosondes, and
GPS/GSM
286—_tracker assembly, among others. Because of these reasons, campaigns were conducted on random dates. However, as ~~it can~~

287 ~~be seen from the~~ Table 2, we have managed to operate all the essential instruments proposed in the observational approach
during other campaigns. In particular, the campaigns in the year 2019 were conducted once a month (March to June 2019) or for two months
(July to December 2019).

289 ~~during other campaigns. In particular, the campaigns in the year 2019 were conducted once in a month (March to June,~~
291 ~~2019) or two months (July to December, 2019).~~

293 With the observational approach described above, the following scientific issues/objectives are being pursued/realized:

295 ~~i. Demonstration of the potential of the multi-instrumental observational approach in obtaining the information on the aerosol~~
~~and~~
297 ~~i. _____, cloud, and associated environmental parameters, such as 3D-winds, relative humidity, and temperature ~~near~~ simultaneously.~~

299 ~~ii. Show consistency Comparison of balloon-borne in-situ measurements among the combination of ~~space-borne~~ spaceborne~~
~~and/or ground-based~~
301 ~~ii. _____ instruments.~~

303 ~~iii. Discrimination of aerosol and cloud in a balloon sounding using the combined observations of COBALD and CPS~~
05 ~~iii. _____ sondes. This is a prerequisite to use balloon information for aerosol cloud studies.~~

307 ~~iv. Testing Verifying and quantification of aerosol-cloud interactions and understanding the influence of meteorological and~~
09 ~~iv. _____ dynamical parameters.~~

311 ~~v. Find out the differences, if any, in the estimates of the magnitude of aerosol-cloud interaction using multi-instruments~~
313 ~~v. _____ and discuss the possible reasons for the observed discrepancies.~~

315 ~~vi. _____ vi. Understanding of how ~~do these~~ the indirect effects of aerosols change radiative transfer through the atmosphere.~~

317 ~~vii. _____ vii. Assessment of Weather and Climate model simulations using the multi-sensor data.~~

318 **2.4. Methods of data processing and interpretation**

319 **2.4.1. COBALD data processing**

320 ~~Backscattered light received -by COBALD is contributed fromby molecules, aerosols and cloud -particles in the~~

~~321~~ atmosphere. The molecular Rayleigh contribution to the raw signal (cps) is established during the post-processing of the data

~~322~~ using the simultaneous temperature and pressure recordings of the radiosonde. It serves to normalize the total signal in terms

of backscattering ratio (BSR) according to

~~323~~ of backscattering ratio (BSR) according to

~~324~~
$$BSR = \frac{\beta_{total}}{\beta_{molecular}} \quad (1)$$

~~325~~ where β_{total} and $\beta_{molecular}$ are the backscatter coefficient corresponds to the contribution from particles plus molecules and

326 molecules, respectively. The sole particle contribution is obtained by BSR-1, which expresses the ratio of particle
 327 backscatter coefficient to the molecular one. The uncertainty in the COBALD BSR is estimated to be 1% and 5% at surface
 328 level and 10 km, respectively (Brabec et al., 2012; Vernier et al., 2015). The Color Index (CI), referring to the particle
 329 backscatter only, is calculated from Equation 2.

$$330 \quad CI = \frac{BSR_{940}-1}{BSR_{455}-1} \quad (2)$$

$$BSR = \frac{\beta_{total}}{\beta_{molecular}} \quad (1)$$

Where β_{total} and $\beta_{molecular}$ are the backscatter coefficients corresponding to the contribution from particles plus molecules and Molecules,
 respectively. The sole particle contribution is obtained by BSR-1, which expresses the ratio of particle backscatter coefficient to the molecular
 one. The uncertainty in the COBALD BSR is estimated to be 1% and 5% at the surface level and 10 km, respectively (Brabec et al., 2012;
 Vernier et al., 2015). The Color Index (CI), referring to the particle backscatter only, is calculated from Equation 2.

$$CI = \frac{BSR_{940}-1}{BSR_{455}-1} \quad (2)$$

331 By definition, CI is an independent quantity of particle number concentration and is hence useful in interpreting the size of a
 332 particle. For analysis, COBALD raw data is binned ~~in to~~into 1 hPa pressure levels. This could minimize noise, and unwanted data
 333 ~~and smoothenings~~smoothen the profile. Figure 3 shows a typical example of COBALD data collected during the second campaign
 (8 July
 334 2017). BSR at 455 nm and 940 nm wavelength channels are represented by blue and red ~~colored~~coloured lines, respectively,
 while CI
 335 (derived using Equation 2) is shown in the green ~~colored~~coloured line. From Fig. 3, a sharp increase in all parameters (BSR at
 two
 336 channels, CI) found around 5 km associated with a thermal inversion (see temperature profile in Fig.3 in black ~~color~~colour) may
 be
 337 attributed to the presence of a low-level cloud or elevated aerosol layer. Below ~5 km, the BSR profile indicates tropospheric
 338 aerosol distribution. Within this altitude, BSR values around 2 km indicate boundary layer confinement. Note no significant
 339 changes in CI within this 2 km height. Significant values in all parameters between 10 and 16 km are indicative of multiple
 340 ~~high~~high-level cloud layers. In the rest of the campaigns, we have noticed that COBALD has captured profile information that was
missing in the lidar data.

~~341—was missing in lidar data.~~

2.4.2. CPS data processing

343 The phase of the cloud particle detected by CPS is determined using a quantity called degree of polarization (DOP) given by
the following relation:

344 ~~given by the following relation:~~

345
$$DOP = \frac{I_{55} - I_{125}}{I_{55} + I_{125}} \quad (3)$$

$$DOP = \frac{I_{55} - I_{125}}{I_{55} + I_{125}} \quad (3)$$

346—Since the spherical particles (water droplets) do not provide significant voltage in the cross-polarization (I125 close to 0), the

347—DOP values for such particles would be close to 1. On the other hand, the DOP for non-spherical particles (for example ice

348—crystals) would take values between -1 and 1 randomly as I125 is non-zero and may or may not be greater than I55. Apart

349—from this, CPS can also detect the non-spherical particles in the lower troposphere whose DOP values may vary between -1 and 1.

350—and 1.

351 The volume of the particle detection area within CPS is non zero and estimated as $\sim 0.5 \text{ cm}^3$ (see section 2.3 of
 352 Fujiwara et al., 2016 for the details). Therefore, when the particle number concentration is greater than $\sim 2 \text{ cm}^{-3}$, more than
 353 one particle would exist simultaneously in the detection area, resulting in particle overlap and multiple scattering and thus a
 354 counting loss. The counting loss occurrence can be identified using a house keeping parameter called ‘particle signal width’
 355 defined as the time taken for detection of a single particle. A simple correction of particle count using the particle signal
 356 width information is proposed by Fujiwara et al. (2016, see their section 2.3 for the details) using a factor ‘f’ which is
 357 (particle signal width in ms)/(1 ms) as follows. The raw counts from a CPS are corrected for multiple scattering and overlap
 358 effects using particle signal width data using Equation 4.

The volume of the particle detection area within CPS is non-zero and estimated as $\sim 0.5 \text{ cm}^3$ (see section 2.3 of Fujiwara et al., 2016
 for details). Therefore, when the particle number concentration is greater than $\sim 2 \text{ cm}^{-3}$, more than one particle would exist simultaneously in
 the detection area, resulting in particle overlap and multiple scattering and thus a counting loss. The counting loss occurrence can be identified
 using a housekeeping parameter called ‘particle signal width’ defined as the time taken for the detection of a single particle. A simple correction
 of particle count using the particle signal width information is proposed by Fujiwara et al. (2016, see their section 2.3 for the details) using a
 factor ‘f’ which is (particle signal width in ms)/(1 ms) as follows. The raw counts from a CPS are corrected for multiple scattering and overlap
 effects using particle signal width data using Equation 4.

$$359 \quad N_{\text{corr}} = N_{\text{meas}} \times 4f^3 \quad (4)$$

360 Finally, the number of particles counted per second is converted to number concentration by assuming that the air flow at the
 361 CPS detection area as 70% of the balloon ascent rate (see Appendices B and C of Fujiwara et al., 2016). The uncertainty of
 362 the number concentration when the above correction to the particle count is made (i.e., for the case of $> \sim 2 \text{ cm}^{-3}$) has not
 363 been evaluated by Fujiwara et al., 2016. It would be safe to assume that the estimated number concentration is valid in the
 364 representation of variations in the cloud property rather than magnitude.

Finally, the number of particles counted per second is converted to number concentration by assuming that the airflow at the CPS detection
 area is 70% of the balloon ascent rate (see Appendices B and C of Fujiwara et al., 2016). The uncertainty of the number concentration when
 the above correction to the particle count is made (i.e., for the case of $> \sim 2 \text{ cm}^{-3}$) has not been evaluated by Fujiwara et al., 2016. It would be
 safe to assume that the estimated number concentration is valid in the representation of variations in the cloud property rather than magnitude.

365 CPS data were analyzed at their actual resolution of ~ 5m. Figure 4a shows the corrected cloud particle (number)
366 count (based on eq. 4) for the same day as shown in ~~fig.~~Figure 3. Significant cloud particle count is found at around 5 km and
from
367 above 10 to 16 km. The number of particles counted per second at 5 km ~~turn~~turns out to be high suggesting the presence of a
368 dense (optically thick) layer of low-level cloud. The corresponding cloud particle number concentration ($\#/cm^3$) also
369 represents (Fig. 4b) the cloud layers at the same altitudes. The DOP is estimated as per Equation 3. In Fig. 4c, DOP values are
370 found to be clustered in the region close to 1 at ~5 km, indicating that the dense (low) cloud layer is a liquid cloud. On the
371 other hand, the DOP values are randomly distributed between -1 and 1 in the altitude region of >10 to 16 km, indicating that
372 these are ice clouds. In Fig. 4d and 4e, particle signal width is often greater than 1 ms and I55 is sometimes ~7.5 V for the
373 ice cloud region between 11 and 14 km suggesting particle overlap and multiple scattering which might have led to signal
saturation. This portion of the profile is more vulnerable to the data correction which has been performed and shown in Fig. 4a.

374 saturation. This portion of the profile is more vulnerable for the data correction which has been performed and shown in Fig.
331 4a.

2.4.3. Lidar data processing

Though the backscattered data at very high altitudes (>30 km) are not significant, it is used as a background signal for noise correction. Range corrected signal (RCS) from MPL/Mie is calculated from noise corrected backscattered signal multiplied with range square. In general, the RCS indicates the intensity of light backscattered from molecules, aerosols and clouds in the atmospheric column. However, inversion techniques are commonly applied to the RCS with an assumption of lidar ratio (the ratio of extinction coefficient to backscattering coefficient) to obtain the profiles of total backscatter coefficient, and extinction coefficient of cloud/aerosol separately. Ground-based lidar data were analyzed at their actual vertical resolutions. However, CALIPSO data were interpolated and processed at every 30 m resolution. This information is used in the discussion (sec 3.1).

2.4.4. Estimation of saturation relative humidity

Two dedicated radiosondes from iMet and Meisei were employed in the balloon campaigns for measurement of meteorological parameters (temperature, pressure, relative humidity, and horizontal winds, with respect to height) as well as to act as interface with specialized sondes COBALD and CPS, respectively. As mentioned, temperature and pressure profiles from the radiosonde were used in post processing of COBALD sonde to scale the signal to the molecular Rayleigh scattering. In addition to this, radiosonde temperature, relative humidity is useful in understanding the state of saturation of water vapor in the column. By convention, relative humidity reported from radiosonde is always over the plane surface of liquid water (because radiosonde relative humidity sensors are factory calibrated) even below 0°C . This is because water droplets may exist even below 0°C and down to -30 to -40°C (in the form of super cooled liquid) in the atmosphere. Saturation relative humidity (SRH) defined in Fujiwara et al. (2016) (see also Fujiwara et al., 2003) as the ratio of saturation vapor pressure over the plane surface of ice (e_{si}) to water (e_{sl}) expressed in units of percentage can be a good metric to describe the state of water vapor in the atmosphere such as sub saturation, saturation and/or super saturation in particular at air temperatures below 0°C (with respect to ice). In this study, both e_{sl} and e_{si} are calculated using Hyland and Wexler formulation (see Appendix A of Murphy and Koop, 2005) by using radiosonde temperature data. For the temperatures warmer than 0°C , water vapor saturation is indicated by 100% RH. For temperatures colder than 0°C , water vapor is said to

~~356 be saturated if $RH = SRH$ and super saturated when $RH > SRH$. This information is used in discussion (sec 3.2).~~

Two dedicated radiosondes from iMet and Meisei were employed in the balloon campaigns for the measurement of meteorological parameters (temperature, pressure, relative humidity, and horizontal winds with height) as well as to act as an interface with specialized sondes COBALD and CPS, respectively. As mentioned, temperature and pressure profiles from the radiosonde were used in the post-processing of the COBALD sonde to scale the signal to the molecular Rayleigh scattering. In addition to this, radiosonde temperature, and relative humidity is useful in understanding the state of saturation of water vapour in the column. By convention, relative humidity reported from radiosonde is always over the plane surface of liquid water (because radiosonde relative humidity sensors are factory calibrated) even below 0°C. This is because water droplets may exist even below 0°C and down to -30 to -40°C (in the form of supercooled liquid) in the atmosphere. Saturation relative humidity (SRH) is defined in Fujiwara et al. (2016) (see also Fujiwara et al., 2003) as the ratio of saturation vapour pressure over the plane surface of ice (e_{si}) to water (e_{sl}) expressed in units of percentage can be a good metric to describe the state of water vapour in the atmosphere such as sub-saturation, saturation and/or super-saturation in particular at air temperatures below 0°C (with respect to ice). In this study, both e_{sl} and e_{si} are calculated using Hyland and Wexler formulation (see Appendix A of Murphy and Koop, 2005) by using radiosonde temperature data. For temperatures warmer than 0°C, water vapour saturation is indicated by 100% RH. For temperatures colder than 0°C, water vapour is said to be saturated if $RH \sim SRH$ and super-saturated when $RH > SRH$. This information is used in the discussion (sec 3.2).

2.4.5. Discrimination of cloud and aerosol in a balloon profile

COBALD measurement always represents backscatter light from the combination of aerosol and cloud. Obtaining information on aerosol (only) is not possible (for COBALD) in the presence of clouds, and the corresponding regions have to be identified and rejected. This cloud clearing has been established previously for studies related to the UTLS region (Vernier et al., 2015, 2018). Contrary, for cloud investigation, the COBALD was used in combination with the Cryogenic Frost point Hygrometer (CFH) to identify super saturation (with respect to ice) below, above and within the cirrus clouds to improve the understanding of microphysical processes in cirrus clouds (Cirisan et al., 2014). This sonde in addition detected volcanic aerosol tracers in the stratosphere (Vernier et al., 2020). The Asian Tropopause Aerosol Layer (ATAL) is a well-documented phenomenon occurring in the UTLS region during the Summer Monsoon Season over South Asia. Vernier et al. (2015) proposed two cloud clearing methods for discrimination of aerosol from cirrus clouds in ATAL region using the physical quantities Color Index (CI), relative humidity over ice (RHi) and backscatter ratio (BSR) at 940 or 532 nm (the latter was interpolated from the 455 nm data for inter-comparison with CALIOP). In the presence of CFH data, the RHi

cloud filtering approach classifies ATAL/UTLS aerosol layers by the criterion $BSR \text{ (at } 532 \text{ nm)} < 1.3$ and $RHi < 70\%$. For measurements of COBALD alone, the CI method indicates clouds with $CI < 7$ and $BSR \text{ (at } 940 \text{ nm)} < 2.5$. It was shown that both methods effectively discriminate ATAL aerosol from upper tropospheric thin clouds. Brunamonti et al. (2018) also applied the cloud clearing criteria ($BSR \text{ at } 940 \text{ nm} < 2.5$, $CI < 7$ and $RHi < 70\%$) following Vernier et al. (2015) and found a clear signal of enhanced BSR (at 455 nm) between 1.04 and 1.12 indicative of the aerosol population in the ATAL region. However, it is noted that the methods proposed by Vernier et al. (2015) and Brunamonti et al., (2018) were developed for the UTLS aerosol and their applicability to COBALD measurements of boundary layer and/or mid tropospheric aerosol needs to be validated.

In the present study, we made use of a CPS sonde in tandem with COBALD. As already mentioned, CPS is sensitive to particles in the size range of $>2 \mu\text{m}$ and hence detects clouds particles (both liquid droplets and ice crystals) and sometimes coarse mode aerosol particles (such as dust) of these sizes. Fujiwara et al. (2016) has demonstrated in detail the potential of a CPS sonde using balloon sounding carried out at mid latitude (Japan) as well as tropical sites (Indonesia). Narendra Reddy et al. (2018) have used a CPS measurement from Gadanki to validate their method of retrieving cloud

vertical structure based on radiosonde measurements. Therefore, to better segregate the clouds from aerosols in the COBALD measurements, CPS sonde has added advantage to the methods using simultaneous RH data described by Vernier et al. (2015) and Brunamonti et al. (2018). This implies wherever the cloud present in a profile, CPS identifies it (along with its phase) and the corresponding COBALD particle backscatter data refers to the cloud. The rest of the particle signals in the COBALD profile should correspond to aerosol. However, it may correspond to the (thin) cloud also which might have been missed or undetected by a CPS. So identification of aerosol and cloud in an altitude profile is key measurement of this paper. The concept is illustrated in sec 3.2.

COBALD measurement always represents backscatter light from the combination of aerosol and cloud. Obtaining information on aerosol (only) is not possible (for COBALD) in the presence of clouds, and the corresponding regions have to be identified and rejected. This cloud clearing has been established previously for studies related to the UTLS region (Vernier et al., 2015, 2018). Contrary, for cloud investigation, the COBALD was used in combination with the Cryogenic Frost point Hygrometer (CFH) to identify supersaturation (with respect to ice) below, above and within the cirrus clouds to improve the understanding of microphysical processes in cirrus clouds (Cirisan et al., 2014). This sonde in addition detected volcanic aerosol tracers in the stratosphere (Vernier et al., 2020). The Asian Tropopause Aerosol Layer (ATAL) is a well-documented phenomenon occurring in the UTLS region during the Summer Monsoon Season in South Asia. Vernier et al. (2015) proposed two cloud clearing methods for discrimination of aerosol from cirrus clouds in the ATAL region using the physical quantities Color Index (CI), relative humidity over ice (RHi) and backscatter ratio (BSR) at 940 or 532 nm (the latter was interpolated from the 455 nm data for inter-comparison with CALIOP). In the presence of CFH data, the RHi cloud-filtering approach classifies ATAL/UTLS aerosol layers by the criterion $BSR \text{ (at 532 nm)} < 1.3$ and $RHi < 70\%$. For measurements of COBALD alone, the CI method indicates clouds with $CI < 7$ and $BSR \text{ (at 940 nm)} < 2.5$. It was shown that both methods effectively discriminate ATAL aerosol from upper tropospheric thin clouds. Brunamonti et al. (2018) also applied the cloud clearing criteria ($BSR \text{ at 940 nm} < 2.5$, $CI < 7$ and $RHi < 70\%$) following Vernier et al. (2015) and found a clear signal of enhanced BSR (at 455 nm) between 1.04 and 1.12 indicative of the aerosol population in the ATAL region. However, it is noted that the methods proposed by Vernier et al. (2015) and Brunamonti et al., (2018) were developed for the UTLS aerosol and their applicability to COBALD measurements of boundary layer and/or mid-tropospheric aerosol needs to be validated.

In the present study, we made use of a CPS sonde in tandem with COBALD. As already mentioned, CPS is sensitive to particles in the size range of $>2 \mu\text{m}$ and hence detects cloud particles (both liquid droplets and ice crystals) and sometimes coarse mode aerosol particles (such as dust) of these sizes. Fujiwara et al. (2016) have demonstrated in detail the potential of a CPS sonde using balloon sounding carried

out at mid-latitude (Japan) as well as tropical sites (Indonesia). Narendra Reddy et al. (2018) used a CPS measurement from Gadanki to validate their method of retrieving cloud vertical structures based on radiosonde measurements. Therefore, to better segregate the clouds from aerosols in the COBALD measurements, CPS sonde has added advantage to the methods using simultaneous RH data described by Vernier et al. (2015) and Brunamonti et al. (2018). This implies wherever the cloud is present in a profile, CPS identifies it (along with its phase) and the corresponding COBALD particle backscatter data refers to the cloud. The rest of the particle signals in the COBALD profile should correspond to aerosol. However, it may correspond to the (thin) cloud also which might have been missed or undetected by a CPS. So identification of aerosol and cloud in an altitude profile is the key measurement of this paper. The concept is illustrated in sec 3.2.

389 **2.4.6. Estimation of Aerosol-cloud-interaction Index**

390 Balloon data from all campaigns can be pooled to explore the aerosol-cloud relationship. For this purpose, a simple
391 scheme is developed to carry out the required computations. CPS profile data is looked for a cloud layer ~~presence~~present in the
392 altitude regime of liquid or low-level clouds (below 5 km). As already discussed, CPS also identifies ~~particle~~particles of non-
393 spherical nature. ~~In order to~~To separate cloud particles from non-spherical particles, the following conditions have been
394 imposed on various CPS measured parameters. Cloud particle count should be >10 #/s, cloud droplet number concentration
395 >10⁻³#/cc, DOP>0.6, relative humidity >95% and temperature >0 degC. As there is a chance of randomly distributed data
396 points in the measurement column satisfying the above conditions, we considered only those points present continuously up
397 to a thickness minimum of 100 m (with at least one point for every 40 m). Further, COBALD data of blue backscatter ~~from~~
398 100m, 200m, 300m, 400m and 500m below the cloud base has been picked up separately (for the same profile) as a proxy of
399 aerosol to check its influence on the cloud above. As already mentioned, post-processed data of backscatter ratio from
400 COBALD sonde represents the contribution from both molecule and particle (cloud and/or aerosol). Hence, the particle
backscatter
401 ratio is obtained by subtracting the backscatter ratio from one. ~~In order to~~To avoid high values of particle (blue) backscatter ratio
402 possibly originating from the interaction with high relative humidity usually expected near to cloud base (boundaries), we
403 have adopted two methods. First, high values of particle (blue) backscatter below the cloud base are removed if beyond a
404 threshold value of 3.15. The threshold is arrived at using a box plot (figure not shown) drawn for all the particle backscatter
405 data set (for sounding with clouds) from cloud base to 500 m below and found that 3.15 corresponds to the upper whisker

406 $-(Q3+1.5*(Q3-Q1))$). Further, the particle backscatter data is corrected for relative humidity in case a statistically significant (p-value ≤ 0.05) and good correlation (> 0.71) is found among relative humidity and particle backscatter ratio. A typical example from the scheme is shown in Fig. 5 for the launch conducted on 01 November 2018 which depicts cloud layers, blue particle backscatter ratio below the cloud along with shaded black dots (representative of aerosol backscatter ratio). The scheme is applied to the balloon sounding and the results were discussed in sec 3.4.

(p value ≤ 0.05) and good correlation (> 0.71) is found among relative humidity and particle back scatter ratio. A typical example from the scheme is shown in Fig. 5 for the launch conducted on 01 November, 2018 that depicts cloud layers, blue particle back scatter ratio below cloud along with shaded black dots (representative of aerosol back scatter ratio). The scheme is applied to the balloon sounding and the results were discussed in sec 3.4.

Aerosol-cloud interaction can be quantified based on an index (ACI) using three methods discussed in Feingold et al., 2003, 2006. ACI is defined as slope of the linear fit between logarithm of cloud proxies such as cloud optical depth, cloud particle radius and cloud droplet number with logarithm of aerosol proxy. ACI in this study has been estimated using the equation (5).

$$ACI = \frac{d \log N_c}{d \log BSR_b} \quad (5)$$

where Aerosol-cloud interaction can be quantified based on an index (ACI) using three methods discussed in Feingold et al., 2003, 2006. ACI is defined as the slope of the linear fit between the logarithm of cloud proxies such as cloud optical depth, cloud particle radius and cloud droplet number with the logarithm of aerosol proxy. ACI in this study has been estimated using the equation (5).

$$ACI = \frac{d \log N_c}{d \log BSR_b} \quad (5)$$

Where cloud droplet number count (N_c) is taken as cloud proxy whereas BSR_b is the COBALD (blue) particle back scatter backscatter is (BSR_b) taken as aerosol proxy and interaction between both is indicated by index ACI. It is to be noted that cloud particle number concentration is used here to represent cloud property instead of droplet number concentration as the former is a direct measurement (of CPS). The slope of the linear fit between the natural logarithm of N_c and BSR_b indicates the magnitude of the aerosol-

cloud interaction (ACI) index which should be between 0 and 1 (Feingold et al., 2003). (Feingold et al., 2003). Note this the condition (shown in eq.5) is

independent of the liquid water path as it verifies/quantifies the aerosol activation process.

2.4.7. Uncertainty in ACI estimation

The uncertainty in ACI stems from both uncertainty/uncertainties in the COBALD backscatter ratio and CPS cloud particle counts.

The slope of the curve (linear fit of data on a log-log scale) can be written as a function of BSR_b (blue back scatter backscatter

ratio) and N_c

425 (cloud particle

426 count) as,

$$ACI = f(BSRb, N_c) = \frac{\log N_c - C}{\log BSRb} \quad (6)$$

$$\text{where } ACI = f(BSRb, N_c) = \frac{\log N_c - C}{\log BSRb} \quad (6)$$

427 Where 'C' is the intercept of the curve. ~~Partial~~ The partial derivative of $f(BSRb, N_c)$ ~~with respect to BSRb and N_c~~ indicates
uncertainty in

428 ACI with respect to uncertainty in individual parameters (N_c and BSRb). The combined uncertainty (UC) in ACI is given by the
equation.

429 the equation,

$$430 UC = \sqrt{\left(\frac{\partial f(BSRb, N_c)}{\partial BSRb} \right)^2 (uBSRb)^2 + \left(\frac{\partial f(BSRb, N_c)}{\partial N_c} \right)^2 (uN_c)^2} \quad (7)$$

$$\text{where } UC = \sqrt{\left(\frac{\partial f(BSRb, Nc)}{\partial BSRb}\right)^2 (uBSRb)^2 + \left(\frac{\partial f(BSRb, Nc)}{\partial Nc}\right)^2 (uNc)^2} \quad (7)$$

Where $uBSRb$ and uNc are individual uncertainties.

3. Results

The multi-instrument data from the BACIS campaigns are presented in this section. Consistency among multiple measurements is discussed in Section 3.1, data from a particular balloon sounding (campaign) are interpreted in detail in Section 3.2, statistics on cloud/aerosol features are given in Section 3.3, and finally, the relationship between aerosol and cloud is illustrated in Section 3.4.

3.1. Consistency. Comparison of balloon measurements

The combination of COBALD and CPS sondes is used for the first time for in situ measurement of aerosols and clouds. Therefore, it is important to know the performance of these sondes in comparison to other measurement techniques.

Here, we make use of data from two pilot campaigns to demonstrate the consistency of balloon-borne measurements with that of ground-based and spaceborne remote-sensing instruments. As mentioned previously, the first two (pilot) campaigns have been conducted in line with the proposed concept.

Here, we make use of data from two pilot campaigns to demonstrate the consistency of balloon-borne measurements with that of ground-based and space-borne remote-sensing instruments. As mentioned previously, the first two (pilot) campaigns have been conducted in line with the proposed concept.

3.1.1. Pilot campaign-1 (launch held on 06 June 2017 at 01:50 LT)

The CALIPSO satellite overpass time for the first pilot campaign was around 02:00 LT on 06 June 2017 (starting time of the track). The balloon was launched at 01:50 LT on the same day just before CALIPSO overpass time. Combined measurements from specialized balloon-borne sondes and ground-based and space-borne lidars obtained during the first launch of the campaign are shown in Figure 6.

Measurements from specialized balloon-borne sondes, ground-based and space-borne lidars obtained during the first launch of the campaign are shown in Figure 6.

449 The BSR from COBALD sonde at 455 nm (950 nm) is plotted in Fig. 6d as a blue (red) line. BSR from both ~~the~~
450 channels ~~are~~is referenced to the same x-axis scale. Similarly, cloud particle number concentration (dN, #/cc) from CPS sonde is
451 plotted as black dots (Fig.6e). On the other hand, range corrected signal (RCS) from ground-~~based~~ lidars (Mie, MPL) is
452 averaged over a short period ~~of time~~ during the CALIPSO overpass and plotted in magenta (averaged from 01:50 to 02:00LT),
453 orange ~~color~~colour lines (averaged from 01:50 to 01:55 LT), respectively (Fig.6f). The total attenuated backscatter ($\text{km}^{-1} \text{sr}^{-1}$) from
454 CALIPSO is also averaged for the profiles found nearest to the location and shown in an olive green ~~color~~colour line (Fig.6f). The
455 significant peaks in physical quantities being compared among the different measurements are representative of ~~response~~

456—responses from clouds and aerosols in the atmosphere. At this point of discussion, we have not distinguished their contributions.
The

457—balloon drifts away from the launch location with time, therefore, it is also required to check the degree of co-location of
458—measurements with the lidars. ~~In order to~~To facilitate this, a portion of nocturnal variation (representing the balloon launch
459—duration) in range corrected signal from both Mie and MPL is shown in Fig. 6b and 6c, respectively. The CALIPSO
460—overpass track consisting of 166 profiles is also plotted as a function of longitude (Fig. 6a). For the sake of easy
461—identification of simultaneous lidar measurements, the balloon indices such as height and drift (radial distance from launch

location) are overplotted as a function of time on contour maps as shown in black and red-coloured lines, respectively (Fig. 6b and 6c).

462—~~location) are over plotted as a function of time on contour maps as shown in black and red colored lines, respectively (Fig.~~
463—~~6b and 6c).~~

464—Balloon—borne in-situ measurements from COBALD and CPS show significant peaks in the lower tropospheric
465—(below 4 km) and upper troposphere (between 13 and 17 km) at the same altitude regions. It can be seen from ~~the~~ Fig. 6d and 6c,
466—that there is a good resemblance ~~amongbetween~~ the in-situ and MPL measurements in the lower tropospheric (below 4km). This is
467—because almost no change in the atmospheric conditions as the balloon took approximately 15 minutes to reach an altitude of
468—4 km with a radial distance of 5 km away from the launch location. Mie lidar information is not reliable for this altitude
469—region (below 4 km) as it is not in the overlapping region of the telescope viewing geometry and laser beam dispersion (see
470—section 2). CALIPSO signal also looks to be dispersed and noisy for this altitude region. This could be due to the attenuation
of the signal from the top side layers as seen in Fig. 6a at a longitude of 79.24° E (nearest profiles longitude).

471—~~of the signal from top side layers as seen in Fig. 6a at longitude of 79.24° E (nearest profiles longitude).~~

472—Next to this is the sharp peak seen in COBALD red channel at slightly below 9 km (Fig. 6d). This again can be seen
473—in Mie and MPL profiles also (Fig. 6b, 6c) but at 8.4 km (slightly below cloud detection height). However, it is to be noted
474—that these profiles are averaged for a short duration of time during the CALIPSO overpass. ~~In fact, there~~There is another peak in
475—the Mie lidar profiles at ~7.2 km, (Fig. 6b), which is not seen in COBALD. It is approximately 45 min (around 02:45 LT)
476—from the time of launch when the balloon reached the altitude of ~9 km and 5.8 km away before detecting a sharp peak. As
477—there is no significant range corrected signal during this time and altitude in the ground—based lidar data (Fig. 6b and 6c), the
478—sharp layer detected by COBALD may be a localized cloud layer or a passing layer which might have ascended/descended.

~~479~~ _Exact attribution can be made with a detailed study but it is beyond the scope of the current analysis.

Further, the balloon drift was within a 10 km range until 03:00 LT when it reached heights of ~12 km. This implies weak horizontal winds and thus ~~weak~~weakly associated wind drifts as well. Thereafter, the balloon started drifting rapidly due to high wind speeds between 10 and 20 m/s. Both the in-situ measurements of COBALD and CPS show strong double peaks from ~13-15.5 km and 16-16.5 km (Fig. 6d, e). Profiles from Mie, MPL and CALIPSO also showed similar peaks except for MPL for which the upper side peak is missing (Fig. 6f). It may be once again noted that, these profiles are averaged for a short duration of time during the CALIPSO overpass the and return signal from MPL at high altitudes (~16 km) during the same time suffered severely due to the presence of a mid-tropospheric cloud layer (at ~7 km) as seen in Fig. 6c. This is not the case for the return signal from Mie Lidar as the power and energy of the Mie laser ~~is~~are relatively high (Fig. 6b). However, strong double peak structures can be noticeable in the simultaneous observations of both ground-based lidars (Mie and MPL) at similar heights during the time corresponding to the balloon altitude of 13 km (post 03:00 LT). Therefore, the same upper tropospheric cloud layers detected in the ground, ~~space-borne~~spaceborne and in-situ measurements suggest they are extended cloud layers. Dynamical aspects of ~~south-west~~the southwest monsoon over the sub-continent ~~refers~~refer to the presence of Tropical Easterly Jet (TEJ)

which is strong enough to swipe anvil clouds of ~~meso-scale~~mesoscale convective systems to thousands of ~~kilo-meters~~kilometres (Sathiyamoorthy et al., 2013).

~~et al., 2013).~~

3.1.2. Pilot campaign -2 (launch held on 08 July 2017 at 01:35 LT)

The starting time of the CALIPSO ~~over-pass~~overpass track for the second pilot campaign was at 02:00 LT. The balloon was launched at 01:35 LT nearly 30 minutes before the starting time of the CALIPSO overpass. Data from all the instruments are plotted in Figure 7, which is prepared the same as Figure 6. MPL, and Mie profiles were averaged from 01:50 to 02:00 LT (close to the CALIPSO overpass time over Gadanki).

The observations from COBALD and CPS are matching reasonably well (Fig. 7d, e) as significant peaks were found in the lower troposphere (0-5km) and upper troposphere (10-16 km). The profiles from ~~space-borne~~spaceborne and ground-based

~~501~~—lidars (Fig. 7f) also show a similar response as in-situ measurements (both in the lower and upper troposphere) except that lidar
~~502~~—measurements exhibit additional peaks in the mid-troposphere (between 5 and 10 km). It is to be noted that profiles from lidar
measurements are averaged over a short period, as mentioned before.

~~503~~—lidar measurements are averaged over a short time period, as mentioned before.

504 Simultaneous observations from both the ~~space borne~~spaceborne (CALIPSO) and ground-based (Mie and MPL) lidars
 505 are shown in
 506 Fig. 7 a, b & c respectively. Due to high wind speeds (10-20 m/s) the balloon drifted about 5 km away from the launch site
 507 while crossing boundary layer height (~2km). The features found within the boundary layer as measured by in-situ
 508 instruments (Fig. 7d) are in agreement with that of MPL measurements (Fig. 7c) for the same altitude region. Note that, Mie
 509 lidar measurements are not reliable at these low altitudes and CALIPSO has not yet started passing by the launch site. The
 510 balloon continued to drift away but with the reduced wind speed of 10 m/s. At around 4.3 and 4.7 km (10 km away
 511 from the launch site), the balloon had detected two layers (strong peaks). The time corresponding to this balloon height was
 512 around 01:50
 513 LT and at this point of time, two layers can also be seen in both the ground-based lidars at the same altitudes (Fig. 7b and c)
 514 indicating the presence of an extended layer (which is evident in both the in-situ and ground-based measurements). In fact,
 515 the layer
 516 at 4.7 km was also noticeable in the CALIPSO profile measurements (Fig. 7a). This is because the CALIPSO started coming
 517 close by to the site when the balloon was at this height and the CALIPSO profile corresponding to an average of
 518 (nearest) profiles at
 519 around 79.32° E longitude (Fig. 7a). Further, the balloon started drifting towards the launch site until it reached a height of
 520 ~7.5 km at a distance of ~13 km away. While moving towards the site, the balloon started detecting the layers starting from
 521 11 km. The time corresponding to the balloon height of 11 km is around 02:45 LT and at this point of time simultaneous
 522 MPL data show almost weak returns (Fig. 7c), whereas Mie lidar shows a better return signal (Fig. 7b) than MPL. In
 523 continuation of this, the balloon started drifting further towards the site until it reached as close as ~3.5 km at a height of
 524 ~12.5
 525 km. Thereafter, it started moving rapidly away from the location with high wind speeds due to the characteristic of TEJ.
 526 Multiple layers of clouds have been nicely captured by in-situ measurements from 11 km to ~ 16 km. However, prominent
 527 lidar returns were not noticeable in the simultaneous observations of Mie and MPL. This is because of a strong lower
 528 tropospheric cloud layer present at around 5 km limiting the detection of upper tropospheric cloud layers by both ground-
 529 based lidars. However, all these layers were prominently captured in CALIPSO observations as it is top-down laser probing.

In summary, the data from both pilot campaigns illustrate the limitations of the ground-based and/or spaceborne lidars in
 detecting the complete cloud vertical structure. At the same time, in-situ data emphasize reasonable agreement of the balloon-borne

measurement with the ground-based as well as space-borne measurements and add to the remote sensing techniques while detecting the missing portion of the cloud vertical structure.

~~525 In summary, the data from both the pilot campaigns illustrate the limitations of the ground based and/or space borne lidars in~~
~~526 detecting the complete cloud vertical structure. At the same time, in situ data emphasize the consistency of the balloon borne~~
~~527 measurement with the ground based as well as space borne measurements and complements to the remote sensing technique~~
~~528 while detecting the missing portion of the cloud vertical structure.~~

529 A typical example of high-resolution vertical wind measurements obtained from MST Radar ~~during~~ on 8 July 2017 is
 530 shown in Figure 8(f) and profiles of all the three-dimensional winds averaged between 02:30 LT to 03:30 LT are shown in
 531 Figures 8(a)-(c) to compare the wind measurements. We also superimpose the zonal and meridional winds in the respective
 532 panels obtained from radiosonde for comparison. Consistency in the measured winds in these two independent techniques
 533 can be noticed. Since this campaign falls ~~in~~ during the Indian Summer Monsoon season, easterly wind velocities exceeding 50 m/s,
 534 which is called ~~as~~ TEJ, can be noticed between 14-16 km altitudes as a part of synoptic-scale systems (Fig. 8a). In addition,
 535 zonal winds are westerly, which is also part of a large-scale monsoon system. These winds play a crucial role in bringing
 536 clouds and aerosol from far away sources. In general, meridional winds are weaker and ~~mostly~~ most southerly (Fig. 8b). Vertical
 537 winds show mostly updrafts, except in the UTLS region where downdrafts are noticed (Fig. 8c) and similar features persist
 538 through this campaign (Fig. 8f). Occasional patches of updrafts and downdrafts can be noticed during the campaign, which is
 539 associated with monsoon convection. These vertical ~~wind acts~~ winds act in the upliftment of aerosol and clouds. Enhanced SNR
 layers are
 540 also noticed (Fig. 8d) at a few altitudes mostly related to large ~~temperature~~ temperatures and water ~~vapor~~ vapour gradients generally
 occur in the
 541 presence of clouds. Doppler width (Fig. 8e) shows higher values below the boundary layer and UTLS region suggesting

active turbulence.

542 ~~active turbulence.~~

543 3.2. Interpretation of aerosol and cloud features in a balloon profile

544 ~~In order to fulfil~~ To fulfil the primary objectives of the campaign, it is a priority to distinguish aerosol and cloud in a
 balloon
 545 borne in-situ profile. In connection with this, combined measurements of CPS and COBALD from a balloon sounding held
 546 on 27 June 2019 at 23:30 LT ~~is~~ are interpreted as shown in Figure 9. This particular sounding is selected because it showcases
 547 all the features that can be detectable by a CPS sonde in a profile such as liquid cloud, ~~super-cooled~~ supercooled liquid cloud, ice
 cloud,
 548 and non-spherical particle layers. INSAT3D brightness temperature shown in Figure S1 indicates the evolution of a localized

cloud system north of the observational site initiated a few hours before the launch and eventually spreading over the site.

549 ~~cloud system north of the observational site initiated few hours before the launch and eventually spreading over the site.~~

550 To characterize the background conditions of the atmosphere, meteorological parameters such as relative humidity
551 (RH), and temperature (T) obtained from RS-11G radiosonde are plotted in Fig. 9a (wine red and blue ~~color~~colour lines). In the
Fig.
552 9a, SRH is also shown (in yellow ~~color~~colour). The SRH and RH can be read from the same top-X scale in wine red ~~color~~colour
as shown in
553 Fig. 9a.

554 The CPS sonde usually features clouds that can be better identified with the information based on DOP,
 555 and corresponding profiles of T, RH, and SRH. From Fig. 9d, DOP values close to 1 (from 0.6 to 1) are noticeable at different
 556 altitude ranges in the profile viz., 3.5 to 5.5 km, 8.6 to 9 km and DOP values spread (-1 to 1) between 9 and 11 km. In the
 557 altitude range from 3.5 to 5.5 km, CPS detected multiple liquid cloud layers, corresponding to the multiple layers of 100%
 558 RH. However, the corresponding COBALD blue and red backscatter data points are limited (Fig. 9b). This is because
 559 COBALD backscattered signals showed missing values due to saturation of ~~photo diodes~~photodiodes in the presence of thick
 liquid
 560 cloud layers and that had to be removed during post-processing of data and are not discussed further.

561 The layer extending between 3.5 and 3.8 km (300 m thick) is observed with RH and T in the range 99-100% and 7-
 562 8.7⁰C, respectively, indicating saturation of water ~~vapor~~vapour with respect to liquid (RH~SRH) which is conducive ~~for~~to the
 563 formation of a (liquid) cloud. Further, the majority of droplet number ~~concentration~~concentrations in this liquid cloud layer range
 between 0.1
 564 to 1 #/cm³. A rough estimate ~~on~~of particle size information (water droplet or ice crystal) can be inferred from CPS voltage data
 565 (I55). According to Fujiwara et al. (2016), I55 mostly lying below 1V suggests these droplets are sized ~2-13 μm. Another
 566 liquid cloud layer extending from 4 to 4.4 km (400 m thick) is observed with ~~vapor~~vapour saturation over liquid (100% RH) and
 567 temperatures from 3-6⁰C. CPS shows that droplet number concentration peaks in the range 0.1-10 #/cm³ with the highest in 0.1-
 568 1 #/cm³. The intensity (I55) values (<1 V) indicate the majority of droplet sizes are ~2-13 μm. The third liquid layer in the range
 569 of 3.5 to 5.5 km is observed between 5.1-5.5 km (400 m thick) with the highest droplet number concentrations in the range of 0.1-
 10
 570 #/cm³, sized around 2-13 μm (I55<1 V). However, RH observations show 100%RH or RH>SRH ie. water ~~vapor~~vapour super-
 571 saturated over ice at temperatures slightly below 0⁰C (0 to -3⁰C), suggesting that the cloud layer may be composed of ~~super~~
 572 ~~cooled~~supercooled liquid droplets. Another clear ~~super-cooled~~supercooled cloud layer was detected between 8.6 and 9 km (400 m
 thick) with super-
 573 saturation of ~~vapor~~vapour over ice at 100%RH or RH>SRH and -21.5 to -23.5⁰C temperatures. The observed features of droplet
 574 number concentration and particle size are similar to those ~~for~~of the ~~super-cooled~~supercooled cloud found in the lower
 atmosphere. The

~~575~~ _only difference that could be noticeable is in the distribution of DOP values as shown in Figure S2, which ~~indicate the~~
~~more~~indicates the tendency of droplets toward non-sphericity in the mid-tropospheric supercooled liquid cloud. COBALD signals were found
limited for all liquid/supercooled layers discussed above.

~~576—tendency of droplets towards non-sphericity in the mid-tropospheric super-cooled liquid cloud. COBALD signals found~~
~~577—limited for all liquid/super-cooled layer discussed above.~~

~~578~~ The ~~top-most~~topmost layer in the upper troposphere spreading from 9.5-11 km is an ice cloud layer as per its DOP values.

~~579~~ The temperatures within the cloud are found in the range of -22 to -40°C. RH values are >SRH, suggesting the super-saturation

~~580~~ of ~~vapor~~vapour (over ice) within the ice cloud. ~~Histogram~~ The histogram of data for all the parameters obtained from COBALD and CPS for this

~~581~~ ice cloud layer (9-11 km) is shown in Figure 10. The number concentration of ice cloud particles (Fig. 10a) lies between 0.01

~~582~~ to 10 #/cm³ with a peak in the range of 0.1-1 #/cm³. Non-sphericity of particles is ~~clearly~~ seen by the wide distribution of DOP

~~583~~ values in the range -0.4 to 1 with the majority of them lying close to 0 (Fig. 10b). In particular, DOP values close to 0 indicate

~~584~~ (see section. 2) that both plane and cross-polarization intensities of scattered light (I55 and I125) are comparable. This happens

~~585~~ when both detectors get saturated due to a large number of small size particles and/or a few large-sized ice particles or both. In

~~586~~ support of this, the I55 values (Fig. 10c) are found to peak in the 7-8 V range (~7.5 V) for such cases. Further, if saturation

~~587~~ voltages are due to large size then they may correspond to ~80-140 μm or greater ice particles (corresponding to I55 of

~~588~~ ~7.5V), assuming that the results from laboratory experiments by Fujiwara et al. (2016) using standard spherical particles

~~can be applied for these ice clouds. Apart from this, the second peak in I55 noticed below 1V corresponds to ice particles roughly sized between 2 and 14 μm.~~

~~589~~ can be applied for these ice clouds. Apart from this, a second peak in I55 noticed below 1V corresponds to ice particles

~~590~~ roughly sized between 2 and 14 μm.

~~591~~ The COBALD BSR corresponding to this ice cloud ~~are~~is symmetrically distributed from 1-10 and 10-100 for blue

~~592~~ (Fig. 10d), red (Fig. 10e) wavelengths, respectively. However, there are some observations which are beyond 10(100) at blue

~~593~~ (red) wavelengths. Similarly, the CI for this cloud (Fig. 10f) is found mostly between 10 and 20 but for a few instances, it is

~~594~~ observed from 20 to 40. From the definition (see section 2), the CI is independent of the number concentration hence it can

~~595~~ be used as an indicator of the mode radius of particles. With the assumption of ~~at~~the single-mode log-normal size distribution of

~~596~~ spherical aerosol/cloud particles, Mie calculations show CI is 4-10 for small particles of mode radius up to 1-2 μm and 14-20

~~597~~ for large particles of 2-20 μm. CI converges to around 20 as a geometric limit for very large particles of mode radius > ~50

~~598~~ μm. However, CI can have values >20 at mode radius 2-20 μm as CI is a non-monotonous function of mode radius and

~~599~~ exhibits Mie oscillations (due to variations of scattering efficiencies with size parameter). The amplitude and frequencies of

~~600~~ Mie oscillations depend on the width of the log-normal size distribution assumed. At width higher than say 2 (represent poly

601—disperse aerosol populations) these oscillations are mitigated and lead to monotonous dependency of CI and mode radius.

602—For stratospheric aerosols in the size range 0.02–0.4 μm the CI is found to be in the range 5–7 (Rosen and Kjome, 1991). This

603— Mie oscillations depend on the width of the log-normal size distribution assumed. At a width higher than say 2 (representing
polydisperse aerosol populations), these oscillations are mitigated and lead to a monotonous dependency of CI and mode radius.
604— For stratospheric aerosols in the size range of 0.02-0.4 μm , the CI is found to be in the range of 5-7 (Rosen and Kjome, 1991). This
is because stratospheric aerosols exhibit size distributions with narrow standard deviations. Aerosol size distributions in the

605— UTLS region may also be assumed as log-normal (similar to stratospheric aerosols) hence the criteria $\text{CI} < 7$ might have

606— suited for cloud filtering in the ATAL region (see Section 2). For the present case of the ice cloud layer (9-11 km) discussed above,

607— CPS indicates the presence of small (2-14 μm) and very large ice particles ($> 80 \mu\text{m}$). So, the standard deviation of log-normal

608— size distribution in the cloud layer of large particle mode must be wider. Therefore, Mie oscillations may be expected to be

609— at a minimum. Probably because of this, the majority of CI values for the cloud layer are found between 15 and 20, which may

610— correspond to a mode radius of $> \sim 50 \mu\text{m}$ (geometric limit). It may also be concluded that the CI of 20-40 (with very few

611— values > 30) corresponds to small particles of mode radius $> 2\text{-}20 \mu\text{m}$ (due to Mie oscillations). COBALD size interpretations

(based on CI) are in support of CPS-based size interpretations. Since the majority of CI falls between 15 and 20, the I55 of $\sim 7.5\text{V}$ in CPS
would have been caused by large size particles.

612— (based on CI) are in support of CPS based size interpretations. Since the majority of CI falls between 15 and 20, the I55 of

613— $\sim 7.5\text{V}$ in CPS would have been caused by large size particles.

614— In the lower troposphere up to 2 km where water vapor is well sub saturated (50-70 %RH), CPS also shows particle

615— signals (Fig. 9c). The DOP values range from 0.4 to 1 but with lower number concentrations ($0.001\text{-}0.01 \text{ \#}/\text{cm}^3$) and less

616— than 1 V of backscatter intensity (I55), indicating these particles as non-spherical in shape similar to the ice cloud particles.

617— Since it is not possible to have ice cloud particles at these lower altitudes in dry conditions ($\text{RH} < 70\%$), it may be possible

618— that these particles are coarse mode non-spherical aerosol particles. COBALD observations indicate CI of 11-12. Thus, both

619— the COBALD and CPS observations indicate aerosol may be of size $2\text{-}5 \mu\text{m}$. To investigate the possible origin of these

620— coarse mode aerosol particles, Hysplit 7 day back trajectories for 5 days before and after the date of launch are calculated

621— and shown in Figure S3 (in different color lines). These Hysplit back trajectories (Stein et al., 2015) indicate the air parcel

622— path ways ending at every 1 km altitude from 1 to 5 km over Gadanki at the time of balloon launch (18 UTC). It can be seen

623— (from Fig. S3) that, the air masses were originated from the Indian Ocean passing through the Arabian Sea before reaching

624— the Gadanki location for heights 1 to 3 km. Therefore, the air masses were of marine origin, and the particles were possibly

coarse mode water soluble particle (such as sea salt) which can grow hygroscopic due to the availability of moisture over the

~~625—Ocean surface (Mishra et al., 2010; Ratnam et al., 2018). The rain water chemical analysis reported by Jain et al. (2019) at~~
~~626—Gadanki supports this conclusion as they found dominance of water soluble ions during the southwest monsoon (June to~~
~~627—September). Above 3 km altitude, the air masses are coming from the Saharan desert region within 7 days which may bring~~

628 ~~non spherical coarse mode dust particles to the launch location (Mishra et al., 2010). Thus, in case of lower tropospheric~~

629 ~~coarse mode aerosol (water soluble aerosol particles), the CI can be >7 at RH<70%.~~

In the lower troposphere up to 2 km where water vapour is well sub-saturated (50-70 %RH), CPS also shows particle signals (Fig. 9c). The DOP values range from -0.4 to 1 but with lower number concentrations (0.001-0.01 #/cm³) and less than 1 V of backscatter intensity (155), indicating these particles as non-spherical in shape similar to the ice cloud particles. Since it is not possible to have ice cloud particles at these lower altitudes in dry conditions (RH<70%), it may be possible that these particles are coarse mode non-spherical aerosol particles. COBALD observations indicate a CI of 11-12. Thus, both the COBALD and CPS observations indicate aerosol may be of size ~2-5 μ m. To investigate the possible origin of these coarse mode aerosol particles, Hysplit 7-day back trajectories for 5 days before and after the date of launch are calculated and shown in Figure S3 (in different colour lines). These Hysplit back trajectories (Stein et al., 2015) indicate the air parcel pathways ending at every 1 km altitude from 1 to 5 km over Gadanki at the time of balloon launch (18 UTC). It can be seen (from Fig. S3) that, the air masses originated from the Indian Ocean passing through the Arabian Sea before reaching the Gadanki location for heights of 1 to 3 km. Therefore, the air masses were of marine origin, and the particles were possibly coarse-mode water-soluble particles (such as sea salt) which can grow hygroscopically due to the availability of moisture over the Ocean surface (Mishra et al., 2010; Ratnam et al., 2018). The rainwater chemical analysis reported by Jain et al. (2019) at Gadanki supports this conclusion as they found dominance of water-soluble ions during the southwest monsoon (June to September). Above 3 km altitude, the air masses are coming from the Saharan desert region (within 7 days) which may bring non-spherical coarse mode dust particles to the launch location (Mishra et al., 2010). Thus, in the case of lower tropospheric coarse mode aerosol (water-soluble aerosol particles), the CI can be >7 at RH<70%.

630 In the altitudes of 6-8.5 km (Fig. 9), CPS has detected no cloud. However, COBALD data shows, that CI values ranging
631 from 3-8 in the altitude range of 6-7 km and 3-12 in the altitude range of 7-8.5 km may indicate the presence of aerosol particles
undetectable

632 by a CPS (i.e., of sizes <2 μ m). RH values indicate sub-saturated conditions throughout this altitude region. However, between

633 ~~7 km~~ and 8.5 km, RH increases and becomes greater than the ice saturation RH values (saturation with ice). Corresponding

634 to this RH change, CI, as well as red channel BSR, is also found to increase. This suggests the growth of small aerosol

635 particles under high humidity conditions until the RH approaches ice saturation where ~~super-cooled~~supercooled liquid droplets are

636 observed (8.6-9 km) in CPS whose features have been discussed already. Since the COBALD CI values are mostly <10 in

this altitude range, the majority of particles detected might be sized up to 1-2 μ m.

~~637—this altitude range, the majority of particles detected might be sized up to 1–2 μm .~~

638 3.3. Statistics on COBALD ~~color~~colour index

639 ~~In order to~~To generalize the optical properties specific to aerosol and cloud, combined data from COBALD and CPS

640 (from multiple launches) has been investigated in detail. The liquid/~~super-cooled~~supercooled cloud, ice cloud and non-spherical particle

641 layer depth are carefully identified with the help of DOP data from CPS (discussed in Section 2). The corresponding data of

642 temperature, relative humidity, BSR, CI, and peak particle number concentration have been picked up for estimating

643 statistics. Further, threshold values of COBALD parameters were tried to identify for the said categories of aerosol and cloud

644 cases. Among 15 balloon soundings, those soundings were considered where CPS detected cloud particles and both blue and

645 red channel data are not missing from COBALD. With these conditions, 8 balloon soundings were identified for estimating

statistics.

646 ~~statistics.~~

647 Table 3 shows the mean (median) values of CI and other parameters corresponding to the ice cloud layers from 7

648 launches. Fig. 11(a) shows the complete statistics of CI in the form of a box plot for the same ice ~~clouds~~cloud layers. Fig. 11(b)

649 shows a histogram of CI from each campaign indicated by different ~~colors~~colours. From Table 3, ice clouds are seen above 9 km with

650 temperatures colder than -20°C . For example, an ice cloud layer was found between 9.3 to 16 km on 30 April 2019 with

651 temperatures in the range of -22 to -79°C , RH close to SRH and mean (median) value of CI is 19.4 (19.3), BSR is 16.4 (8.6) at

652 455 nm, 302 (147) at 940 nm, peak droplet concentration is in the range 10^{-1} to 1#/cc. Similarly, from Table 3, the range of

~~653~~ mean (median) values of BSR is noticed to be from 1.6 (1.4) to 17.2 (17.5) and 12.2 (8.7) to 318 (313) at 455 and 940 nm,
~~654~~ respectively. Therefore, it is difficult to arrive at threshold values of BSR for ice clouds based on Table 3. This may be partly
~~655~~ ~~due to the fact that~~ because BSR depends not only on the particle number concentration but also the size. However, it is interesting
to
~~656~~ note (except for a few cases in Table 3) that BSR data of ice clouds (at both channels) tend to be greater for densely populated
~~657~~ clouds. On the other hand, the difference between mean and median values of CI is not large, thus not much variance in CI
~~658~~ within the ice cloud. It is also clear from Table 3 and Fig. 11(a) that about 90-95 percentile of CI values of ice ~~cloud~~ clouds are
~~659~~ above 15 and below 25 with mean/median values in the range 18-20. The same is also seen in the histogram of CI shown
~~660~~ (Fig. 11b) in different ~~colors~~ colours for different sounding dates where a greater number of points in a sounding are lying close to
~~661~~ 20. Therefore, it may be concluded that the mean value of CI of ice clouds would be between 18 and 20.

~~662~~ The data from 8 soundings are also analysed for CI (and other parameters) of liquid clouds. However, it is noted
~~663~~ that liquid clouds were not observed as often as ice ~~cloud~~ clouds in the balloon data. In the second campaign (8 July 2017) a liquid
~~664~~ cloud layer was observed at ~~altitude~~ altitudes from 4.7 to 4.86 km (160 m) with $RH > SRH$, temperatures in the range of -0.4 to -
1.65°C.

~~665~~ The mean value of CI corresponding to this liquid cloud layer is very high around 50. Similarly, another liquid cloud layer
~~666~~ was observed in the fourth campaign (01 Nov. 2018) in the altitude range of 2-2.3 km (300 m). The corresponding CI values
~~667~~ are high and above 100 (up to 200). ~~Couple~~ A couple of thin ~~super-cooled~~ supercooled liquid cloud layers were also identified on
the same

~~668~~ sounding between 6.1-6.17 km (7 m) and 6.6-6.8 km (200 m). The corresponding CI values are found with mean (median)
~~669~~ values of 19.5 (19.4) and 32.6 (32.8), respectively. Apart from this, a strong boundary layer (liquid) cloud layer was
~~670~~ observed on 23 Mar. 2019 (fifth campaign) between 0.9 and 1.2 km (300 m). The corresponding CI of liquid cloud was
~~671~~ found to be high with mean, and median values of 60-80. From the above discussion (including the liquid cloud cases not
~~672~~ discussed above), it is noticed that the CI for liquid clouds is high. The difference in CI values of liquid clouds can be

attributed to the thickness of the cloud, and the density and droplet size of liquid clouds.

~~673~~ ~~attributed to the thickness of cloud, density and droplet size of liquid clouds.~~

~~674~~ Non-spherical large dust aerosol particles were identified by DOP values from CPS in the lower troposphere where
~~675~~ RH is far less than 100%. Statistics on COBLAD CI (and other parameters) for these non-spherical particle cases are

~~676~~ presented in Table 4 using the data from 8 soundings. For example, a non-spherical particle layer was found between 0.5 and ~~677~~ 2.5 km altitudes on 06 June 2017 with temperatures in the range of 15.5 to 27.6⁰C and relative humidity is dry from 63.5 to

81.3%. The mean (median) value of CI corresponding to this non-spherical particle layer is 12.3 (12.5), BSR is 1.45 (1.4) at 455 nm, 6.5(6) at 940 nm and peak particle concentration is between 10^{-3} and 10^{-1} #/cm³. The peak particle concentration of all non-spherical layers is found to be in the same range and hence not shown. From Table 4, it can be noticed that the non-spherical particle (aerosol) layer is found from the near-surface to the 5 km altitude depending on the month or season. During the monsoon season (font in blue ~~color~~colour in Table 4), non-spherical particle layers were observed mostly from the near-surface (500m) to 2.5 km whereas during pre-monsoon (font in wine red ~~color~~colour) it is found from 0.5 up to 5 km. The reason for the difference in layer thickness among seasons may be attributed to the mixing within the lower troposphere, long-range transport and local sources. Since these layers are confined mostly to the lower troposphere, the temperatures are in the range of 27 to below 0°C. From the above statistics (pre-monsoon and monsoon cases) it may be stated that the mean/median value of CI for the non-spherical particle layer is distributed between 11 and 15, irrespective of environmental humidity and season.

BSR values for the non-spherical layer are between 1.4 and 3.5 at 455 nm, whereas little spread in the red channel.

~~BSR values for non-spherical layer are between 1.4 and 3.5 at 455 nm, whereas little spread in red channel.~~

3.4. Illustration of the aerosol-cloud relationship

~~In this section, an attempt is made to demonstrate the method to identify the relationship, if any, between aerosol and cloud properties observed using balloon observations of the BACIS campaigns. In the present analysis we have restricted ourselves to only liquid or low level clouds as aerosol interactions in these cloud categories are well established (Bruce A. Albrecht, 1989; Twomey, 1977).~~

In this section, an attempt is made to demonstrate the method to identify the relationship, if any, between aerosol and cloud properties observed using balloon observations of the BACIS campaigns. In the present analysis, we have restricted ourselves to only liquid or low-level clouds as aerosol interactions in these cloud categories are well established (Bruce A. Albrecht, 1989; Twomey, 1977).

The scheme (discussed in sec. 2) is applied to the 15 balloon soundings of the BACIS campaigns and 6 launches have been observed with low-level cloud and aerosol layers. Further, a scatter plot between logarithm values of the median cloud particle count of the cloud layer and logarithm of median values of aerosol (blue) ~~back scatter~~backscatter below cloud base (for 300, 400 and 500m) is plotted in Fig. 12. A linear fit (line) of log-log values is also shown separately for all depths. It is noticed

698— for depths 100 and 200m below the cloud base relationship between aerosol, and the cloud cannot be discussed due to a lack of
data points

699— of aerosol backscatter ratio from individual campaigns. This could be the result of the elimination of the high value of COBALD

700— particle ~~back-scatter~~backscatter (>3.15) observed in this region (100 and 200m below cloud base). In the cloud boundaries of about
100

701— and 200m below the cloud base, an intermediate region exists where aerosol transformation to cloud particle/growth takes place.

702— Hence it is tricky to have the aerosol observation in this region. On the other hand, with similar elimination criteria (Section 2),

703 aerosol backscatter could be obtained (from all 5 campaigns) for depths 300m onwards (up to 500m) from ~~cloud base.~~ the cloud
base. A good positive relationship is found between aerosol backscatter and cloud particle count with a statistically significant Pearson
correlation coefficient of about 0.9 and slope (ACI index) of 0.77 and 0.86 when the aerosol is considered from 300 and 400m below the cloud
base, respectively. For a depth of 500m from the cloud base, the slope has decreased to 0.67 (correlation coefficient is also not significant with
p-value >0.05) indicating aerosol influence weakens if the region below 400m from the cloud base is considered. Therefore, it may be better
to consider aerosols up to a depth of 400m (below the cloud base) for understanding their influence on cloud properties. It is also emphasized
that the slope (ACI index) value obtained in this analysis at all depths is well within the theoretical range of 0 to 1. However, with a greater
number of balloon soundings, it might be possible to have statistically significant aerosol data after constraining similar
background/meteorological conditions to delineate their possible effects. Data obtained on 04 February 2020 was not considered in the analysis
due to the high values of COBALD. The individual uncertainties in BSRb and Nc were assumed to be 5% and the combined uncertainty in the
ACI index is estimated as discussed in Sec. 2.4.7 (equation.7). It is found that the combined uncertainty in the estimated ACI index is found
from 0.01 to 0.23 and 0.08 to 0.13, respectively for particle backscatter data from 300 and 400m below cloud base.

704 good positive relationship is found between aerosol backscatter and cloud particle count with a statistically significant
705 Pearson correlation coefficient of about 0.9 and slope (ACI index) of 0.77 and 0.86 when aerosol is considered from 300 and
706 400m below cloud base, respectively. For depth of 500m from cloud base, the slope has decreased to 0.67 (correlation
707 coefficient is also not significant with p value >0.05) indicates aerosol influence weakens if region below 400m from cloud
708 base is considered. Therefore, it may be better to consider aerosol up to a depth of 400m (below the cloud base) for
709 understanding their influence on cloud properties. It is also emphasized that the slope (ACI index) value obtained in this
710 analysis at all depths are well within the theoretical range of 0 to 1. However, with a greater number of balloon soundings it
711 might be possible to have statistically significant aerosol data after constraining the similar background/meteorological
712 conditions to delineate their possible effects. Sounding from (with a low level cloud layer) 04 February 2020 is ignored due
713 to high values of COBALD return signal possibly due to an optical interference. The individual uncertainties in BSRb and
714 Nc were assumed to be 5% and the combined uncertainty in ACI index is estimated as discussed in Sec. 2.4.7 (equation.7). It
715 is found that the combined uncertainty in estimated ACI index is found from 0.01 to 0.23 and 0.08 to 0.13, respectively for
716 particle backscatter data from 300 and 400m below cloud base.

717 **4. Summary**

718 — The BACIS (Balloon-borne Aerosol Cloud Interaction Studies) field campaigns have been conceptualized and
719 — successfully conducted using multiple instruments from Gadanki (13.45° N; 79.2° E), a location in Southern peninsular
720 — India. Meteorological balloon ~~payload~~payloads with a combination of lightweight and specialized sondes such as COBALD and
CPS
721 — have been launched for the first time ~~prior to~~before a CALIPSO satellite overpass (close by Gadanki). Ground-based Lidars
722 — (MPL/Ceilometer/Mie lidar), and Radars (MST Radar/LAWP) were also operated during the campaign period. So far 15 balloon
723 — soundings have been conducted as part of the BACIS campaigns.

724 — During the first two (pilot) campaigns, all essential ground-based and space-borne instruments were made available.
725 — ~~Consistency in balloon~~ Balloon-borne in-situ measurements (CPS and COBALD) ~~is~~are assessed using the data from ground/~~space~~
~~borne~~
726 — ~~spaceborne~~ remote sensing instruments (CALIPSO, MPL and a Mie lidar) from two pilot campaigns (early hours of 6 June and 8
July
727 — 2017). The comparison shows ~~a good~~reasonable agreement within in-situ measurements as well as between ground-based/space-
borne

728— and in-situ measurements. It is observed that the in-situ balloon soundings using a combination of specialized (COBALD and
729— CPS) sondes adds to the cloud and aerosol information than can be obtained from an individual ground/~~space~~
~~spaceborne~~ instrument.

730— instrument.

731— ~~In order to~~ To discriminate aerosol from clouds in a profile, combined observations of COBALD and CPS from a
732— campaign held on 27 June 2019 were inferred in detail. Using CPS data, liquid, ~~super-cooled,~~ supercooled, and ice clouds were
identified.

733— COBALD data of BSR corresponding to the ice clouds was found to be 1-10 (at blue channel) and CI of 10 to 20. In addition

734— to cloud features, CPS has also detected cloud particle layers at low altitudes (under dry conditions). These layers may be

735— regarded as non-spherical (coarse mode) aerosol particle layers as ice clouds (with non-spherical cloud particles) cannot exist at lower

heights. An attempt is also made to infer the size of cloud particles using the CPS data of intensity of scattered light (I55) and the COBALD

colour index. Based on CPS scattered light, the liquid droplet size (for the above case) is estimated to be 2-14 μm , and for ice particles, it is a

combination of particles with 80-140 μm and 2-14 μm . The estimates of ice particle sizes using CI data from COBALD supported the size

interpretations of ice particles by CPS.

736— ~~at lower heights. An attempt is also made to infer the size of cloud particle using the CPS data of intensity of scattered light~~

737— ~~(I55) and the COBALD color index. Based on CPS scattered light, the liquid droplet size (for the above case) is estimated to~~

738— ~~be 2-14 μm , and for ice particles it is combination of particles with 80-140 μm and 2-14 μm . The estimates of ice particle~~

739— ~~sizes using CI data from COBALD supported the size interpretations of ice particles by CPS.~~

740— Further, combined observations from COBALD and CPS (BSR, CI, and peak particle number concentration data

741— based on information on the cloud phase) are analyzed from multiple (eight) balloon soundings from BACIS Campaigns.

742— From these statistics, it is found that the mean value of CI of ice cloud is found between 18 and 20. BSR (at both

743— wavelengths) have a wide range of values hence threshold values for ice clouds could not be arrived at. However, in some

744— cases, ~~we noticed,~~ BSR increased with ice clouds of more droplet number concentration. In the case of non-spherical particle

745— (aerosol) layers (in the lower troposphere), the mean values of CI and BSR (at 455 nm) are found to be between 11 to 15 and

746— 1.4 to 3.5, respectively. These non-spherical particle layers may correspond to coarse mode (dust) aerosols as discussed.

747 ————— The relationship between aerosol and cloud in low-level (liquid) ~~cloud~~clouds is illustrated using balloon data from BACIS
748 — campaigns. CPS cloud particle count and COBALD particle backscatter at the blue channel were considered as cloud and
749 — aerosol proxies, respectively. A scheme is developed to carefully identify the cloud layers from CPS data and particle
750 — (aerosol) backscatter below the cloud from COBALD data (in a profile). However, the relationships were analyzed
751 — separately using particle backscatter data from 100 to 500m below the base height for the first cloud layer. The results show;
752 — a statistically significant correlation of 0.9 and a slope (Aerosol-Cloud Interaction index, ACI) of 0.7 (0.86) obtained between

753 _particle backscatter from 300m (500m) below the cloud base and the corresponding cloud particle count. ~~The ACI index~~The
ACI index value obtained is well within the theoretical limits of 0 to 1 indicative of the aerosol activation process of the cloud. The uncertainty
in the estimated value of the ACI index is 0.01 to 0.23 and 0.08 to 0.13, respectively for backscatter data from 300 and 400m below the cloud
base.

~~754 value obtained are well within the theoretical limits of 0 to 1 indicative of aerosol activation process of cloud. The~~
~~755 uncertainty in the estimated value of ACI index is 0.01 to 0.23 and 0.08 to 0.13, respectively for back scatter data from 300~~
~~756 and 400m below the cloud base.~~

757 _____Statistical estimates/threshold value of CI, BSR for cloud (liquid/super-cooled/ice) and non-spherical particles
758 _attempted here will greatly help to separate a COBALD profile ~~with respect to~~for aerosol and cloud. However, immediate
759 _efforts are needed to understand the portion of the COBALD profile with no cloud detection from CPS. This portion of
760 the COBALD profile may correspond to either aerosol with fine mode particles and/or a thin cloud not detectable by a CPS. On
761 _the other hand, estimates of size discussed here (from CPS, COBALD) are purely based on Mie theory and laboratory data.
762 _However, with assumptions of the log-normal distribution of particles and measurements from COBALD (BSR, CI), the
theoretical
763 _estimate of the particle size distribution of aerosol/cloud is possible. It makes sense to cross-check rough estimates of size from a
764 _CPS with COBALD size distributions rather than using CI variations. It is also planned to add a size distribution
765 _measurement to the balloon payload for cross-~~in~~ verification and validation. Apart from this, in some of the cases, we have
766 _noticed COBALD return signal saturated for liquid/~~super-cooled~~supercooled cloud in the presence of a thick liquid cloud. Hence
the
767 _information from a greater number of future launches will help to conclude the statistical figures/threshold values for liquid
768 _clouds as well as other cases of clouds, to discriminate the aerosol/cloud in a profile and to better quantify the aerosol-cloud
769 _relationship. Further to this, attempts will be made to quantify aerosol-cloud interactions (with the multi-instrument data),
particularly the role of vertical wind and turbulence on the aerosol-cloud interactions, and ice cloud interactions, among others. In a nutshell,
the results presented in the study indeed demonstrate the potential of the observational approach/method, to understand the aerosol-cloud
process.

~~770 particularly the role of vertical wind and turbulence on the aerosol cloud interactions, ice cloud interactions, among others.~~

~~771 In a nutshell, the results presented in the study indeed demonstrate the potential of observational approach/method, paves the~~
~~772 way for future campaigns to understand aerosol cloud process.~~

Code/Data Availability

774 Data analyzed in the study is made available on Zenodo (~~10.5281/zenodo.5749293~~[10.5281/zenodo.5749293](https://zenodo.org/record/105281)). Data

will also be shared with the interested users under the collaboration.

~~775 with the interested users upon request and under collaboration.~~

Author Contribution

~~777~~ RKV is responsible for Conceptualization, Conducting ~~experiment~~experiments, Formal analysis, Visualization, Investigation,

~~778~~ Writing-original draft preparation; VRM is responsible for Supervision, ~~helped~~helping in Visualization, Writing-review and editing.

~~779~~ FM, HR and FGW are responsible for Writing-review and editing; MBL, RRM, and RN helped in Visualization, Writing-review ~~780~~ and editing; RN, ARST, HKA, and RBS helped in conducting the experiment, Writing-review and editing;

~~781~~ Competing interest

The authors declare that they have no conflict of interest.~~783~~

~~782~~ Acknowledgements

~~784~~ ~~Authors~~The authors would like to thank the Director, NARL for supporting ~~to conduct of~~ conducting the field campaigns from NARL, Gadanki. ~~785~~ Special thanks to the RADG and ASDG group members of NARL for their ~~co-operation~~cooperation in the operation of Indian MST ~~786~~ Radar, LAWP and Mie Lidar, respectively, during the launch period. We also would like to express our thanks to the staff ~~787~~ members of ARTG, the balloon launch facility of NARL for extending their kind support for smoothly conducting balloon ~~788~~ launches and recovery. The CALIPSO science team is credited for providing the CALIOP data analysed in the study freely ~~789~~ available at on their webpage (<https://www.calipso.larc.nasa.gov>). We are also thankful to the Hysplit team for facilitating ~~to~~ ~~790~~ ~~run~~the running of the HYSPLIT model on their server to simulate the air parcel back trajectories as per the requirement.

~~791~~

~~792~~

References

~~793~~ Abbott, T. H. and Cronin, T. W.: Through Increases in Humidity, *Science* (80 .), 85(January), 83–85, 2021.

~~794~~ Brabec, M., Wienhold, F. G., Wüest, M., Krieger, U. and Peter, T.: A novel radiosonde payload to study upper tropospheric / ~~795~~ lower stratospheric aerosol and clouds, 2008.

~~796~~ Brabec, M., Wienhold, F. G., Luo, B. P., VÄmel, H., Immler, F., Steiner, P., Hausammann, E., Weers, U. and Peter, T.: ~~797~~ Particle backscatter and relative humidity measured across cirrus clouds and comparison with microphysical cirrus ~~798~~ modelling, *Atmos. Chem. Phys.*, 12(19), 9135–9148, doi:10.5194/acp-12-9135-2012, 2012.

~~799~~ BRUCE A. ALBRECHT: Aerosols, Cloud Microphysics, and Fractional Cloudiness, *Science* (80 .), 245(4247), 24–29, 800 1989.

~~801~~ Brunamonti, S., Jorge, T., Oelsner, P., Hanumanthu, S., Singh, B. B., Ravi Kumar, K., Sonbawne, S., Meier, S., Singh, D., ~~802~~ Wienhold, F. G., Ping Luo, B., Boettcher, M., Poltera, Y., Jauhiainen, H., Kayastha, R., Karmacharya, J., Dirksen, R., Naja, ~~803~~ M., Rex, M., Fadnavis, S. and Peter, T.: Balloon-borne measurements of temperature, water vapor, ozone and aerosol ~~804~~ backscatter on the southern slopes of the Himalayas during StratoClim 2016–2017, *Atmos. Chem. Phys.*, 18(21), 15937–805

~~15957, doi:10.5194/aep-18-15937-2018, 2018.~~

~~806 — Brunamonti, S., Martucci, G., Romanens, G., Poltera, Y., Wienhold, F., Haeferle, A. and Navas-Guzmán, F.: Validation of 807
aerosol backscatter profiles from Raman lidar and ceilometer using balloon-borne measurements, Atmos. Chem. Phys.~~

808 Discuss., (May), 1–31, doi:10.5194/acp-2020-294, 2020.

809 Cherian, T., Kumar, Y. B., Reddy, B. S., Optics, G., Limited, A., Nr, R. S. and Road, N.: LIDAR for Atmospheric
Measurement and Probing, , 5(84), 5114–5124, 2014.

811 Cirisan, A., Luo, B. P., Engel, I., Wienhold, F. G., Sprenger, M., Krieger, U. K., Weers, U., Romanens, G., Levrat, G.,
812 Jeannet, P., Ruffieux, D., Philipona, R., Calpini, B., Spichtinger, P. and Peter, T.: Balloon-borne match measurements of
813 midlatitude cirrus clouds, *Atmos. Chem. Phys.*, 14(14), 7341–7365, doi:10.5194/acp-14-7341-2014, 2014.

814 COAKLEY, J. A., BERNSTEIN, R. L. and DURKEE, P. A.: Effect of Ship Stack Effluents on Cloud Reflectivity, *Science* 815
(80 .), 237(4818), 1020 LP–1022, doi:10.1126/science.237.4818.1020, 1987.

816 Corrigan, C. E., Roberts, G. C., Ramana, M. V., Kim, D. and Ramanathan, V.: Capturing vertical profiles of aerosols and
817 black carbon over the Indian Ocean using autonomous unmanned aerial vehicles, *Atmos. Chem. Phys.*, 8(3), 737–747, 818
doi:10.5194/acp-8-737-2008, 2008.

819 Costantino, L. and Bréon, F. M.: Analysis of aerosol cloud interaction from multi-sensor satellite observations, *Geophys.*
820 *Res. Lett.*, 37(11), 1–5, doi:10.1029/2009GL041828, 2010.

821 Fan, J., Wang, Y., Rosenfeld, D. and Liu, X.: Review of aerosol cloud interactions: Mechanisms, significance, and
822 challenges, *J. Atmos. Sci.*, 73(11), 4221–4252, doi:10.1175/JAS-D-16-0037.1, 2016.

823 Fan, J., Rosenfeld, D., Zhang, Y., Giangrande, S. E., Li, Z., Machado, L. A. T., Martin, S. T., Yang, Y., Wang, J., Artaxo, P.,
824 Barbosa, H. M. J., Braga, R. C., Comstock, J. M., Feng, Z., Gao, W., Gomes, H. B., Mei, F., Pöhlker, C., Pöhlker, M. L.,
825 Pöschl, U. and de Souza, R. A. F.: Substantial convection and precipitation enhancements by ultrafine aerosol particles,
826 *Science* (80 .), 359(6374), 411–418, doi:10.1126/science.aan8461, 2018.

827 Feingold, G., Eberhard, W. L., Veron, D. E. and Previdi, M.: First measurements of the Twomey indirect effect using
828 ground-based remote sensors, *Geophys. Res. Lett.*, 30(6), 19–22, doi:10.1029/2002GL016633, 2003.

829 Feingold, G., Furrer, R., Pilewskie, P., Remer, L. A., Min, Q. and Jonsson, H.: Aerosol indirect effect studies at Southern
830 Great Plains during the May 2003 Intensive Operations Period, *J. Geophys. Res. Atmos.*, 111(5), 1–13, 831
doi:10.1029/2004JD005648, 2006.

832 Fujiwara, M., Shiotani, M., Hasebe, F., Vömel, H., Oltmans, S. J., Ruppert, P. W., Horinouchi, T. and Tsuda, T.:
Performance of the Meteolabor “Snow White” chilled-mirror hygrometer in the tropical troposphere: Comparisons with the
834 Vaisala RS80 A/H Humicap sensors, *J. Atmos. Ocean. Technol.*, 20(11), 1534–1542, doi:10.1175/1520-835
0426(2003)020<1534:POTMSW>2.0.CO;2, 2003.

836 Fujiwara, M., Sugidachi, T., Arai, T., Shimizu, K., Hayashi, M., Noma, Y., Kawagita, H., Sagara, K., Nakagawa, T.,
837 Okumura, S., Inai, Y., Shibata, T., Iwasaki, S. and Shimizu, A.: Development of a cloud-particle sensor for radiosonde
838 sounding, *Atmos. Meas. Tech.*, 9(12), 5911–5931, doi:10.5194/amt-9-5911-2016, 2016.

839 Grosvenor, D. P., Sourdeval, O., Zuidema, P., Ackerman, A., Alexandrov, M. D., Bennartz, R., Boers, R., Cairns, B., Chiu, 840
J. C., Christensen, M., Deneke, H., Diamond, M., Feingold, G., Fridlind, A., Hünerbein, A., Knist, C., Kollias, P., Marshak, 841 A.,
McCoy, D., Merk, D., Painemal, D., Rausch, J., Rosenfeld, D., Ruschke, H., Seifert, P., Sinclair, K., Stier, P.,

842 van Dierenhoven, B., Wendisch, M., Werner, F., Wood, R., Zhang, Z. and Quaas, J.: Remote Sensing of Droplet Number 843
Concentration in Warm Clouds: A Review of the Current State of Knowledge and Perspectives, *Rev. Geophys.*, 56(2), 409–844 453,
doi:10.1029/2017RG000593, 2018.

845 Gupta, G., Ratnam, M. V., Madhavan, B. L., Prasad, P. and Narayanamurthy, C. S.: Vertical and spatial distribution of 846
elevated aerosol layers obtained using long term ground based and space borne lidar observations, *Atmos. Environ.*, 847
246(December 2020), 118172, doi:10.1016/j.atmosenv.2020.118172, 2021.

848 Haywood, J. and Boucher, O.: Estimates of the direct and indirect radiative forcing due to tropospheric aerosols: A review, 849
Rev. Geophys., 38(4), 513–543, doi:10.1029/1999RG000078, 2000.

850 IPCC: Climate Change 2013: [online] Available from: https://www.ipcc.ch/pdf/assessment-report/ar5/wg1/WGIAR5_SPM_brochure_en.pdf, 2013.

852 Jain, C. D., Madhavan, B. L. and Ratnam, M. V.: Source apportionment of rainwater chemical composition to investigate the 853
transport of lower atmospheric pollutants to the UTLS region, *Environ. Pollut.*, 248, 166–174, 854
doi:10.1016/j.envpol.2019.02.007, 2019.

855 Jose, S., Nair, V. S. and Babu, S. S.: Anthropogenic emissions from South Asia reverses the aerosol indirect effect over the 856
northern Indian Ocean, *Sci. Rep.*, 10(1), 1–8, doi:10.1038/s41598-020-74897-x, 2020.

857 Kobayashi, E., Hoshino, S., Iwabuchi, M., Sugidachi, T., Shimizu, K. and Fujiwara, M.: Comparison of the GRUAN data 858
products for Meisei RS-11G and Vaisala RS92-SGP radiosondes at Tateno (36.06°N, 140.13°E), Japan, *Atmos. Meas. Tech.*, 859
12(6), 3039–3065, doi:10.5194/amt-12-3039-2019, 2019.

860 Koren, I., Remer, L. A., Altaratz, O., Martins, J. V. and Davidi, A.: Aerosol induced changes of convective cloud anvils 861
produce strong climate warming, *Atmos. Chem. Phys.*, 10(10), 5001–5010, doi:10.5194/acp-10-5001-2010, 2010.

862 Kulkarni, J. R., Maheskumar, R. S., Morwal, S. B., Padma Kumari, B., Konwar, M., Deshpande, C. G., Joshi, R. R.,
863 Bhalwankar, R. V., Pandithurai, G., Safai, P. D., Narkhedkar, S. G., Dani, K. K., Nath, A., Nair, S., Sapre, V. V., Puranik, P. 864
V., Kandalgaonkar, S. S., Mujumdar, V. R., Khaladkar, R. M., Vijayakumar, R., Prabha, T. V. and Goswami, B. N.: The 865
cloud aerosol interaction and precipitation enhancement experiment (CAIPEEX): Overview and preliminary results, *Curr. Sci.*,
866 102(3), 413–425, 2012.

867 L’Ecuyer, T. S.: Touring the atmosphere aboard the A-Train (vol 63, pg 36, 2010), *Phys. Today*, 64(8), 10, 2011.

868 Lohmann, U.: Aerosol effects on clouds and climate, *Space Sci. Rev.*, 125(1–4), 129–137, doi:10.1007/s11214-006-9051-8,
869 2006.

870 Lohmann, U. and Feichter, J.: Global indirect aerosol effects: a review, *Atmos. Chem. Phys. Discuss.*, 4(6), 7561–7614,
871 doi:10.5194/acpd-4-7561-2004, 2004.

872 McComiskey, A. and Feingold, G.: The scale problem in quantifying aerosol indirect effects, *Atmos. Chem. Phys.*, 12(2),
873 1031–1049, doi:10.5194/acp-12-1031-2012, 2012.

874 McComiskey, A., Feingold, G., Frisch, A. S., Turner, D. D., Miller, M. A., Chiu, J. C., Min, Q. and Ogren, J. A.: An
875 assessment of aerosol cloud interactions in marine stratus clouds based on surface remote sensing, *J. Geophys. Res. Atmos.*,

876—114(9), 1–15, doi:10.1029/2008JD011006, 2009.

877 Mishra, M. K., Rajeev, K., Thampi, B. V., Parameswaran, K. and Nair, A. K. M.: Micro pulse lidar observations of mineral 878
dust layer in the lower troposphere over the southwest coast of Peninsular India during the Asian summer monsoon season, 879 J.
Atmos. Solar Terrestrial Phys., 72(17), 1251–1259, doi:10.1016/j.jastp.2010.08.012, 2010.

880 Murphy, D. M. and Koop, T.: Review of the vapour pressures of ice and supercooled water for atmospheric applications, Q. 881
J. R. Meteorol. Soc., 131(608), 1539–1565, doi:10.1256/qj.04.94, 2005.

882 Narendra Reddy, N., Venkat Ratnam, M., Basha, G. and Ravikiran, V.: Cloud vertical structure over a tropical station 883
obtained using long term high resolution Radiosonde measurements, Atmos. Chem. Phys. Discuss., 1–49, doi:10.5194/acp 884
2018 194, 2018.

885 Pandit, A. K., Gadhavi, H., Ratnam, M. V., Jayaraman, A., Raghunath, K. and Rao, S. V. B.: Characteristics of cirrus clouds 886
and tropical tropopause layer: Seasonal variation and long term trends, J. Atmos. Solar Terrestrial Phys., 121(PB), 248–256, 887
doi:10.1016/j.jastp.2014.07.008, 2014.

888 Pandit, A. K., Gadhavi, H. S., Ratnam, M. V., Raghunath, K., Rao, S. V. B. and Jayaraman, A.: Long term trend analysis 889
and climatology of tropical cirrus clouds using 16 years of lidar data set over Southern India, Atmos. Chem. Phys., 15(24), 890
13833–13848, doi:10.5194/acp 15 13833 2015, 2015.

891 Pandithurai, G., Takamura, T., Yamaguchi, J., Miyagi, K., Takano, T., Ishizaka, Y., Dipu, S. and Shimizu, A.: Aerosol effect 892
on cloud droplet size as monitored from surface based remote sensing over East China Sea region, Geophys. Res. Lett.,
893 36(13), 1–5, doi:10.1029/2009GL038451, 2009.

894 Prasad, P., Raman, M. R., Ratnam, M. V., Ravikiran, V., Madhavan, B. L. and Bhaskara, S. V.: Nocturnal , seasonal and 895
intra annual variability of tropospheric aerosols observed using ground based and space borne lidars over a tropical location 896
of India, Atmos. Environ., 213(May), 185–198, doi:10.1016/j.atmosenv.2019.06.008, 2019.

897 Radke, L. F., Coakley, J. A. and King, M. D.: Direct and remote sensing observations of the effects of ships on clouds, 898
Science (80 .), 246(4934), 1146–1149, doi:10.1126/science.246.4934.1146, 1989.

899 Rao, P. B., Jain, A. R., Kishore, P., Balamuralidhar, P., Damle, S. H. and Viswanathan, G.: Indian MST radar 1. System 900
description and sample vector wind measurements in ST mode, Radio Sci., 30(4), 1125–1138, doi:10.1029/95RS00787,
901 1995.

902 Ratnam, M. V., Prasad, P., Raman, M. R., Ravikiran, V., Bhaskara, S. V., Murthy, B. V. K. and Jayaraman, A.: Role of 903
dynamics on the formation and maintenance of the elevated aerosol layer during monsoon season over south east peninsular 904
India, , 188(June), 43–49, doi:10.1016/j.atmosenv.2018.06.023, 2018.

905 Redemann, J., Wood, R., Zuidema, P., Doherty, S., Luna, B., LeBlanc, S., Diamond, M., Shinozuka, Y., Chang, I., Ueyama, 906
R., Pfister, L., Ryoo, J., Dobracki, A., da Silva, A., Longo, K., Kacenelenbogen, M., Flynn, C., Pistone, K., Knox, N., Piketh, 907 S.,
Haywood, J., Formenti, P., Mallet, M., Stier, P., Ackerman, A., Bauer, S., Fridlind, A., Carmichael, G., Saide, P., 908 Ferrada,
G., Howell, S., Freitag, S., Cairns, B., Holben, B., Knobelspiesse, K., Tanelli, S., L'Ecuyer, T., Dzambo, A., Sy, O., 909 McFarquhar,
G., Poellot, M., Gupta, S., O'Brien, J., Nenes, A., Kacarab, M., Wong, J., Small Griswold, J., Thornhill, K.,

910 Noone, D., Podolske, J., Schmidt, K. S., Pilewskie, P., Chen, H., Cochrane, S., Sedlacek, A., Lang, T., Stith, E., Segal-
911 Rozenhaimer, M., Ferrare, R., Burton, S., Hostetler, C., Diner, D., Platnick, S., Myers, J., Meyer, K., Spangenberg, D.,
912 Maring, H. and Gao, L.: An overview of the ORACLES (ObseRvations of Aerosols above CLouds and their intEractionS) 913
project: aerosol cloud radiation interactions in the Southeast Atlantic basin, *Atmos. Chem. Phys.*, 1–82, doi:10.5194/acp-914 2020-
449, 2020.

915 Rosen, J. M. and Kjome, N. T.: Backscattersonde: a new instrument for atmospheric aerosol research, *Appl. Opt.*, 30(12), 916
1552, doi:10.1364/ao.30.001552, 1991.

917 Rosenfeld, D., Lohmann, U., Raga, G. B., O'Dowd, C. D., Kulmala, M., Fuzzi, S., Reissell, A. and Andreae, M. O.: Flood or
918 drought: How do aerosols affect precipitation?, *Science* (80-.), 321(5894), 1309–1313, doi:10.1126/science.1160606, 2008. 919

Rosenfeld, D., Sherwood, S., Wood, R. and Donner, L.: Climate Effects of Aerosol-Cloud Interactions, *Science* (80-.), 920
343(6169), 379 LP–380, doi:10.1126/science.1247490, 2014a.

921 Rosenfeld, D., Andreae, M. O., Asmi, A., Chin, M., Leeuw, G., Donovan, D. P., Kahn, R., Kinne, S., Kivekäs, N., Kulmala, 922
M., Lau, W., Schmidt, K. S., Suni, T., Wagner, T., Wild, M. and Quaas, J.: Reviews of Geophysics, -, 1–59, 923
doi:10.1002/2013RG000441.Received, 2014b.

924 Sarna, K. and Russchenberg, H. W. J.: Ground-based remote-sensing scheme for monitoring aerosol cloud interactions,
925 *Atmos. Meas. Tech.*, 9(3), 1039–1050, doi:10.5194/amt-9-1039-2016, 2016.

926 Sarna, K. and Russchenberg, H. W. J.: Monitoring aerosol cloud interactions at the CESAR Observatory in the Netherlands, 927
Atmos. Meas. Tech., 10(5), 1987–1997, doi:10.5194/amt-10-1987-2017, 2017.

928 Sathiyamoorthy, V., Mahesh, C., Gopalan, K., Prakash, S., Shukla, B. P. and Mathur, A. K.: Characteristics of low clouds 929
over the Arabian Sea, , 118(December), 489–503, doi:10.1002/2013JD020553, 2013.

930 Schmidt, J., Ansmann, A., Bühl, J., Baars, H., Wandinger, U., Müller, D. and Malinka, A. V.: Dual-FOV raman and Doppler
931 lidar studies of aerosol cloud interactions: Simultaneous profiling of aerosols, warm cloud properties, and vertical wind, *J.* 932
Geophys. Res., 119(9), 5512–5527, doi:10.1002/2013JD020424, 2014.

933 Schmidt, J., Ansmann, A., Bühl, J. and Wandinger, U.: Strong aerosol cloud interaction in altocumulus during updraft 934
periods: Lidar observations over central Europe, *Atmos. Chem. Phys.*, 15(18), 10687–10700, doi:10.5194/acp-15-10687-935
2015, 2015.

936 Seinfeld, J. H., Bretherton, C., Carslaw, K. S., Coe, H., DeMott, P. J., Dunlea, E. J., Feingold, G., Ghan, S., Guenther, A. B., 937
Kahn, R., Kraucunas, I., Kreidenweis, S. M., Molina, M. J., Nenes, A., Penner, J. E., Prather, K. A., Ramanathan, V., 938
Ramaswamy, V., Rasch, P. J., Ravishankara, A. R., Rosenfeld, D., Stephens, G. and Wood, R.: Improving our fundamental 939
understanding of the role of aerosol cloud interactions in the climate system, *Proc. Natl. Acad. Sci. U. S. A.*, 113(21), 5781–940
5790, doi:10.1073/pnas.1514043113, 2016.

941 Sena, E. T., McComiskey, A. and Feingold, G.: A long-term study of aerosol cloud interactions and their radiative effect at 942
the Southern Great Plains using ground-based measurements, *Atmos. Chem. Phys.*, 16(17), 11301–11318, doi:10.5194/acp-943 16-
11301-2016, 2016.

944—Small, J. D., Chuang, P. Y., Feingold, G. and Jiang, H.: Can aerosol decrease cloud lifetime?, *Geophys. Res. Lett.*, 36(16), 945
1–5, doi:10.1029/2009GL038888, 2009.

946 Srinivasulu, P., Yasodha, P., Kamaraj, P., Rao, T. N., Jayaraman, A., Reddy, S. N. and Satyanarayana, S.: 1280 MHz active 947
array radar wind profiler for lower atmosphere: System description and data validation, *J. Atmos. Ocean. Technol.*, 29(10), 948
1455–1470, doi:10.1175/JTECH-D-12-00030.1, 2012.

949 Stein, A. F., Draxler, R. R., Rolph, G. D., Stunder, B. J. B., Cohen, M. D. and Ngan, F.: NOAA's hysplit atmospheric transport
950 and dispersion modeling system, *Bull. Am. Meteorol. Soc.*, 96(12), 2059–2077, doi:10.1175/BAMS-D-14-00110.1, 2015.

951 Twomey, S.: The Influence of Pollution on the Shortwave Albedo of Clouds, *J. Atmos. Sci.*, 34(7), 1149–1152, 952
doi:10.1175/1520-0469(1977)034<1149:TIOPOT>2.0.CO;2, 1977.

953 Vernier, J., Fairlie, T. D., Natarajan, M., Wienhold, F. G., Bian, J., Martinsson, B. G., Crumeyrolle, S., Thomason, L. W. and
954 Bedka, K. M.: *Journal of Geophysical Research : Atmospheres*, doi:10.1002/2014JD022372, Received, 2015.

955 Vernier, J. P., Fairlie, T. D., Deshler, T., Venkat Ratnam, M., Gadhave, H., Kumar, B. S., Natarajan, M., Pandit, A. K., Akhil 956
Raj, S. T., Hemant Kumar, A., Jayaraman, A., Singh, A. K., Rastogi, N., Sinha, P. R., Kumar, S., Tiwari, S., Wegner, T., 957 Baker,
N., Vignelles, D., Stenchikov, G., Shevchenko, I., Smith, J., Bedka, K., Kesarkar, A., Singh, V., Bhate, J., Ravikiran, 958 V., Durga
Rao, M., Ravindrababu, S., Patel, A., Vernier, H., Wienhold, F. G., Liu, H., Knepp, T. N., Thomason, L., 959 Crawford, J.,
Ziemba, L., Moore, J., Crumeyrolle, S., Williamson, M., Berthet, G., Jégou, F. and Renard, J. B.: BATAL: The 960—balloon
measurement campaigns of the Asian tropopause aerosol layer, *Bull. Am. Meteorol. Soc.*, 99(5), 955–973, 961
doi:10.1175/BAMS-D-17-0014.1, 2018.

962 Vernier, J. P., Kalnajs, L., Diaz, J. A., Reese, T., Corrales, E., Alan, A., Vernier, H., Holland, L., Patel, A., Rastogi, N.,
963—Wienhold, F., Carn, S., Krotkov, N. and Murray, J.: VolKilaui: Volcano rapid response balloon campaign during the 2018 964
Kilauea eruption, *Bull. Am. Meteorol. Soc.*, 101(10), E1602–E1618, doi:10.1175/BAMS-D-19-0011.1, 2020.

965 Weinzierl, B., Ansmann, A., Prospero, J. M., Althausen, D., Benker, N., Chouza, F., Dollner, M., Farrell, D., Fomba, W. K., 966
Freudenthaler, V., Gasteiger, J., Groß, S., Haerig, M., Heinold, B., Kandler, K., Kristensen, T. B., Mayol Bracero, O. L., 967
Müller, T., Reitebuch, O., Sauer, D., Schäfler, A., Schepanski, K., Spanu, A., Tegen, I., Toledano, C. and Walser, A.: The 968 Saharan
aerosol long-range transport and aerosol-cloud-interaction experiment: Overview and selected highlights, *Bull. Am. 969 Meteorol.*
Soc., 98(7), 1427–1451, doi:10.1175/BAMS-D-15-00142.1, 2017.

970 Wiegner, M., Madonna, F., Biniotoglou, I., Forkel, R., Gasteiger, J., Geiß, A., Pappalardo, G., Schäfer, K. and Thomas, W.: 971
What is the benefit of ceilometers for aerosol remote sensing? An answer from EARLINET, *Atmos. Meas. Tech.*, 7(7), 972
1979–1997, doi:10.5194/amt-7-1979-2014, 2014.

973 Winker, D. M., Hunt, W. H. and McGill, M. J.: Initial performance assessment of CALIOP, *Geophys. Res. Lett.*, 34(19), 1–974
5, doi:10.1029/2007GL030135, 2007.

975

976

977—Abbott, T. H. and Cronin, T. W.: Through Increases in Humidity, *Science* (80-.), 85(January), 83–85, 2021.

Brabec, M., Wienhold, F. G., Wüest, M., Krieger, U. and Peter, T.: A novel radiosonde payload to study upper tropospheric / lower stratospheric aerosol and clouds, 2008.

Brabec, M., Wienhold, F. G., Luo, B. P., VÄmel, H., Immler, F., Steiner, P., Hausammann, E., Weers, U. and Peter, T.: Particle backscatter and relative humidity measured across cirrus clouds and comparison with microphysical cirrus modelling, *Atmos. Chem. Phys.*, 12(19), 9135–9148, doi:10.5194/acp-12-9135-2012, 2012.

BRUCE A. ALBRECHT: Aerosols, Cloud Microphysics, and Fractional Cloudiness, *Science* (80-.), 245(4247), 24–29, 1989.

Brunamonti, S., Jorge, T., Oelsner, P., Hanumanthu, S., Singh, B. B., Ravi Kumar, K., Sonbawne, S., Meier, S., Singh, D., Wienhold, F. G., Ping Luo, B., Boettcher, M., Poltera, Y., Jauhiainen, H., Kayastha, R., Karmacharya, J., DIRksen, R., Naja, M., Rex, M., Fadnavis, S. and Peter, T.: Balloon-borne measurements of temperature, water vapor, ozone and aerosol backscatter on the southern slopes of the Himalayas during StratoClim 2016-2017, *Atmos. Chem. Phys.*, 18(21), 15937–15957, doi:10.5194/acp-18-15937-2018, 2018.

Brunamonti, S., Martucci, G., Romanens, G., Poltera, Y., Wienhold, F., Haeferle, A. and Navas-Guzmán, F.: Validation of aerosol backscatter profiles from Raman lidar and ceilometer using balloon-borne measurements, *Atmos. Chem. Phys. Discuss.*, (May), 1–31, doi:10.5194/acp-2020-294, 2020.

Cherian, T., Kumar, Y. B., Reddy, B. S., Optics, G., Limited, A., Nr, R. S. and Road, N.: LIDAR for Atmospheric Measurement and Probing, 5(84), 5114–5124, 2014.

Cirisan, A., Luo, B. P., Engel, I., Wienhold, F. G., Sprenger, M., Krieger, U. K., Weers, U., Romanens, G., Levrat, G., Jeannet, P., Ruffieux, D., Philipona, R., Calpini, B., Spichtinger, P. and Peter, T.: Balloon-borne match measurements of midlatitude cirrus clouds, *Atmos. Chem. Phys.*, 14(14), 7341–7365, doi:10.5194/acp-14-7341-2014, 2014.

COAKLEY, J. A., BERNSTEIN, R. L. and DURKEE, P. A.: Effect of Ship-Stack Effluents on Cloud Reflectivity, *Science* (80-.), 237(4818), 1020 LP – 1022, doi:10.1126/science.237.4818.1020, 1987.

Corrigan, C. E., Roberts, G. C., Ramana, M. V., Kim, D. and Ramanathan, V.: Capturing vertical profiles of aerosols and black carbon over the Indian Ocean using autonomous unmanned aerial vehicles, *Atmos. Chem. Phys.*, 8(3), 737–747, doi:10.5194/acp-8-737-2008, 2008.

Costantino, L. and Bréon, F. M.: Analysis of aerosol-cloud interaction from multi-sensor satellite observations, *Geophys. Res. Lett.*, 37(11), 1–5, doi:10.1029/2009GL041828, 2010.

Deshler, T., Hervig, M. E., Hofmann, D. J., Rosen, J. M. and Liley, J. B.: Thirty years of in situ stratospheric aerosol size distribution measurements from Laramie, Wyoming (41°N), using balloon-borne instruments, *J. Geophys. Res. Atmos.*, 108(5), 1–13, doi:10.1029/2002jd002514, 2003.

Fan, J., Wang, Y., Rosenfeld, D. and Liu, X.: Review of aerosol-cloud interactions: Mechanisms, significance, and challenges, *J. Atmos. Sci.*, 73(11), 4221–4252, doi:10.1175/JAS-D-16-0037.1, 2016.

Fan, J., Rosenfeld, D., Zhang, Y., Giangrande, S. E., Li, Z., Machado, L. A. T., Martin, S. T., Yang, Y., Wang, J., Artaxo, P., Barbosa, H. M. J., Braga, R. C., Comstock, J. M., Feng, Z., Gao, W., Gomes, H. B., Mei, F., Pöhlker, C., Pöhlker, M. L., Pöschl, U. and de Souza, R. A. F.: Substantial convection and precipitation enhancements by ultrafine aerosol particles, *Science* (80-.), 359(6374), 411–418, doi:10.1126/science.aan8461, 2018.

[Feingold, G., Eberhard, W. L., Veron, D. E. and Previdi, M.: First measurements of the Twomey indirect effect using ground-based remote sensors, *Geophys. Res. Lett.*, 30\(6\), 19–22, doi:10.1029/2002GL016633, 2003.](#)

[Feingold, G., Furrer, R., Pilewskie, P., Remer, L. A., Min, Q. and Jonsson, H.: Aerosol indirect effect studies at Southern Great Plains during the May 2003 Intensive Operations Period, *J. Geophys. Res. Atmos.*, 111\(5\), 1–13, doi:10.1029/2004JD005648, 2006.](#)

[Fujiwara, M., Shiotani, M., Hasebe, F., Vömel, H., Oltmans, S. J., Ruppert, P. W., Horinouchi, T. and Tsuda, T.: Performance of the Meteorolabor “Snow White” chilled-mirror hygrometer in the tropical troposphere: Comparisons with the Vaisala RS80 A/H-Humicap sensors, *J. Atmos. Ocean. Technol.*, 20\(11\), 1534–1542, doi:10.1175/1520-0426\(2003\)020<1534:POTMSW>2.0.CO;2, 2003.](#)

[Fujiwara, M., Sugidachi, T., Arai, T., Shimizu, K., Hayashi, M., Noma, Y., Kawagita, H., Sagara, K., Nakagawa, T., Okumura, S., Inai, Y., Shibata, T. and Iwasaki, S.: Development of a cloud particle sensor for radiosonde sounding, , \(May\), doi:10.5194/amt-2016-170, 2016a.](#)

[Fujiwara, M., Sugidachi, T., Arai, T., Shimizu, K., Hayashi, M., Noma, Y., Kawagita, H., Sagara, K., Nakagawa, T., Okumura, S., Inai, Y., Shibata, T., Iwasaki, S. and Shimizu, A.: Development of a cloud particle sensor for radiosonde sounding, *Atmos. Meas. Tech.*, 9\(12\), 5911–5931, doi:10.5194/amt-9-5911-2016, 2016b.](#)

[Girdwood, J., Smith, H., Stanley, W., Ulanowski, Z., Stopford, C., Chemel, C., Doulgieris, K. M., Brus, D., Campbell, D. and MacKenzie, R.: Design and field campaign validation of a multi-rotor unmanned aerial vehicle and optical particle counter, *Atmos. Meas. Tech.*, 13\(12\), 6613–6630, doi:10.5194/amt-13-6613-2020, 2020.](#)

[Girdwood, J., Stanley, W., Stopford, C. and Brus, D.: Simulation and Field Campaign Evaluation of an Optical Particle Counter on a Fixed-Wing UAV, *Atmos. Meas. Tech. Discuss.*, \(October\), 1–26, 2021.](#)

[Grosvenor, D. P., Sourdeval, O., Zuidema, P., Ackerman, A., Alexandrov, M. D., Bennartz, R., Boers, R., Cairns, B., Chiu, J. C., Christensen, M., Deneke, H., Diamond, M., Feingold, G., Fridlind, A., Hünerbein, A., Knist, C., Kollias, P., Marshak, A., McCoy, D., Merk, D., Painemal, D., Rausch, J., Rosenfeld, D., Russchenberg, H., Seifert, P., Sinclair, K., Stier, P., van Diedenhoven, B., Wendisch, M., Werner, F., Wood, R., Zhang, Z. and Quaas, J.: Remote Sensing of Droplet Number Concentration in Warm Clouds: A Review of the Current State of Knowledge and Perspectives, *Rev. Geophys.*, 56\(2\), 409–453, doi:10.1029/2017RG000593, 2018.](#)

[Gupta, G., Ratnam, M. V., Madhavan, B. L., Prasad, P. and Narayanamurthy, C. S.: Vertical and spatial distribution of elevated aerosol layers obtained using long-term ground-based and space-borne lidar observations, *Atmos. Environ.*, 246\(December 2020\), 118172, doi:10.1016/j.atmosenv.2020.118172, 2021.](#)

[Hanumanthu, S., Vogel, B., Müller, R., Brunamonti, S., Fadnavis, S., Li, D., Ölsner, P., Naja, M., Singh, B. B., Kumar, K. R., Sonbawne, S., Jauhainen, H., Vömel, H., Luo, B., Jorge, T., Wienhold, F. G., Dirksen, R. and Peter, T.: Strong day-to-day variability of the Asian Tropopause Aerosol Layer \(ATAL\) in August 2016 at the Himalayan foothills, *Atmos. Chem. Phys.*, 20\(22\), 14273–14302, doi:10.5194/acp-20-14273-2020, 2020.](#)

[Haywood, J. and Boucher, O.: Estimates of the direct and indirect radiative forcing due to tropospheric aerosols: A review, *Rev. Geophys.*, 38\(4\), 513–543, doi:10.1029/1999RG000078, 2000.](#)

[Inoue, J., Sato, K., Tobo, Y., Taketani, F. and Maturilli, M.: Advanced method for estimating the number concentration of cloud water and liquid water content observed by cloud particle sensor sondes, *Atmos. Meas. Tech. Discuss.*, 1–35, doi:10.5194/amt-2020-476, 2021.](#)

[IPCC: Climate Change 2021: The Physical Science Basis. Contribution of Working Group I to the Sixth Assessment Report of the](#)

Intergovernmental Panel on Climate Change, edited by V. Masson-Delmotte, P. Zhai, A. Pirani, S. L. Connors, C. Péan, S. Berger, N. Caud, Y. Chen, L. Goldfarb, M. I. Gomis, M. Huang, K. Leitzell, E. Lonnoy, J. B. R. Matthews, T. K. Maycock, T. Waterfield, O. Yelekçi, R. Yu, and B. Zhou, Cambridge University Press, Cambridge, United Kingdom and New York, NY, USA., 2021.

Jain, C. D., Madhavan, B. L. and Ratnam, M. V.: Source apportionment of rainwater chemical composition to investigate the transport of lower atmospheric pollutants to the UTLS region, Environ. Pollut., 248, 166–174, doi:10.1016/j.envpol.2019.02.007, 2019.

Jose, S., Nair, V. S. and Babu, S. S.: Anthropogenic emissions from South Asia reverses the aerosol indirect effect over the northern Indian Ocean, Sci. Rep., 10(1), 1–8, doi:10.1038/s41598-020-74897-x, 2020.

Kezoudi, M., Tesche, M., Smith, H., Tsekeri, A., Baars, H., Dollner, M., Estelle´s, V., Bu¨hl, J., Weinzierl, B., Ulanowski, Z., Mu¨ller, D. and Amiridis, V.: Measurement report: Balloon-borne in situ profiling of Saharan dust over Cyprus with the UCASS optical particle counter, Atmos. Chem. Phys., 21(9), 6781–6797, doi:10.5194/acp-21-6781-2021, 2021.

Kobayashi, E., Hoshino, S., Iwabuchi, M., Sugidachi, T., Shimizu, K. and Fujiwara, M.: Comparison of the GRUAN data products for Meisei RS-11G and Vaisala RS92-SGP radiosondes at Tateno (36.06°N, 140.13°E), Japan, Atmos. Meas. Tech., 12(6), 3039–3065, doi:10.5194/amt-12-3039-2019, 2019.

Koren, I., Remer, L. A., Altaratz, O., Martins, J. V. and Davidi, A.: Aerosol-induced changes of convective cloud anvils produce strong climate warming, Atmos. Chem. Phys., 10(10), 5001–5010, doi:10.5194/acp-10-5001-2010, 2010.

Kulkarni, J. R., Mahes Kumar, R. S., Morwal, S. B., Padma Kumari, B., Konwar, M., Deshpande, C. G., Joshi, R. R., Bhalwankar, R. V., Pandithurai, G., Safai, P. D., Narkhedkar, S. G., Dani, K. K., Nath, A., Nair, S., Sapre, V. V., Puranik, P. V., Kandalgaonkar, S. S., Mujumdar, V. R., Khaladkar, R. M., Vijayakumar, R., Prabha, T. V. and Goswami, B. N.: The cloud aerosol interaction and precipitation enhancement experiment (CAIPEEX): Overview and preliminary results, Curr. Sci., 102(3), 413–425, 2012.

L'Ecuyer, T. S.: Touring the atmosphere aboard the A-Train (vol 63, pg 36, 2010), Phys. Today, 64(8), 10, 2011.

Lohmann, U.: Aerosol effects on clouds and climate, Space Sci. Rev., 125(1–4), 129–137, doi:10.1007/s11214-006-9051-8, 2006.

Lohmann, U. and Feichter, J.: Global indirect aerosol effects: a review, Atmos. Chem. Phys. Discuss., 4(6), 7561–7614, doi:10.5194/acpd-4-7561-2004, 2004.

Mamali, D., Marinou, E., Sciare, J., Pikridas, M., Kokkalis, P., Kottas, M., Biniotoglou, I., Tsekeri, A., Keleshis, C., Engelmann, R., Baars, H., Ansmann, A., Amiridis, V., Russchenberg, H. and Biskos, G.: Vertical profiles of aerosol mass concentration derived by unmanned airborne in situ and remote sensing instruments during dust events, Atmos. Meas. Tech., 11(5), 2897–2910, doi:10.5194/amt-11-2897-2018, 2018.

McComiskey, A. and Feingold, G.: The scale problem in quantifying aerosol indirect effects, Atmos. Chem. Phys., 12(2), 1031–1049, doi:10.5194/acp-12-1031-2012, 2012.

McComiskey, A., Feingold, G., Frisch, A. S., Turner, D. D., Miller, M. A., Chiu, J. C., Min, Q. and Ogren, J. A.: An assessment of aerosol-cloud interactions in marine stratus clouds based on surface remote sensing, J. Geophys. Res. Atmos., 114(9), 1–15, doi:10.1029/2008JD011006, 2009.

Mishra, M. K., Rajeev, K., Thampi, B. V., Parameswaran, K. and Nair, A. K. M.: Micro pulse lidar observations of mineral dust layer in the lower troposphere over the southwest coast of Peninsular India during the Asian summer monsoon season, J. Atmos. Solar-Terrestrial Phys., 72(17), 1251–1259, doi:10.1016/j.jastp.2010.08.012, 2010.

Murphy, D. M. and Koop, T.: Review of the vapour pressures of ice and supercooled water for atmospheric applications, Q. J. R. Meteorol. Soc., 131(608), 1539–1565, doi:10.1256/qj.04.94, 2005.

Narendra Reddy, N., Venkat Ratnam, M., Basha, G. and Ravikiran, V.: Cloud vertical structure over a tropical station obtained using long-term high resolution Radiosonde measurements, Atmos. Chem. Phys. Discuss., 1–49, doi:10.5194/acp-2018-194, 2018.

Pandit, A. K., Gadhavi, H., Ratnam, M. V., Jayaraman, A., Raghunath, K. and Rao, S. V. B.: Characteristics of cirrus clouds and tropical tropopause layer: Seasonal variation and long-term trends, J. Atmos. Solar-Terrestrial Phys., 121(PB), 248–256, doi:10.1016/j.jastp.2014.07.008, 2014.

Pandit, A. K., Gadhavi, H. S., Ratnam, M. V., Raghunath, K., Rao, S. V. B. and Jayaraman, A.: Long-term trend analysis and climatology of tropical cirrus clouds using 16 years of lidar data set over Southern India, Atmos. Chem. Phys., 15(24), 13833–13848, doi:10.5194/acp-15-13833-2015, 2015.

Pandithurai, G., Takamura, T., Yamaguchi, J., Miyagi, K., Takano, T., Ishizaka, Y., Dipu, S. and Shimizu, A.: Aerosol effect on cloud droplet size as monitored from surface-based remote sensing over East China Sea region, Geophys. Res. Lett., 36(13), 1–5, doi:10.1029/2009GL038451, 2009.

Prasad, P., Raman, M. R., Ratnam, M. V., Ravikiran, V., Madhavan, B. L. and Bhaskara, S. V.: Nocturnal, seasonal and intra-annual variability of tropospheric aerosols observed using ground-based and space-borne lidars over a tropical location of India, Atmos. Environ., 213(May), 185–198, doi:10.1016/j.atmosenv.2019.06.008, 2019.

Radke, L. F., Coakley, J. A. and King, M. D.: Direct and remote sensing observations of the effects of ships on clouds, Science (80-.), 246(4934), 1146–1149, doi:10.1126/science.246.4934.1146, 1989.

Rao, P. B., Jain, A. R., Kishore, P., Balamuralidhar, P., Damle, S. H. and Viswanathan, G.: Indian MST radar 1. System description and sample vector wind measurements in ST mode, Radio Sci., 30(4), 1125–1138, doi:10.1029/95RS00787, 1995.

Ratnam, M. V., Prasad, P., Raman, M. R., Ravikiran, V., Bhaskara, S. V., Murthy, B. V. K. and Jayaraman, A.: Role of dynamics on the formation and maintenance of the elevated aerosol layer during monsoon season over south-east peninsular India, , 188(June), 43–49, doi:10.1016/j.atmosenv.2018.06.023, 2018.

Redemann, J., Wood, R., Zuidema, P., Doherty, S., Luna, B., LeBlanc, S., Diamond, M., Shinozuka, Y., Chang, I., Ueyama, R., Pfister, L., Ryoo, J., Dobracki, A., da Silva, A., Longo, K., Kacenelenbogen, M., Flynn, C., Pistone, K., Knox, N., Piketh, S., Haywood, J., Formenti, P., Mallet, M., Stier, P., Ackerman, A., Bauer, S., Fridlind, A., Carmichael, G., Saide, P., Ferrada, G., Howell, S., Freitag, S., Cairns, B., Holben, B., Knobelspiesse, K., Tanelli, S., L’Ecuyer, T., Dzambo, A., Sy, O., McFarquhar, G., Poellot, M., Gupta, S., O’Brien, J., Nenes, A., Kacarab, M., Wong, J., Small-Griswold, J., Thornhill, K., Noone, D., Podolske, J., Schmidt, K. S., Pilewskie, P., Chen, H., Cochrane, S., Sedlacek, A., Lang, T., Stith, E., Segal-Rozenhaimer, M., Ferrare, R., Burton, S., Hostetler, C., Diner, D., Platnick, S., Myers, J., Meyer, K., Spangenberg, D., Maring, H. and Gao, L.: An overview of the ORACLES (ObSeRvations of Aerosols above CLouds and their intEractionS) project: aerosol-cloud-radiation interactions in the Southeast Atlantic basin, Atmos. Chem. Phys., 1–82, doi:10.5194/acp-2020-449, 2020.

Rosen, J. M. and Kjome, N. T.: Backscattersonde: a new instrument for atmospheric aerosol research, Appl. Opt., 30(12), 1552, doi:10.1364/ao.30.001552, 1991.

Rosenfeld, D., Lohmann, U., Raga, G. B., O’Dowd, C. D., Kulmala, M., Fuzzi, S., Reissell, A. and Andreae, M. O.: Flood or drought: How

[do aerosols affect precipitation?, Science \(80-. \), 321\(5894\), 1309–1313, doi:10.1126/science.1160606, 2008.](#)

[Rosenfeld, D., Sherwood, S., Wood, R. and Donner, L.: Climate Effects of Aerosol-Cloud Interactions, Science \(80-. \), 343\(6169\), 379 LP – 380, doi:10.1126/science.1247490, 2014a.](#)

[Rosenfeld, D., Andreae, M. O., Asmi, A., Chin, M., Leeuw, G., Donovan, D. P., Kahn, R., Kinne, S., Kivekäs, N., Kulmala, M., Lau, W., Schmidt, K. S., Suni, T., Wagner, T., Wild, M. and Quaas, J.: Reviews of Geophysics, , 1–59, doi:10.1002/2013RG000441.Received, 2014b.](#)

[Sarna, K. and Russchenberg, H. W. J.: Ground-based remote sensing scheme for monitoring aerosol-cloud interactions, Atmos. Meas. Tech., 9\(3\), 1039–1050, doi:10.5194/amt-9-1039-2016, 2016.](#)

[Sarna, K. and Russchenberg, H. W. J.: Monitoring aerosol-cloud interactions at the CESAR Observatory in the Netherlands, Atmos. Meas. Tech., 10\(5\), 1987–1997, doi:10.5194/amt-10-1987-2017, 2017.](#)

[Sathiyamoorthy, V., Mahesh, C., Gopalan, K., Prakash, S., Shukla, B. P. and Mathur, A. K.: Characteristics of low clouds over the Arabian Sea, , 118\(December\), 489–503, doi:10.1002/2013JD020553, 2013.](#)

[Schmidt, J., Ansmann, A., Bühl, J., Baars, H., Wandinger, U., Müller, D. and Malinka, A. V.: Dual-FOV raman and Doppler lidar studies of aerosol-cloud interactions: Simultaneous profiling of aerosols, warm-cloud properties, and vertical wind, J. Geophys. Res., 119\(9\), 5512–5527, doi:10.1002/2013JD020424, 2014.](#)

[Schmidt, J., Ansmann, A., Bühl, J. and Wandinger, U.: Strong aerosol-cloud interaction in altocumulus during updraft periods: Lidar observations over central Europe, Atmos. Chem. Phys., 15\(18\), 10687–10700, doi:10.5194/acp-15-10687-2015, 2015.](#)

[Seinfeld, J. H., Bretherton, C., Carslaw, K. S., Coe, H., DeMott, P. J., Dunlea, E. J., Feingold, G., Ghan, S., Guenther, A. B., Kahn, R., Kraucunas, I., Kreidenweis, S. M., Molina, M. J., Nenes, A., Penner, J. E., Prather, K. A., Ramanathan, V., Ramaswamy, V., Rasch, P. J., Ravishankara, A. R., Rosenfeld, D., Stephens, G. and Wood, R.: Improving our fundamental understanding of the role of aerosol-cloud interactions in the climate system, Proc. Natl. Acad. Sci. U. S. A., 113\(21\), 5781–5790, doi:10.1073/pnas.1514043113, 2016.](#)

[Sena, E. T., McComiskey, A. and Feingold, G.: A long-term study of aerosol-cloud interactions and their radiative effect at the Southern Great Plains using ground-based measurements, Atmos. Chem. Phys., 16\(17\), 11301–11318, doi:10.5194/acp-16-11301-2016, 2016.](#)

[Small, J. D., Chuang, P. Y., Feingold, G. and Jiang, H.: Can aerosol decrease cloud lifetime?, Geophys. Res. Lett., 36\(16\), 1–5, doi:10.1029/2009GL038888, 2009.](#)

[Smith, H. R., Ulanowski, Z., Kaye, P. H., Hirst, E., Stanley, W., Kaye, R., Wieser, A., Stopford, C., Kezoudi, M., Girdwood, J., Greenaway, R. and Mackenzie, R.: The Universal Cloud and Aerosol Sounding System \(UCASS\): A low-cost miniature optical particle counter for use in dropsonde or balloon-borne sounding systems, Atmos. Meas. Tech., 12\(12\), 6579–6599, doi:10.5194/amt-12-6579-2019, 2019.](#)

[Srinivasulu, P., Yasodha, P., Kamaraj, P., Rao, T. N., Jayaraman, A., Reddy, S. N. and Satyanarayana, S.: 1280-MHz active array radar wind profiler for lower atmosphere: System description and data validation, J. Atmos. Ocean. Technol., 29\(10\), 1455–1470, doi:10.1175/JTECH-D-12-00030.1, 2012.](#)

[Stein, A. F., Draxler, R. R., Rolph, G. D., Stunder, B. J. B., Cohen, M. D. and Ngan, F.: Noaa’s hysplit atmospheric transport and dispersion modeling system, Bull. Am. Meteorol. Soc., 96\(12\), 2059–2077, doi:10.1175/BAMS-D-14-00110.1, 2015.](#)

[Twomey, S.: The Influence of Pollution on the Shortwave Albedo of Clouds, J. Atmos. Sci., 34\(7\), 1149–1152, doi:10.1175/1520-0469\(1977\)034<1149:TIOPOT>2.0.CO;2, 1977.](#)

[Vernier, J., Fairlie, T. D., Natarajan, M., Wienhold, F. G., Bian, J., Martinsson, B. G., Crumeyrolle, S., Thomason, L. W. and Bedka, K. M.: Journal of Geophysical Research : Atmospheres, , doi:10.1002/2014JD022372.Received, 2015.](#)

[Vernier, J. P., Fairlie, T. D., Deshler, T., Venkat Ratnam, M., Gadhavi, H., Kumar, B. S., Natarajan, M., Pandit, A. K., Akhil Raj, S. T., Hemanth Kumar, A., Jayaraman, A., Singh, A. K., Rastogi, N., Sinha, P. R., Kumar, S., Tiwari, S., Wegner, T., Baker, N., Vignelles, D., Stenchikov, G., Shevchenko, I., Smith, J., Bedka, K., Kesarkar, A., Singh, V., Bhate, J., Ravikiran, V., Durga Rao, M., Ravindrababu, S., Patel, A., Vernier, H., Wienhold, F. G., Liu, H., Knepp, T. N., Thomason, L., Crawford, J., Ziemba, L., Moore, J., Crumeyrolle, S., Williamson, M., Berthet, G., Jégou, F. and Renard, J. B.: BATAL: The balloon measurement campaigns of the Asian tropopause aerosol layer, Bull. Am. Meteorol. Soc., 99\(5\), 955–973, doi:10.1175/BAMS-D-17-0014.1, 2018.](#)

[Vernier, J. P., Kalnajs, L., Diaz, J. A., Reese, T., Corrales, E., Alan, A., Vernier, H., Holland, L., Patel, A., Rastogi, N., Wienhold, F., Carn, S., Krotkov, N. and Murray, J.: VolKilau: Volcano rapid response balloon campaign during the 2018 Kilauea eruption, Bull. Am. Meteorol. Soc., 101\(10\), E1602–E1618, doi:10.1175/BAMS-D-19-0011.1, 2020.](#)

[Weinzierl, B., Ansmann, A., Prospero, J. M., Althausen, D., Benker, N., Chouza, F., Dollner, M., Farrell, D., Fomba, W. K., Freudenthaler, V., Gasteiger, J., Groß, S., Haarig, M., Heinold, B., Kandler, K., Kristensen, T. B., Mayol-Bracero, O. L., Müller, T., Reitebuch, O., Sauer, D., Schäfler, A., Schepanski, K., Spanu, A., Tegen, I., Toledano, C. and Walser, A.: The Saharan aerosol long-range transport and aerosol-cloud-interaction experiment: Overview and selected highlights, Bull. Am. Meteorol. Soc., 98\(7\), 1427–1451, doi:10.1175/BAMS-D-15-00142.1, 2017.](#)

[Wiegner, M., Madonna, F., Biniotoglou, I., Forkel, R., Gasteiger, J., Geiß, A., Pappalardo, G., Schäfer, K. and Thomas, W.: What is the benefit of ceilometers for aerosol remote sensing? An answer from EARLINET, Atmos. Meas. Tech., 7\(7\), 1979–1997, doi:10.5194/amt-7-1979-2014, 2014.](#)

[Winker, D. M., Hunt, W. H. and McGill, M. J.: Initial performance assessment of CALIOP, Geophys. Res. Lett., 34\(19\), 1–5, doi:10.1029/2007GL030135, 2007.](#)

Tables
978
979
980
981
982
983
984
985
986
987
988
989
990
991
992
993
994

Table 1. List of instruments deployed (in BACIS) and the corresponding physical parameters obtained.

Sl. No.	Instrument	Purpose	Physical quantity (Unit)
1	CALIPSO	Aerosol and cloud profiling	Total attenuated backscatter($\text{km}^{-1}\text{sr}^{-1}$)
2	MPL	Aerosol and cloud profiling	Backscatter coefficient($\text{m}^{-1}\text{sr}^{-1}$)
3	Mie Lidar	Aerosol and cloud profiling	Backscatter coefficient($\text{km}^{-1}\text{sr}^{-1}$)
4	COBALD	In-situ measurement of aerosol and cloud particles	Backscatter ratio
5	CPS	In situ measurement of cloud particles	Cloud particle number concentration($\#/cc$), degree of polarization(DOP)
6	MST Radar	3-D Wind components, turbulence	Horizontal and vertical wind components(m/s)
7	LAWP	3-D Wind components, turbulence	Horizontal and vertical wind components (m/s)
8	MWR	Meteorological parameters and cloud	Temperature($^{\circ}\text{C}$), RH(%) and cloud liquid water content(g/m^3)
9	ICON	Ambient aerosol	BC concentration ($\mu\text{g/m}^3$), Scattering coefficient and absorption coefficient (m^{-1})
10	Ceilometer	Boundary layer, cloud and aerosol	Back scatter Backscatter coefficient($\text{km}^{-1}\text{sr}^{-1}$)

995

996

997
998

Table. 2. Date and time of the BACIS campaigns and the instruments operated during the corresponding ~~campaign~~campaigns.

S. No.	Date & Time (LT)	MPL	Mie	Ceil	CPS	COB	MST	MWR	Aeth	CALI	LAWP
1	06-06-2017; 01:57	Y	Y	N	Y	Y	Y	N	Y	Y	Y
2	08-07-2017; 01:36	Y	Y	N	Y	Y	N	N	Y	Y	Y
3	29-09-2018; 01:46	Y	Y	N	Y	Y	N	N	Y	N	Y
4	01-11-2018; 22:13	N	Y	N	Y	Y	N	N	Y	N	Y
5	23-03-2019; 02:36	N	Y	Y	Y	Y	Y	N	Y	N	Y
6	30-04-2019; 23:16	N	Y	Y	Y	Y	Y	N	Y	N	Y

999

7	30-05-2019; 23:46	N	Y	Y	Y	Y	Y	N	Y	N	Y
8	27-06-2019; 23:45	N	Y	Y	Y	Y	Y	N	Y	N	Y
9	28-08-2019; 23:42	N	Y	Y	Y	Y	Y	N	Y	N	Y
10	09-10-2019; 23:36	N	Y	Y	Y	Y	Y	N	Y	N	Y
11	20-12-2019; 21:20	N	Y	Y	Y	Y	Y	Y	Y	N	Y
12	04-02-2020; 00:27	N	Y	Y	Y	Y	Y	N	Y	N	Y
13	10-03-2020; 00:26	N	Y	Y	Y	Y	Y	N	Y	N	Y
14	19-06-2020; 23:26	N	Y	Y	Y	Y	Y	Y	Y	N	Y
15	19-08-2020; 22:39	N	Y	Y	Y	Y	Y	N	Y	N	Y
MPL – Micro Pulse Lidar; Mie – Mie Lidar; Ceil – Ceilometer; CPS – Cloud Particle Sensor (CPS); COB – Compact Optical Backscatter Aerosol Detector (COBALD); MST – Indian MST Radar; LAWP – Lower Atmospheric Wind Profiler (LAWP); Aeth – Aethalometer; CALI – Calipso; MWR – Micro Wave Radiometer.											

~~+000~~
~~+001~~
~~+002~~
~~+003~~

~~+004~~
~~+005~~

Table 3. ~~Cele~~
~~#Col~~
~~our~~
Index
(CI)
and
other
phys
ical
para
mete
rs of
the
ice
clou
ds.
~~Back~~
~~scatt~~
~~e~~
~~Th~~
~~e~~
~~back~~
~~scatt~~
~~er~~
ratio
(BS
R) in
norm
al
(Itali
c)
font
is for
a 450
nm
(940
nm)
chan
nel.

							conc. (#/cc)
06-Jun-2017	1	13- 15.5	-53 to -74	~ SRH	19.2 (19.2)	5.6(4.8) 90.4(73)	10 ⁻² to 10 ⁻¹
08-Jul-2017	2	10.5-16	-34 to -78	> SRH	18.7(18.6)	3(2.9) 37.5(35.2)	10 ⁻² to 10 ⁻¹
01-Nov-2018	4	12-12.6	-47 to -53	> SRH	19.5	17.2(17.5) 318(313.5)	10 ⁻¹ to 1
30-Apr-2019	6	9.3-16	-22 to -79	~SRH	19.4(19.3)	16.4(8.6) 302(147)	10 ⁻¹ to 1
30-May-2019	7	16.2- 17.4	-78 to -84.5	<SRH	18	1.6(1.4) 12.2(8.7)	10 ⁻³ to 10 ⁻²
27-Jun-2019	8	9.4-10.7	-23.7 to -35.2	>SRH	19.3(17.9)	5.1(3.1) 74.8(43.2)	10 ⁻¹ to 1
19-Jun-2020	14	14.2- 15.4	-62 to -75	<SRH	21	7.9(7.9) 147.4(143.2)	10 ⁻¹ to 1

Date	Campaign no	Ice cloud altitude (km)	Temperatur e Temperatu re range (°C)	RH condition	Mean (median) CI	Mean (median) BSR	Range of peak ice particle no
------	----------------	----------------------------------	---	-----------------	------------------------	-------------------------	--

~~+006~~
~~+007~~
~~+008~~
~~+009~~
~~+010~~

~~+011~~
~~+012~~

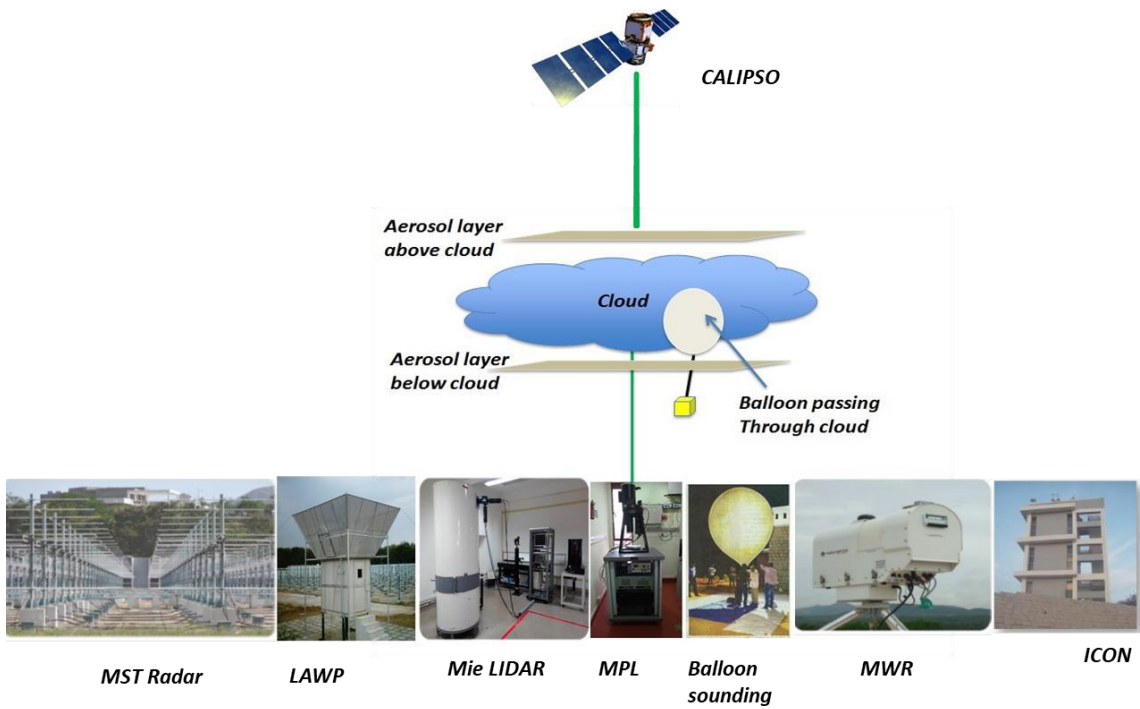
able 4. ColorC
olour
Index
(CI)
and
backsc
atter
ratio
(BSR)
of non-
spheric
al
(coarse
)
particle
layers
as
identi
ed by
CPS
sonde.
The
BSR in
normal
(italic)
font is
for 450
nm
(940
nm).
Blue
(red)
color
values
are
observ
ed in
the
monso
on (pre-
monso
on)
months
:

s
o
n
d

e. The BSR in the normal (italic) font is 450 nm (940 nm). Blue (red) colour values are observed in the monsoon (pre-monsoon) months.

Campaign Date	Non-spherical layer altitude (km)	Temperature range (°C)	RH range (%)	Mean (median) CI	Mean (median) BSR
06-Jun-2017	0.5-2.5	27.6 to 15.5	63.5-81.3	12.3(12.5)	1.45(1.4) 6.5(6)
08-Jul-2017	0.5-2.5	25.3 to 14.7	64.2-96.4	14.6(14.8)	2 15.8
29-Sep-2018	0.5-1	22.6 to 20	92-94	12.3	3.3(3.2) 30(29)
27-Jun-2019	0.5-1.5	27.6 to 19.8	57.3-70.3	11.4	1.6 7.6
19-Jun-2020	0.5-2.5	28.8 to 14.2	57.2-94.4	12.6(12.8)	1.6 8(8.1)
23-Mar-2019	1.5-3.5	23 to 6.5	32.7-70.3	12.6(12.8)	2 13
30-Apr-2019	0.5-4	28 to 4.5	60.2-97.3	12.2(12.6)	3.3(2.6) 28(21.5)
30-May-2019	0.5-5	28.8 to -0.1	60-98	11.7(11.6)	3.2(2.9) 25.7(22)

1013
1014



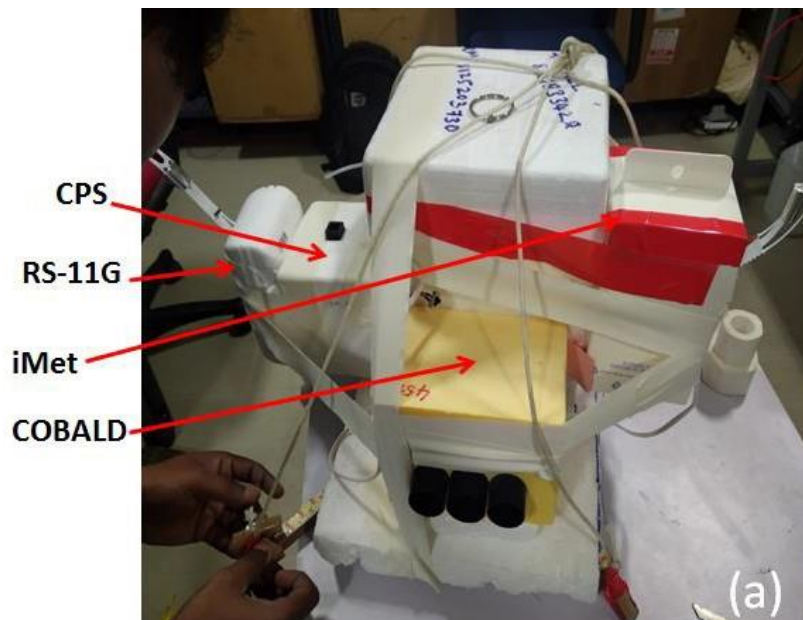
1015
1016
1017
1018
1019
1020
1021
1022
1023
1024
1025
1026
1027
1028
1029
1030
1031
1032
1033
1034
1035
1036
1037
1038
1039
1040

d Interaction Studies (BACIS) campaign.



Figure 1. Schematic diagram showing the observational concept of the Ballroom-born Aero-sol Clou

1041

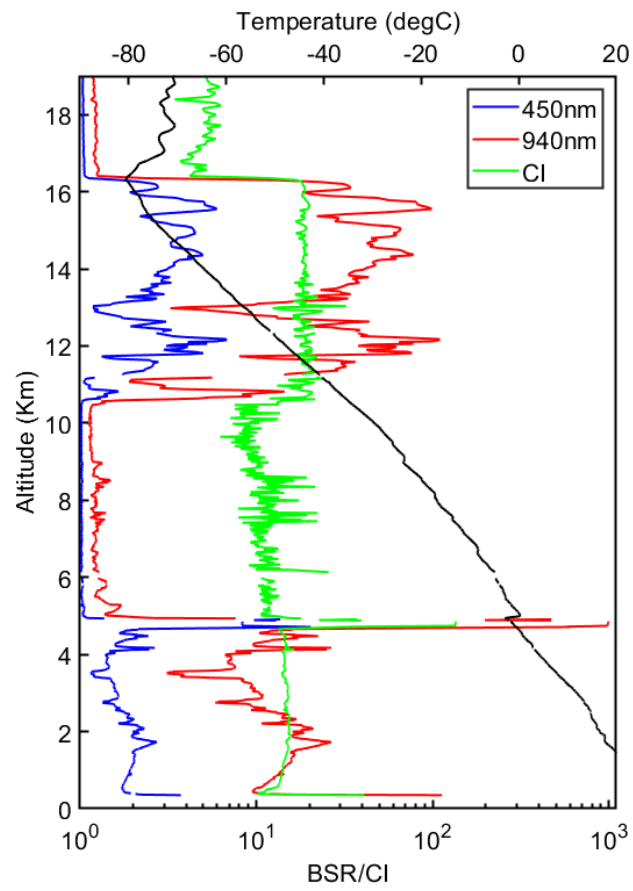


1042
1043
1044
1045
1046
1047
1048
1049
1050

ch preparations at the launch field with the payload and balloon.

C
RS-
iMet
COB

Figure 2. Phot ogra ph show s (a) the ballo on payl oad with COB ALD , iMet radio sond e, CPS, RS- 11G radio sond e, and (b) pre- laun



1051
 1052
 1053
 1054
 1055
 1056
 1057
 1058
 1059
 1060
 1061
 1062
 1063
 1064
 1065

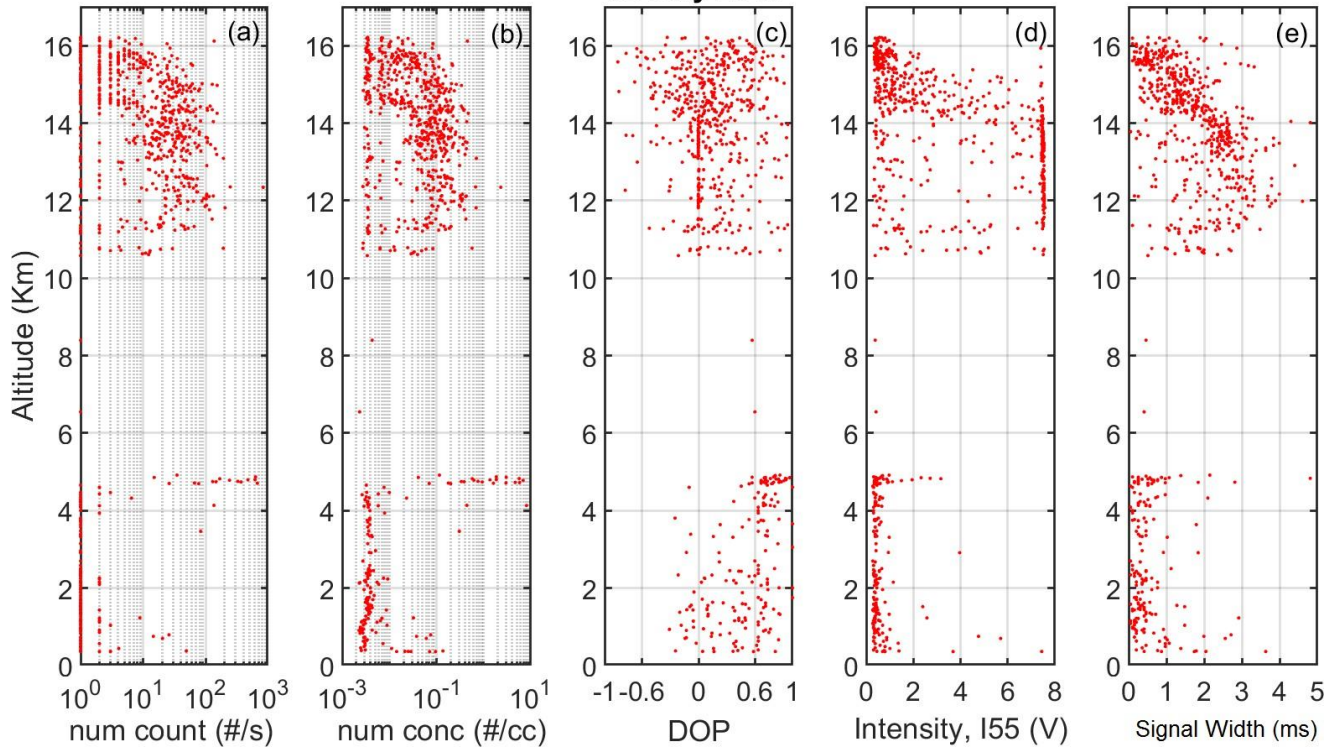
nm) channels were obtained using a COBALD sonde launched during the second pilot campaign (08 July 2017). ~~Color~~Colour Index (CI) estimated from BSR at both channels is also shown (in green ~~color~~colour).

Altitude (Km)
18
16
14
12
10
8
6
4
2
0
1

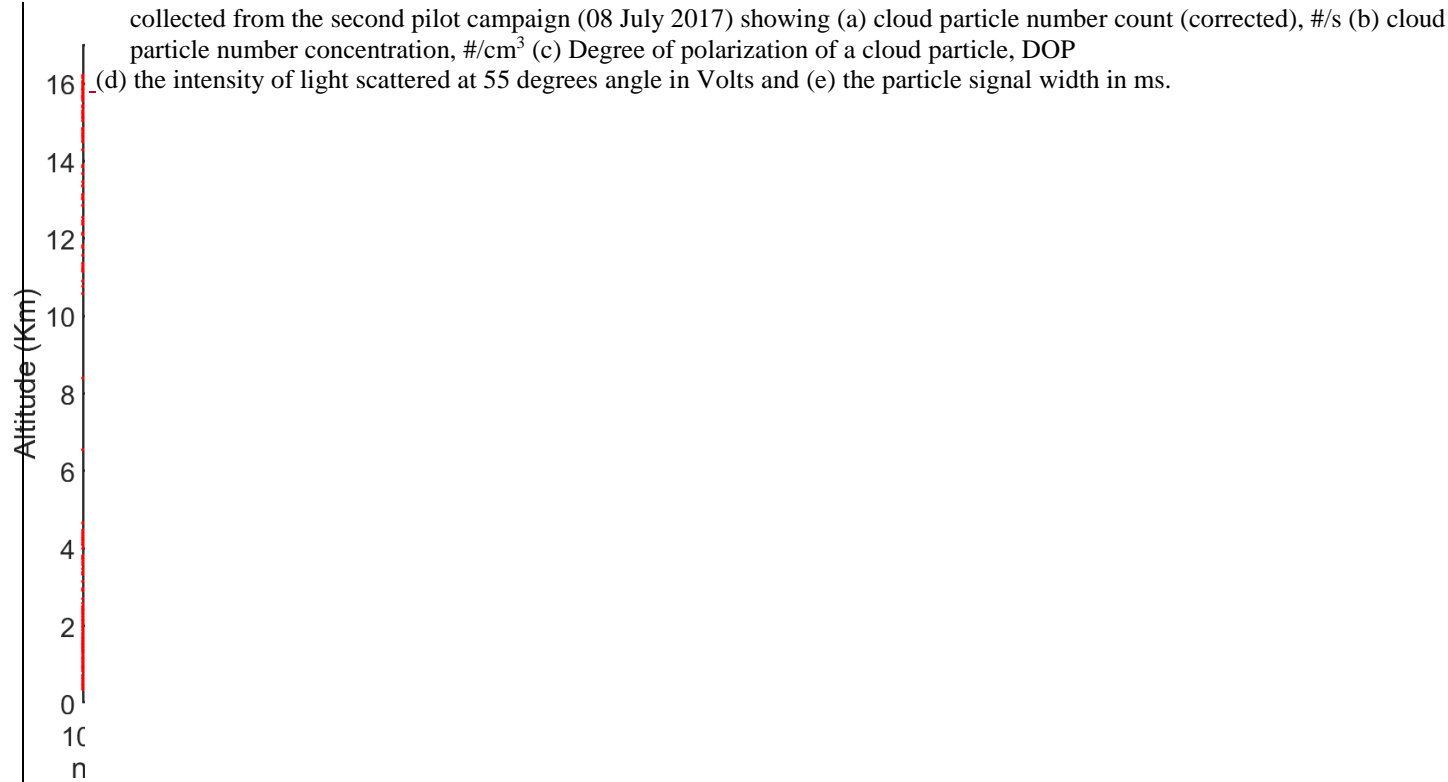
Figure

3.
Back
scatt
er
ratio
(BS
R) at
blue
(450
nm)
and
red
(940

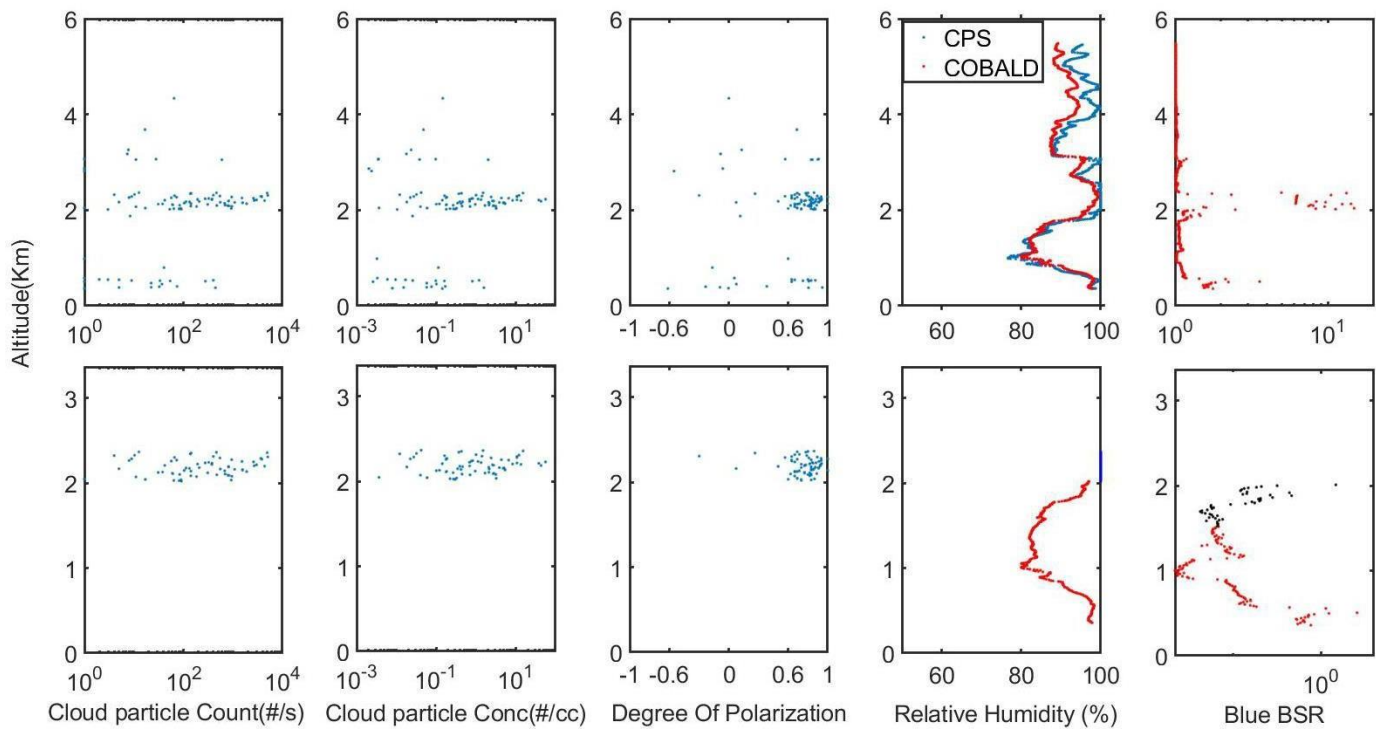
08-July-2017



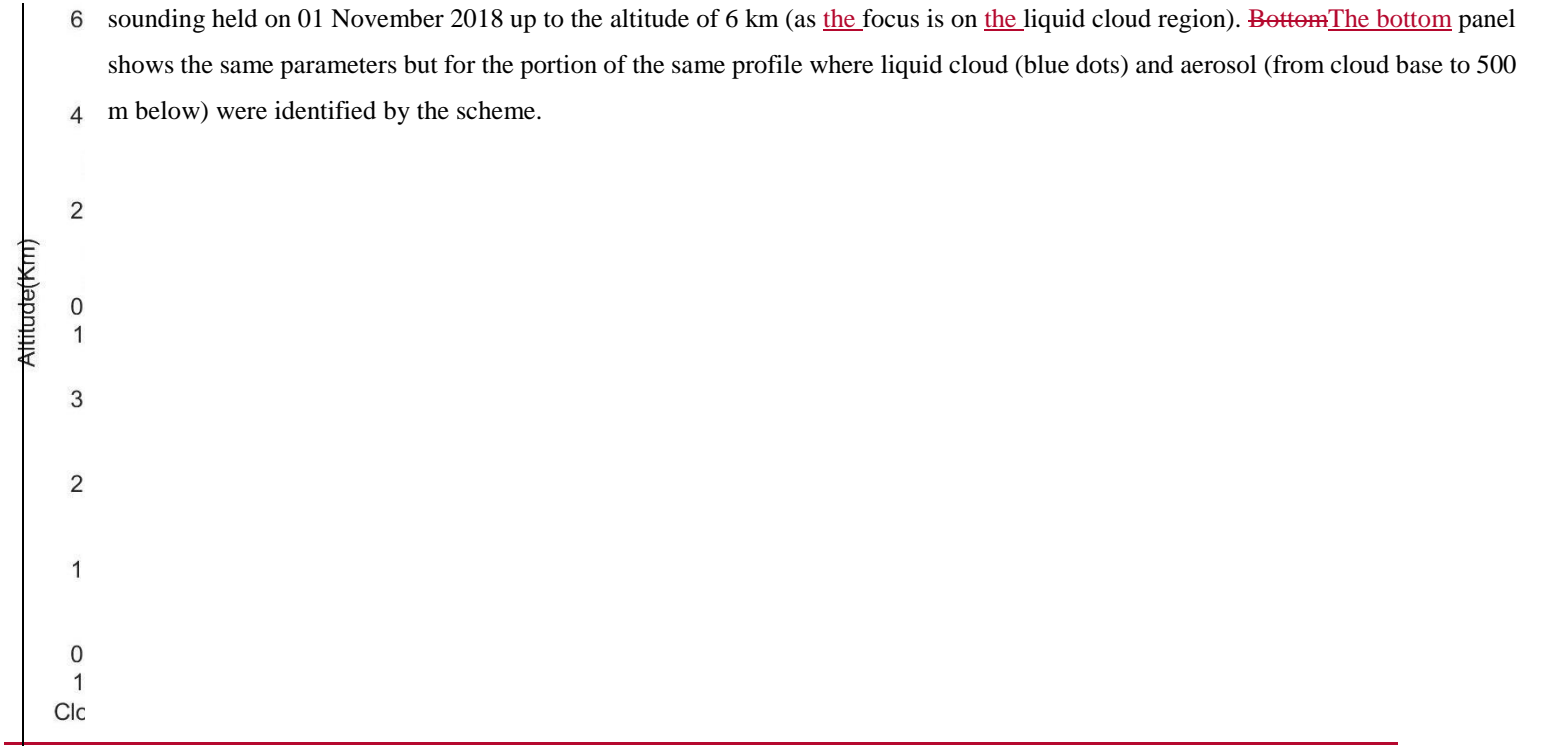
+066
+067
+068
+069
+070
+071
+072
+073
+074
+075
+076
+077
+078
+079
+080



F
i
g
u
r
e
4
•
C
P
S
m
e
a
s
u
r
e
m
e
n
t
s



1081
1082
1083
1084
1085
1086
1087



Figure

5.

The

top

pane

l

show

s

COB

ALD

and

CPS

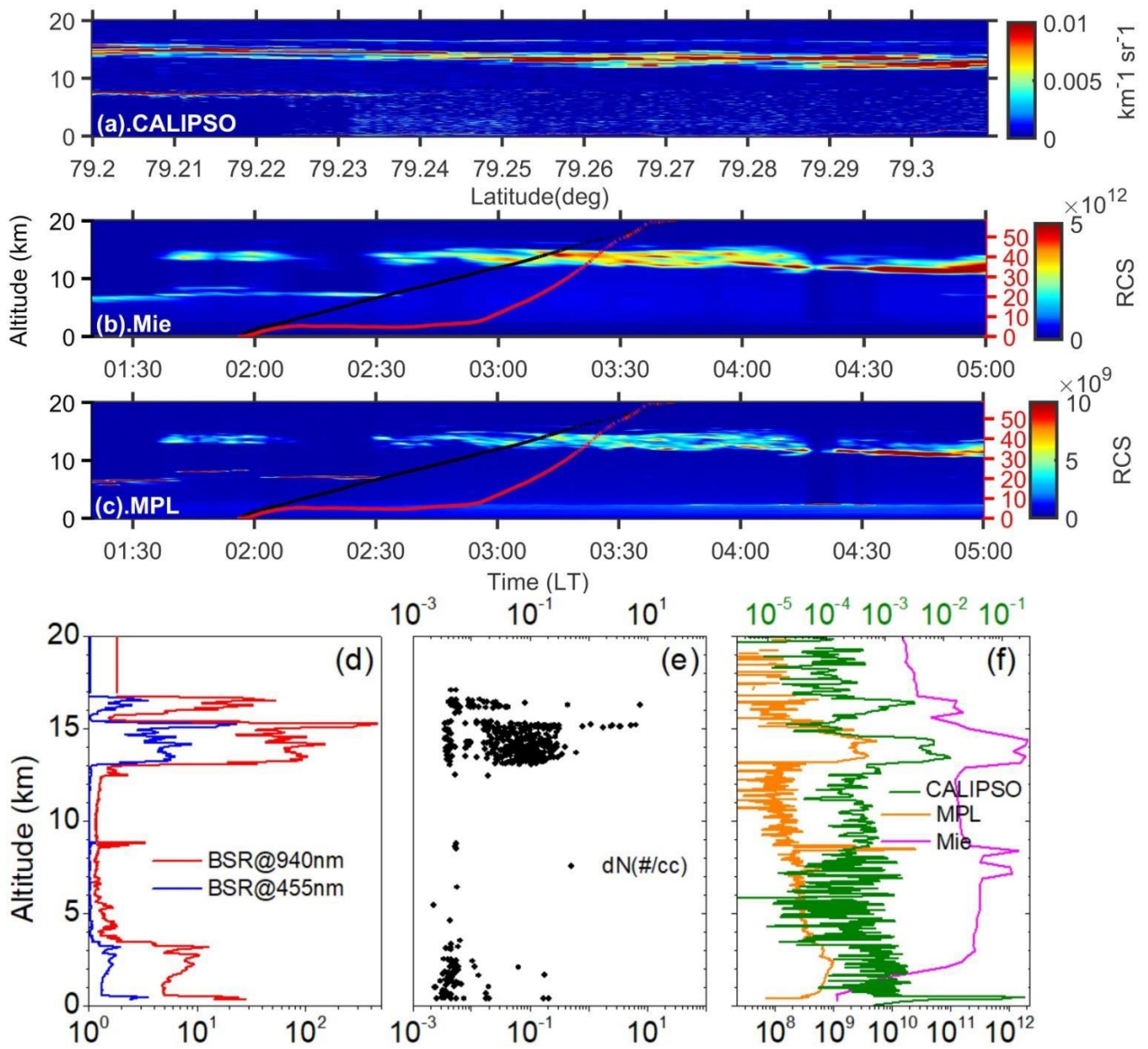
obse

rvati

ons

from

a



1088
1089
1090
1091
1092
1093
1094
1095
1096
1097

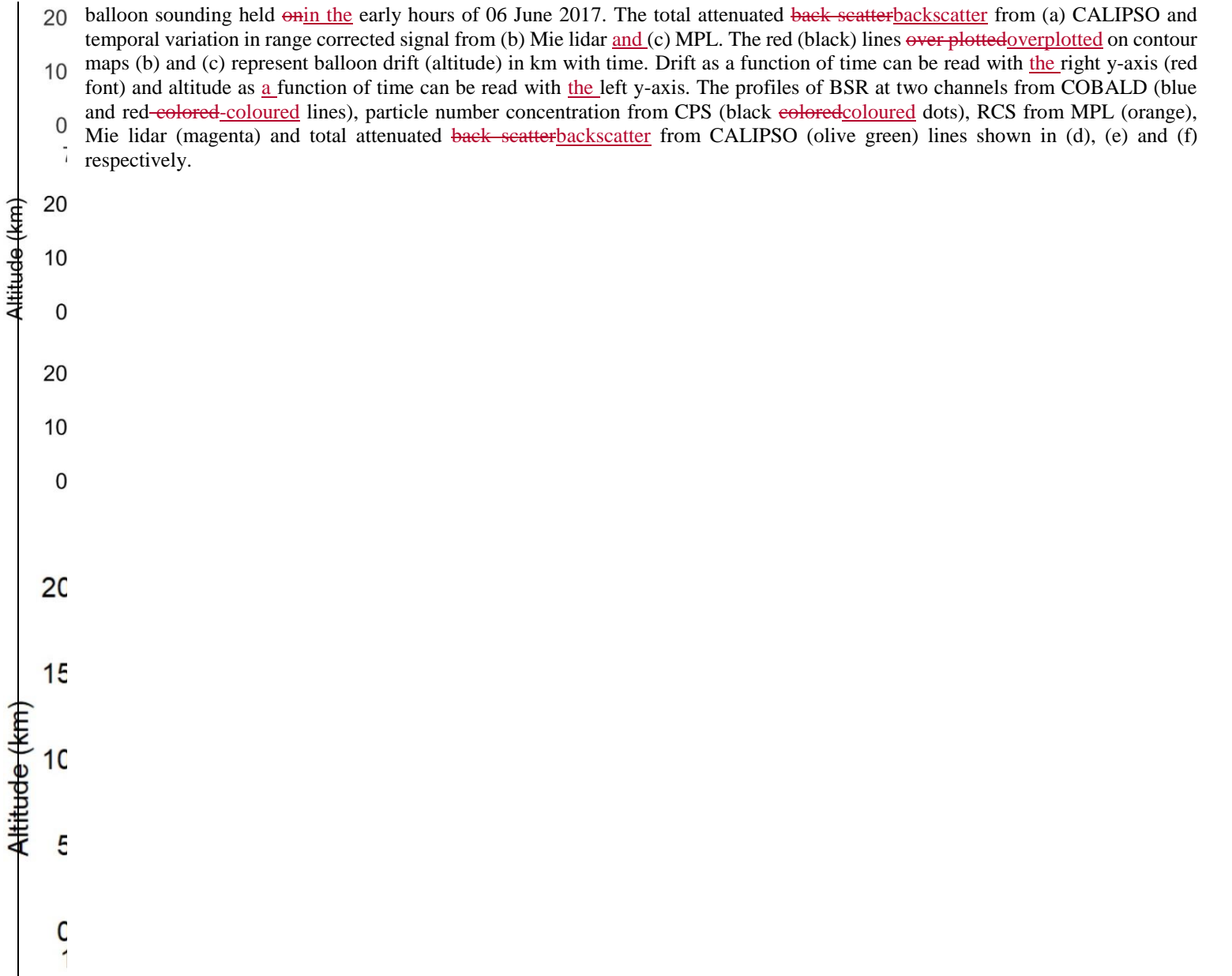
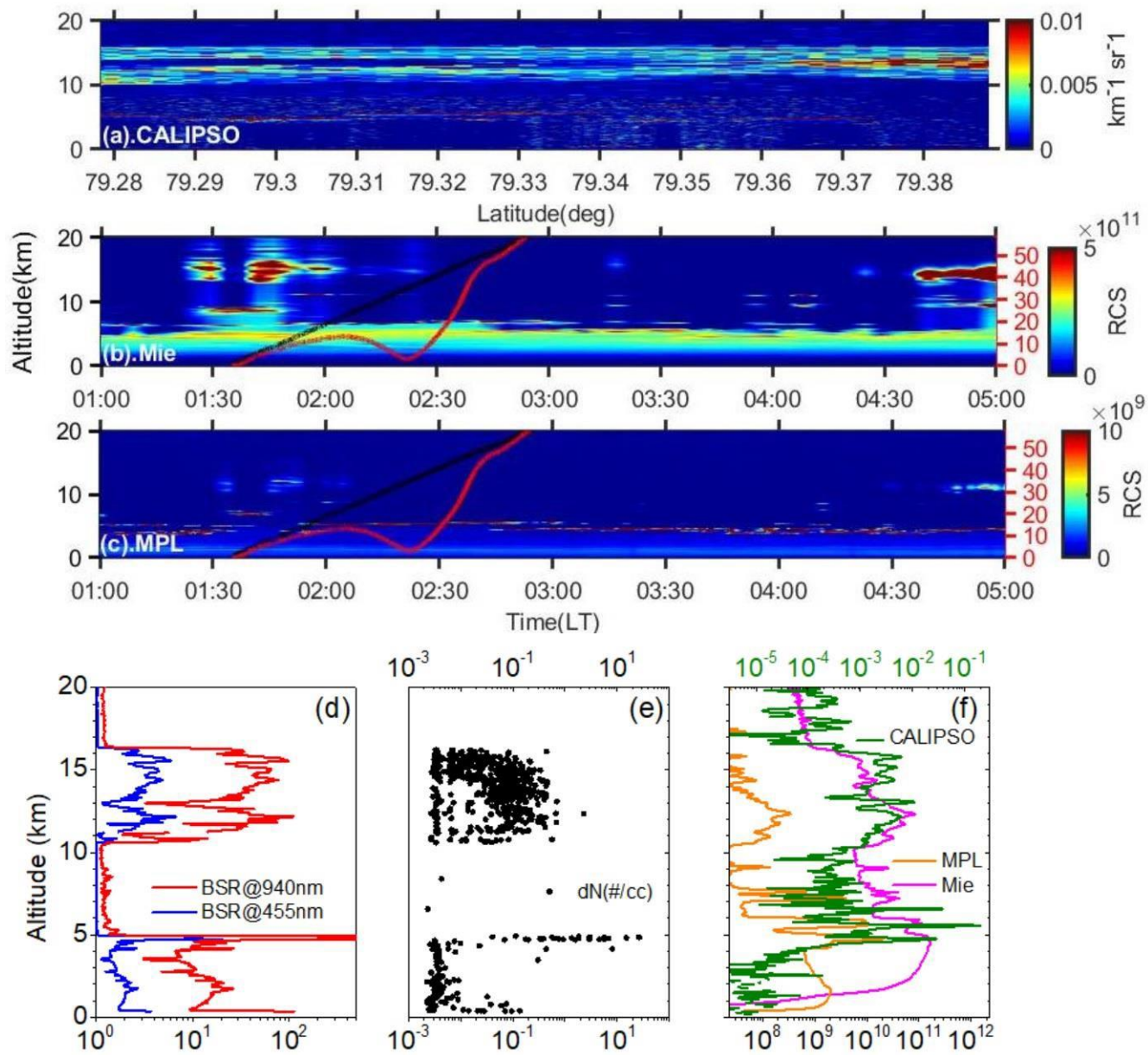


Figure 6. Multi-instrument data from a



1098
1099
1100

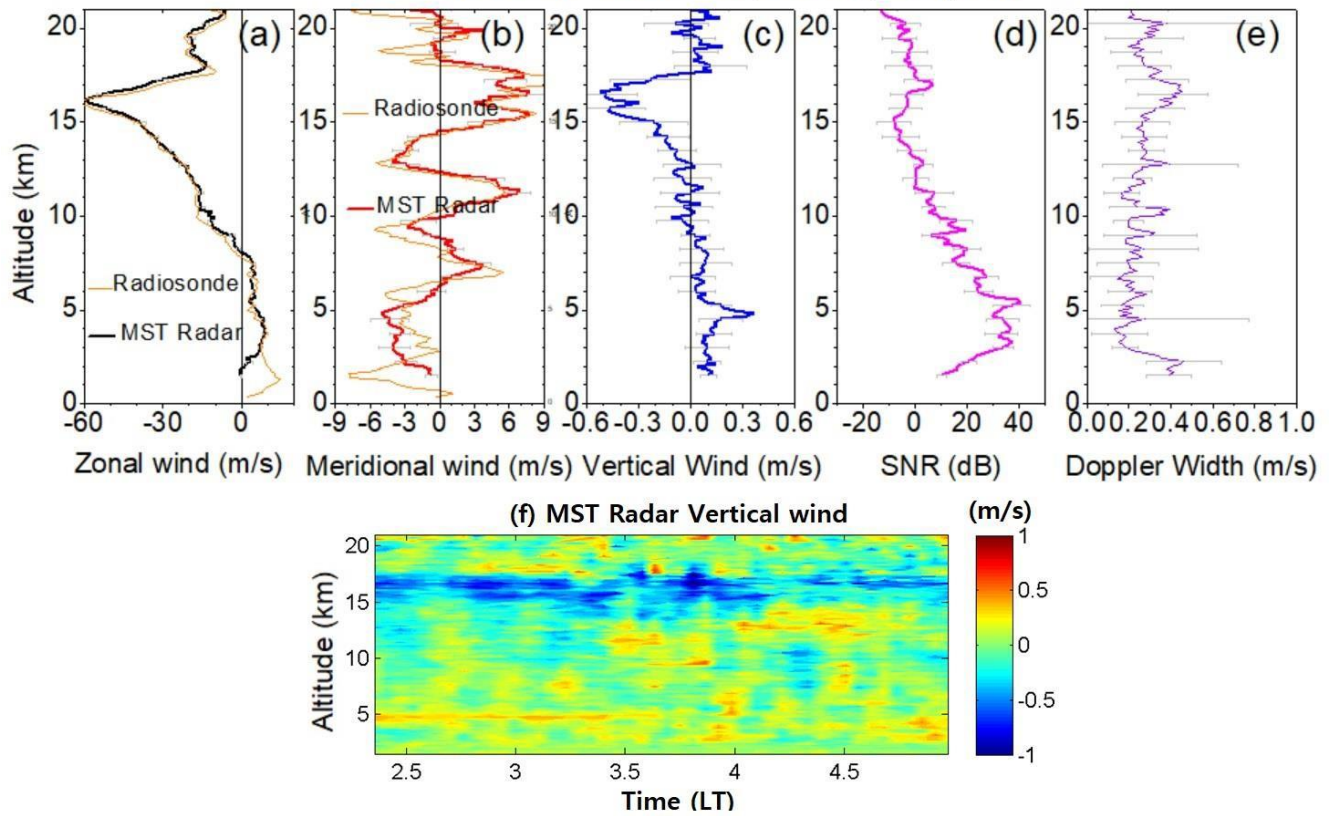
pilot campaign (08 ~~July 2017~~ July 2017).

Altitude(km)

Altitude (km)

Figure
7.
Same
as
Figure
6 but
for the
case of
~~the~~
second

Indian MST Radar & Radiosonde, Gadanki, 8 July 2017



1101
1102
1103
1104
1105
1106
1107
1108

Noise Ratio (SNR) and (e) Doppler Width were obtained from Indian MST radar during 8 July 2017 averaged during 02:30 LT to 03:30 LT. Horizontal bars show standard deviation. Radiosonde observed zonal and meridional winds are also superimposed in the respective panels. (f) Time-altitude section of vertical wind obtained from Indian MST radar during the radiosonde launch time.

Altitude (km)

20.
15.
10.
5.
0.
-5.
-10.

Figure 8. Profiles of (a) zonal wind, (b) meridional wind, (c) vertical wind, (d) Signal to

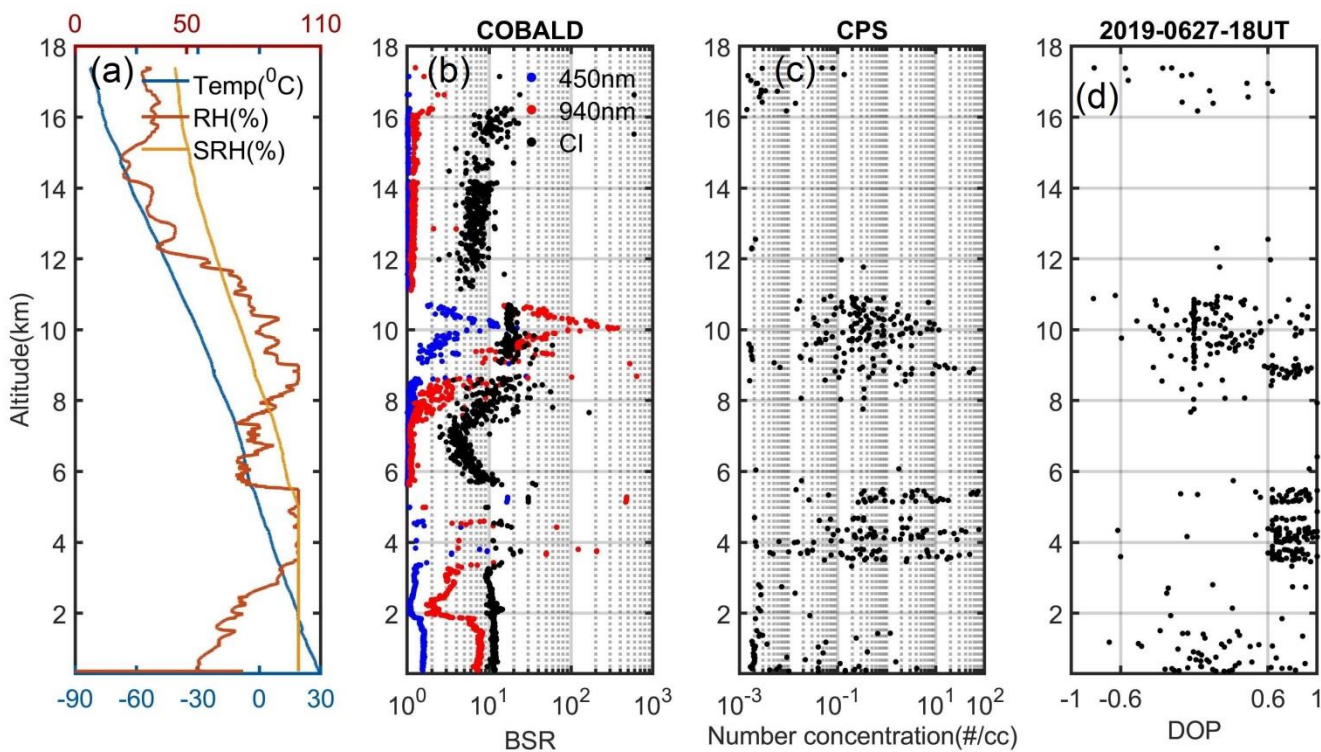
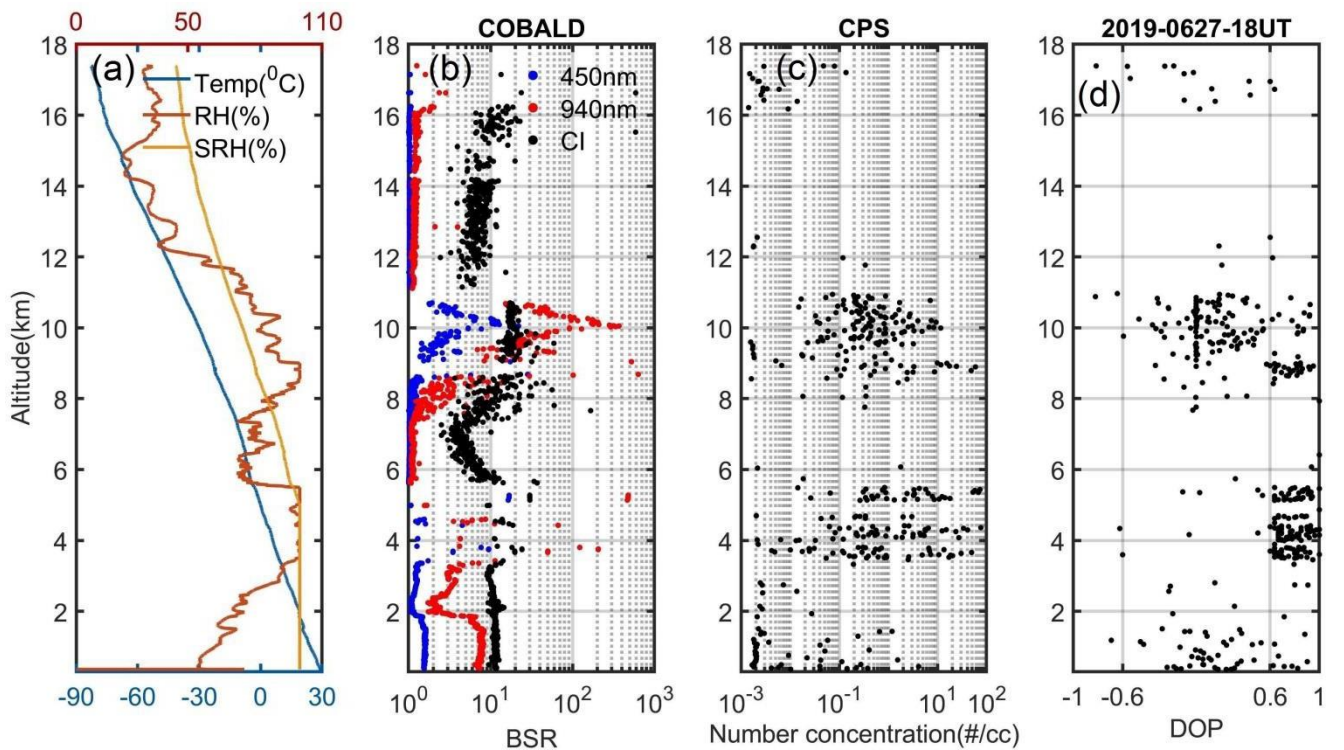
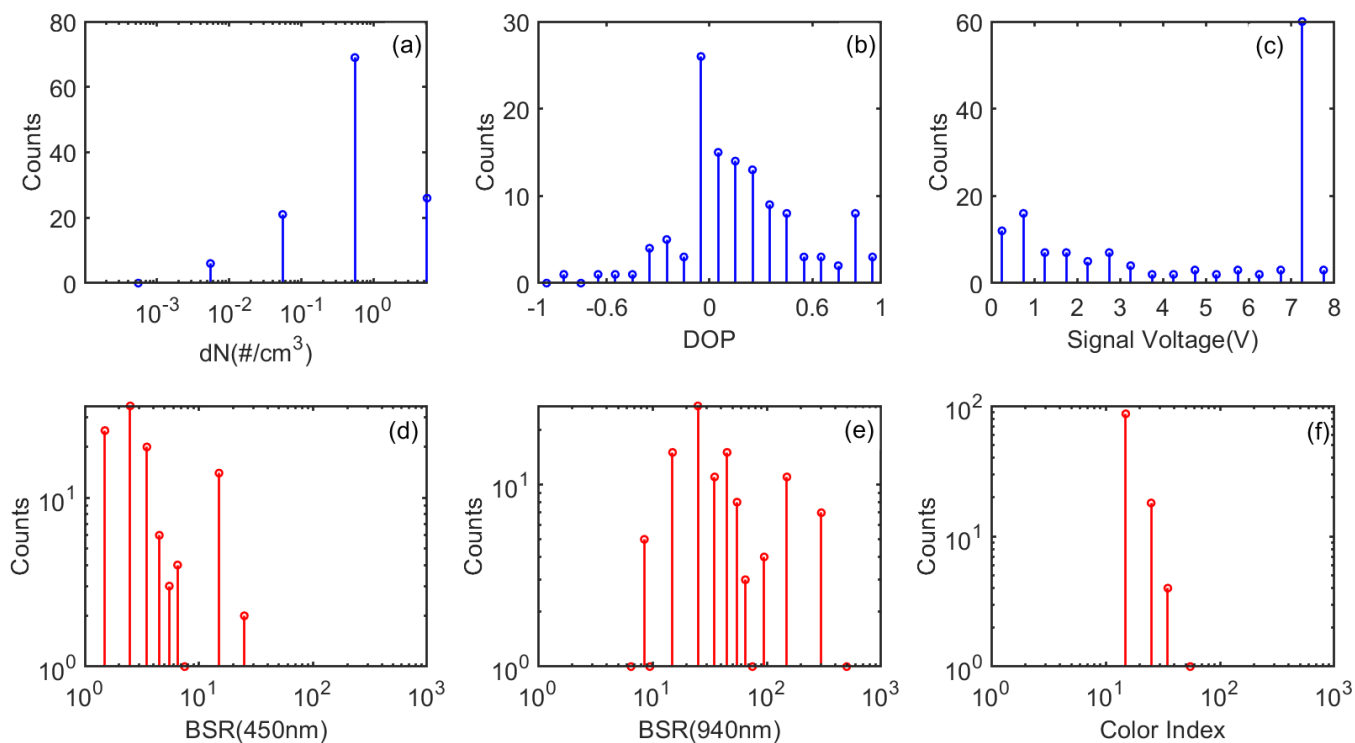


Figure 9. Combined observations of COB ALD and CPS from balloon sounding were held on 27 June 2019 at 2330 LT. (a) Temperature (T), Relative humidity (RH) and Saturation Relative Humidity (SRH) (b) Backscatter ratio at 455 nm (blue), 940 nm (red) and ~~Color~~Colour Index (Black). (c) ~~cloud~~Cloud particle number concentration and (d) Degree of polarization (DOP).

1114
1115

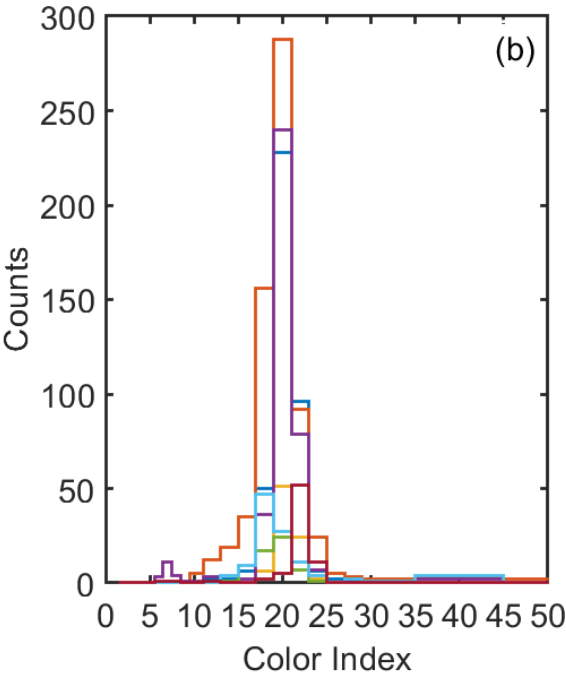
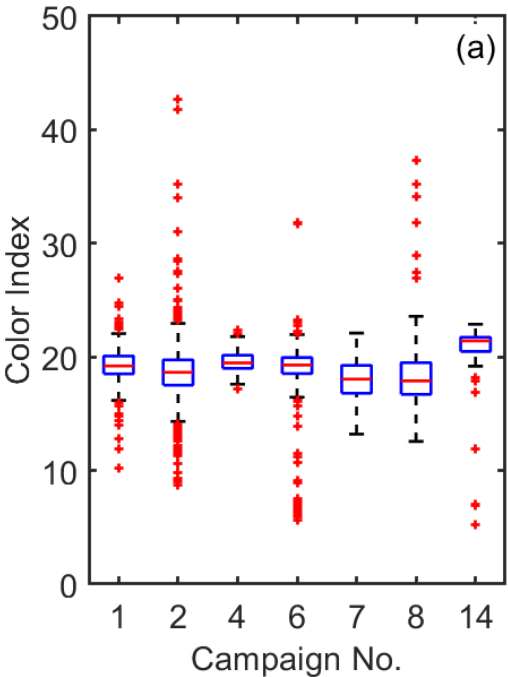


1116
1117
1118
1119
1120
1121

Figure 10. Histogram of (a) Droplet number concentration (dN) in $\text{\#}/\text{cc}$ (b) Degree of polarization (DOP) (c) Backscattered signal (Volts) (d) Backscatter ratio at 455 nm, (e) Backscatter ratio at 940 nm and (f) Color Index. The top panel shows the data from CPS and the bottom panel from COBALD for the ice cloud layer between 9 and 11 km from the sounding held on 27 June 2019.

1122
1123
1124

1125
1126
1127
1128



P) (c) Backscattered signal (Volts) (d) Backscatter ratio at 455 nm, (e) Backscatter ratio at 940 nm and (f) Colour Index. The top panel shows the data from CPS and the bottom panel from COBALD for the ice cloud layer between 9 and 11 km from the sounding held on 27 June 2019.

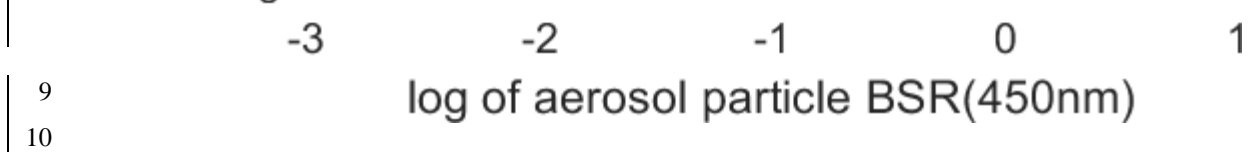
Counts
80
60
40
20
0
Counts
10¹
10⁰
1

Figure 10.
Histogram of
(a) Drop
let
num
ber
conc
entra
tion
(dN)
in
#/cc
(b)
Degr
ee of
polar
izati
on
(DO

Index (CI) was observed for the ice clouds found in different campaigns. The horizontal line in the centre of the box represents the median. The upper and lower edges of the box represent the third quartile (Q3), and first quartile (Q1) respectively. Similarly, the upper and lower whiskers represent $Q3+1.5*(Q3-Q1)$ and $Q1-1.5*(Q3-Q1)$. The data points beyond the whiskers (outliers) are shown with red star symbols. (b) The histogram of the CI values from each campaign. Different colours indicate the data from different campaigns.

Figure 11
The box plot of the CI values from each campaign.

1	1129
2	1130
3	1131
4	1132
5	1133
6	1134
7	1135
8	



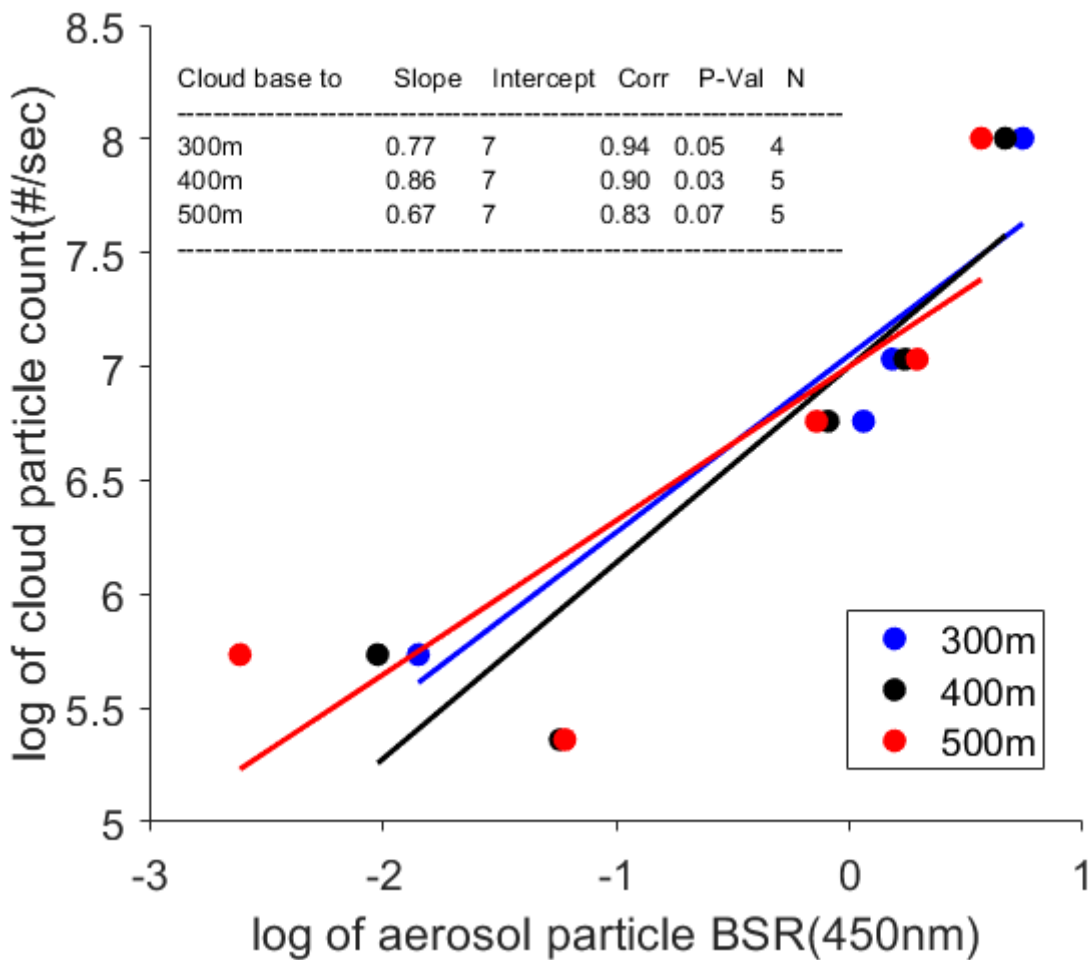


Figure 12. Scatter between logarithm values of COBALD median aerosol blue back-scatter (x-axis) from 100, 200, 300, 400 and 500 meters below the cloud base and the corresponding CPS median cloud particle count (y-axis) obtained from five balloon soundings, with a linear fit (different colored lines). The table inside shows the detailed statistics.
